

1



2

# CVD diamond applications for particle detection and identification in high-radiation environments

3

4

5

6

Matevž Červ  
Vienna University of Technology

7

8

A thesis submitted for the degree of  
*Doctor of technical sciences*

9

10

Geneva 2016



# <sup>11</sup> Contents

<b>12    1</b>	<b>Introduction</b>	<b>1</b>
13    1.1	Fundamental research . . . . .	2
14    1.2	Research institutes . . . . .	3
15    1.3	The Large Hadron Collider . . . . .	4
16    1.4	The ATLAS experiment . . . . .	6
17    1.5	Particle detectors . . . . .	7
<b>18    2</b>	<b>Diamond detectors for radiation detection</b>	<b>9</b>
19    2.1	Semiconductor detectors . . . . .	10
20    2.2	Principles of signal formation in semiconductors . . . . .	11
21    2.3	Carrier transport in a diamond sensor . . . . .	15
22    2.4	Radiation-induced current signals . . . . .	16
23    2.5	Radiation damage . . . . .	21
24    2.6	Temperature effects . . . . .	22
25    2.7	Electronics for signal processing . . . . .	23
<b>26    3</b>	<b>Diamond irradiation study</b>	<b>31</b>
27    3.1	Measurement setup . . . . .	31
28    3.2	Charged particle pulses and spectra . . . . .	37
29    3.3	Radiation limitations . . . . .	39
30    3.4	Temperature limitations . . . . .	48
31    3.5	Conclusion . . . . .	54
<b>32    4</b>	<b>Charge monitoring</b>	
33    4.1	<i>The ATLAS Diamond Beam Monitor</i>	<b>57</b>
34    4.2	Introduction . . . . .	57
35    4.3	Luminosity measurements . . . . .	58
36    4.4	Diamond pixel module . . . . .	59
37    4.5	Module assembly . . . . .	62
38    4.6	Performance results . . . . .	62
39    4.7	Installation and commissioning . . . . .	67
40    4.8	First data taking during collisions . . . . .	70
41    4.9	Conclusion . . . . .	72
<b>42    5</b>	<b>Current monitoring</b>	
43    5.1	<i>Real-time particle identification</i>	<b>73</b>
44    5.2	Motivation . . . . .	73

## *CONTENTS*

---

45	5.2 Requirements . . . . .	74
46	5.3 Device specifications . . . . .	74
47	5.4 Pulse parameters . . . . .	75
48	5.5 Applications . . . . .	76
49	5.6 Description of the firmware . . . . .	77
50	5.7 Control and data interface . . . . .	82
51	5.8 Performance results . . . . .	83
52	5.9 Source calibration . . . . .	86
53	5.10 Applications in neutron instrumentation . . . . .	105
54	5.11 Conclusion . . . . .	117
55	<b>Bibliography</b>	<b>119</b>

<sup>56</sup> **Chapter 1**

<sup>57</sup> **Introduction**

<sup>58</sup> Curiosity is the driving force behind the development of human civilisation. Over centuries, scientists  
<sup>59</sup> have discovered new methods for understanding Nature and the fundamental mechanisms governing  
<sup>60</sup> the Universe, using continually improving research methods and technology to peer ever deeper into  
<sup>61</sup> the heart of matter.

<sup>62</sup> After the initial discovery of atoms, their underlying structure was soon revealed to be that of a positively charged core surrounded by a cloud of orbiting electrons. The atomic nucleus was  
<sup>63</sup> subsequently decomposed into protons and neutrons, which themselves were found to consist of  
<sup>64</sup> three tiny quarks. Studying these minuscule building blocks of visible matter has made it possible  
<sup>65</sup> to understand more about the intricate complexities of the Universe, and the mechanisms that guide  
<sup>66</sup> its behaviour and evolution.

<sup>68</sup> Discoveries of this magnitude would not have been possible without the technologies developed  
<sup>69</sup> to carry out such experiments. On one hand, the energy of the experimental devices has been  
<sup>70</sup> increasing continually, allowing smaller and smaller distance scales to be probed. On the other  
<sup>71</sup> hand, the devices used to observe and measure the phenomena created in these experiments have  
<sup>72</sup> had to be designed with improved precision, speed and durability.

<sup>73</sup> Keeping these factors in mind, the goal of this work was to find “the perfect material”. Diamond  
<sup>74</sup> proved to be a worthy contender, offering both outstanding electrical and mechanical properties  
<sup>75</sup> which make it the material of choice for a number of applications in experimental physics. However,  
<sup>76</sup> much remains to be learned about its behaviour, and this thesis adds a small piece to the shimmering  
<sup>77</sup> mosaic of diamond research efforts.

<sup>78</sup> The first chapter introduces some of the leading particle physics research institutes, and describes  
<sup>79</sup> how their research is carried out. The second chapter discusses the properties of diamond detectors  
<sup>80</sup> used in high energy particle physics experiments. A diamond sensor irradiation study is presented in  
<sup>81</sup> chapter 3. The conclusions of this study, which define the constraints for the two diamond detector  
<sup>82</sup> applications, are presented in the final two chapters.

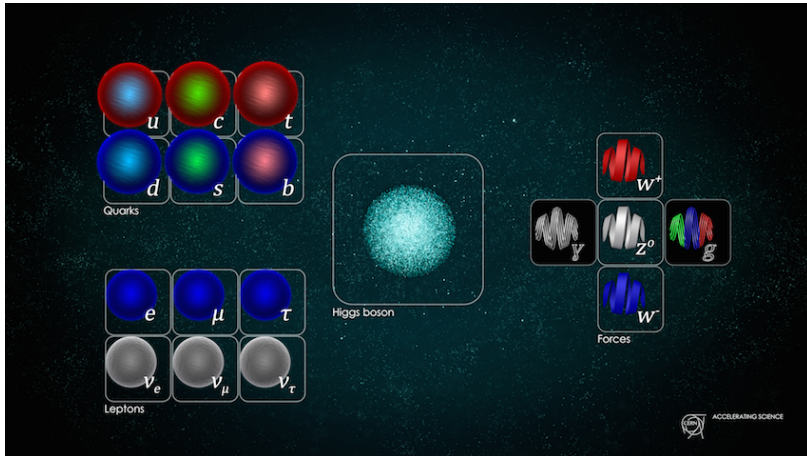


Figure 1.1: The Standard model [2].

## 83 1.1 Fundamental research

84 The aim of fundamental research is to define scientific theories and verify them to improve our  
85 understanding of the universe. It does not in itself focus on applying this research by developing  
86 products and is not meant to create a direct return on investment. Instead, it expands the overall  
87 knowledge of the human kind - by making the results freely available to the general public.

88 Particle physics research peers into the smallest constituents of the universe, dissecting the atoms  
89 into quarks and electrons, catching cosmic rays and figuring out what dark matter is made of. Particle  
90 physicists want to explain the phenomena surrounding us by studying the fundamental particles and  
91 the mechanisms governing their interactions. By understanding this, we would be able to answer  
92 difficult questions; How did the universe begin? What is the invisible force (dark matter, dark  
93 energy) pushing the galaxies apart from each other? Where does mass come from? Why is there  
94 almost no antimatter in the universe? In this effort, scientists have formed several theories. One  
95 of them, the Standard Model of particles, is currently the most successful theory to describe the  
96 constituents of matter and their interactions.

97 **The Standard Model (SM)** is a physics theory developed in the 1970's [1]. It was designed to  
98 explain the current experimental results. As such, it was also able to predict new discoveries and  
99 was a driving force for the scientists to invest time and money in developing new experiments. To  
100 date, it is by far the most established and verified physics theory. It explains how the basic building  
101 blocks of matter – *fermions* – interact with each other via mediators of interactions called *bosons*.  
102 There are two main families of fermions - *quarks* and *leptons*, as shown in figure 1.1. Each group  
103 consists of six members divided into three *generations*, the first being the lightest and most stable  
104 and the last the heaviest, which are the most unstable. The nature around us is made up of the  
105 stable particles – those from the second or third generations can only be found in cosmic rays or  
106 produced artificially using particle accelerators.

107 Quarks have a spin of 1/2 and a charge of either +2/3 (up, charm, top) or -1/3 (down, strange,  
108 bottom) while the leptons have a spin of 1/2 and a charge of either 1 (electron, muon, tau) or 0  
109 (electron neutrino, muon neutrino, tau neutrino). Leptons only exist individually – they do not  
110 cluster. Quarks, however, immediately form a cluster of either two (unstable), three (more stable)  
111 or five (unstable). Two up and one down quark make up a proton whereas two down and one up  
112 quark make up a neutron.

113 In addition to fermions, each particle has its corresponding antiparticle – a particle with the same  
114 mass but the opposite charge. If an antiparticle hits a particle, they annihilate each other, producing  
115 energy in form of photons.  
116 Bosons are the carriers of force that mediate weak ( $W^+$ ,  $W^-$  and  $Z$  bosons), strong (gluons) and  
117 electromagnetic (photons) interactions. The weak interaction is responsible for the radioactive decay  
118 of subatomic particles, thus playing an essential role in nuclear fusion – a process taking place in the  
119 stars. The electromagnetic interaction works at a macroscopic level – it allows particles to interact  
120 via electric and magnetic fields. The strong interaction is effective at femtometer distances and it  
121 governs how quarks interact and bind with each other. An additional boson is the Higgs boson  
122 discovered at CERN in 2012 [3]. It is a representation of the Higgs mechanism, which gives rise to  
123 the mass (or lack thereof) of all the particles in the Standard Model.

## 124 1.2 Research institutes

125 This section gives a short overview of some of the institutes and collaborations carrying out funda-  
126 mental physics research. These facilities were used for the research carried out for this thesis.

127 **CERN** (European Centre for Nuclear Research) [4] is the largest particle physics laboratory in the  
128 world, straddling the Swiss-French border just outside Geneva. It was established in 1954 to bring the  
129 war-torn Europe together by means of fundamental scientific research. Today, its 22 member state  
130 countries and several observer states contribute approximately 1 billion CHF annually to fund the  
131 research and development. More than 10000 scientists, engineers, technicians, students and others  
132 from all around the globe work at CERN on many projects in research fields ranging from particle to  
133 nuclear physics. The scope is to probe the fundamental structure of the universe and to understand  
134 the mechanisms governing it. Therefore CERN’s main function is to provide the infrastructure  
135 for high-energy physics experiments. These are carried out using large machines called particle  
136 accelerators. These instruments boost beams of particles to high energies before making them  
137 collide with each other or with stationary targets. The resulting collisions are recorded by particle  
138 detectors and later analysed by physicists. To carry out research on the smallest constituents of  
139 matter, their dynamics and structure, very high energies are needed. This is why the most powerful  
140 accelerators are used for fundamental research. The largest accelerators at CERN are the Proton  
141 Synchrotron [5], the Super Proton Synchrotron [6] and the Large Hadron Collider, described in 1.3.

142 **Atominstytut, Vienna** (ATI) [7], an institute for atomic and subatomic physics, was established  
143 in 1958 in Vienna as an inter-university institute. It houses around 200 people involved in a broad  
144 range of research fields: quantum, particle, neutron, nuclear, radiation and reactor physics, quantum  
145 optics etc. As of 2002 the ATI is part of the University of Technology in Vienna.

146 Its central facility is *TRIGA MARK II* [8], a neutron reactor used for training, research and isotope  
147 production. It is one of 40 such reactors worldwide, produced by the Californian company General  
148 Atomic in the early 60’s. It is capable of continuous operation at a maximum output power of  
149 250 kW. The reactor core consists of 3 kg of 20 % enriched uranium ( $^{235}\text{U}$ ). The fuel moderator rods  
150 are mostly made up of zirconium with a low percentage of hydrogen and uranium. Both the core  
151 and the rods are immersed in a pool of water as shown in figure 1.2 for the purpose of cooling and  
152 radiation protection. The surrounding concrete walls are 2 m wide with an added graphite layer for  
153 improved shielding. Four main experimental apertures for neutron beam are placed radially through  
154 the walls. All exits are heavily shielded to prevent people from being exposed to radiation, but still

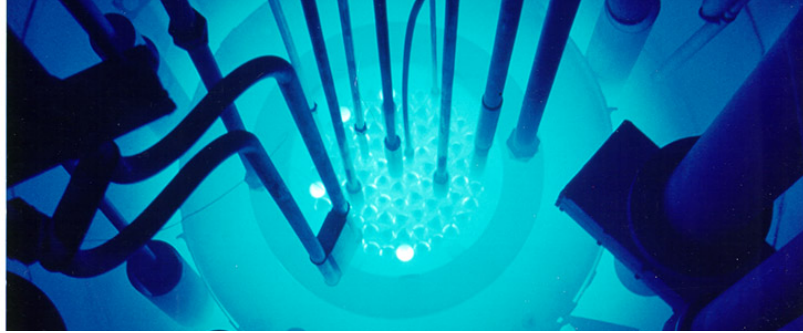


Figure 1.2: The TRIGA MARK II neutron reactor [9].

leaving enough space to set up experiments. Apart from the beam apertures, there are several other exits and components, e.g. a thermal column for generation of thermal (low energetic) neutrons.

**n-ToF** (neutron Time-of-Flight) [10] is a scientific collaboration with the aim of studying neutron-nucleus interactions. Over 30 institutes are active members of this collaboration, among them Atominstitut in Vienna. The n-ToF experiment is located at CERN where the experiments are carried out in a 200 m long experimental area. The knowledge stemming from the experimental results can then be applied in various fields ranging from nuclear technology and cancer therapy to astrophysics.

A pulsed beam of highly energetic protons (20 GeV/c) is produced by the Proton Synchrotron and aimed at a fixed lead spallation target. Each proton hitting the target produces around 300 neutrons of various energies. Initially highly energetic neutrons are slowed down by the target and by a slab of water placed behind it. This broadens their energy spectrum, which then ranges from meV (thermal neutrons) to GeV (fast neutrons). The neutrons are then sent through a 185 m long evacuated pipe to the experimental area, where they collide with another target or a sample. The radiation created by the collisions is detected by a set of dedicated detectors around the interaction point shown in figure 1.3. Having different energies, neutrons travel with different speeds, highly energetic ones reaching the target faster than those with low energies. The analysis of collisions with a precise timing allows for a determination of the interaction probability with the sample material as a function of energy of the incident neutrons.

### 1.3 The Large Hadron Collider

A particle accelerator is a machine that accelerates beams of charged particles such as protons, electrons, ions etc. It generates electric fields that add kinetic energy to the particles, speeding them up. It then uses magnets to retain them within a defined trajectory and inside the evacuated beam pipe. The trajectory can be either linear (linear accelerators or LINACs) or circular (circular or cyclic accelerators). The former accelerate particles in a straight line, therefore the acceleration process only occurs once. The latter can accelerate particles many times while keeping them in orbit, but need a LINAC to pre-accelerate the particles before being injected in the loop.

Particle accelerators are used in numerous fields ranging from fundamental and material research, cancer treatment to industrial applications, such as biomedicine and material processing. Several types of accelerators exist: electrostatic accelerators, LINACs, cyclotrons, synrocyclotrons, synchrotrons, synchrotron radiation sources and fixed-field alternating gradient accelerators (FFAGs).

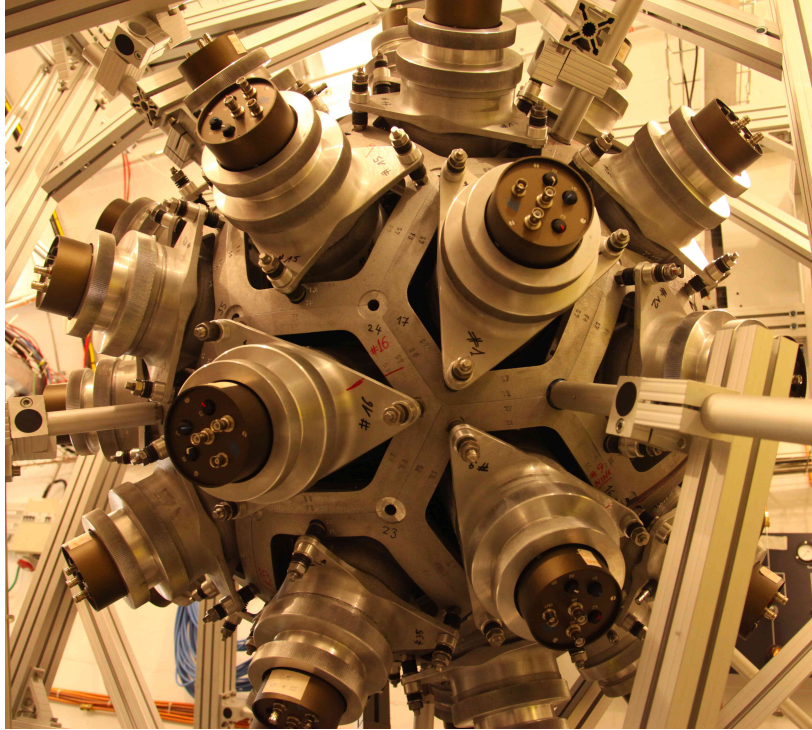


Figure 1.3: The calorimeter in the n-ToF area [11].

186     The Large Hadron Collider (the LHC, figure 1.4) [12] at CERN is the largest particle collider  
187    in the world. It was build between 1998 and 2008 and was first successfully started in 2010 and  
188    operated until 2013 when it underwent a two-year long upgrade. Its second operational cycle started  
189    at the beginning of 2015.

190     The LHC is a 27 km long circular machine set up in a tunnel deep under the surface, ranging  
191    from 50 to 175 m below ground. It accelerates two proton beams to the energy of 6.5 TeV per beam  
192    before it makes them collide with each other with the energy of 13 TeV at four different interaction  
193    points around its circumference. Hair-thin particle beams are guided inside two evacuated pipes with  
194    a  $\sim$ 5 cm radius by means of magnetic field. Coils made up of a superconductive material are wound  
195    around the pipes in special patterns. When cooled down to -271 °C using liquid helium, they become  
196    superconductive; the resistivity of the material drops significantly, minimising the heat dissipation  
197    despite high electric currents. These produce strong magnetic fields which bend the particles and  
198    keep them in a circular trajectory.

199     The protons travel bunched together in groups – bunches. There are  $10^{11}$  protons in every  
200    bunch. These are accelerated when traversing the radio-frequency (RF) cavities with the frequency  
201    of the electromagnetic field equal to 400 MHz. This oscillating field creates 2.5 ns long buckets –  
202    compartments for the bunches. Only one out of ten buckets is filled, so the bunches are spaced at  
203    25 ns. This defines the machine’s clock (40 MHz) as well as the maximum rate of bunch crossings  
204    – the bunches travelling in the opposite direction cross at the intersections 40 million times per  
205    second. Around 20 collisions occur during every bunch crossing, yielding the maximum collision  
206    rate of the order of  $10^9$  s $^{-1}$ . The number of collisions will increase in the following years; the  
207    number of particles per bunch will be increased and the transverse spread of the bunches will be  
208    decreased. The bunch density will therefore be increased, which will in turn increase the collision  
209    probability – the cross-section. The original design number of collisions accumulated over the years

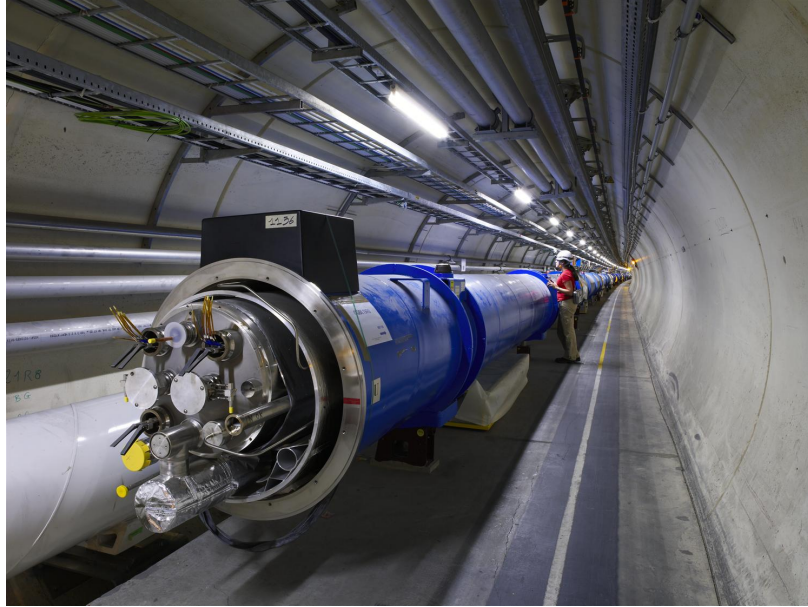


Figure 1.4: The Large Hadron Collider [13].

of operation is presented in the form of integrated luminosity [14] and is of the order of  $300 \text{ fb}^{-1}$  (inverse femtobarn). After the planned upgrades in 2020, the High-Luminosity LHC [15] will achieve up to  $3000 \text{ fb}^{-1}$ .

## 1.4 The ATLAS experiment

ATLAS (short for A Toroidal Lhc ApparatuS, figure 1.5) [16] is a particle physics experiment at CERN. Its purpose is to verify current theories and to search for new discoveries by observing and analysing high energy proton-proton collisions produced by the LHC. It is the biggest experiment at CERN by dimensions (45 m in length and 26 m in height) and the number of people involved (more than 3000 physicists and engineers). The ATLAS experiment consists of a number of detectors, each designed to measure a specific property of the particles and photons produced during the collision. The closest to the collision point is the Inner Detector (ID), which consists of scintillating elements, a Transition Radiation Tracker and of the several layers of highly spatially segmented semiconductor sensors, which record single points of the incident particles. These points are later reconstructed into particle tracks. In addition, a strong magnetic field of 2 T curves the paths of the charged particles, which in turn allows the ID to identify an individual particle's charge and momentum. The next two parts are the electromagnetic and tile calorimeter. These detectors weigh a few thousand tonnes and measure the energy that the particles deposit in the material. The only particles that make it through the calorimeters are neutrinos and muons. The former cannot be detected with the detectors in ATLAS. The latter however are detected by the Muon Spectrometer, a set of large detector plates placed all around the calorimeters. The last is the superconductive magnet which provides the magnetic field to allow the Muon Spectrometer to measure muon momenta. The ID has its own set of magnets that are used for the same purpose. To sum up, the Inner Detector measures the charge and momenta of the particles, the calorimeters measure their energies, the Muon Spectrometer measures muon tracks and momenta and the magnets provide magnetic fields, which curve the trajectories of the charged particles, allowing for identification of particle momenta.

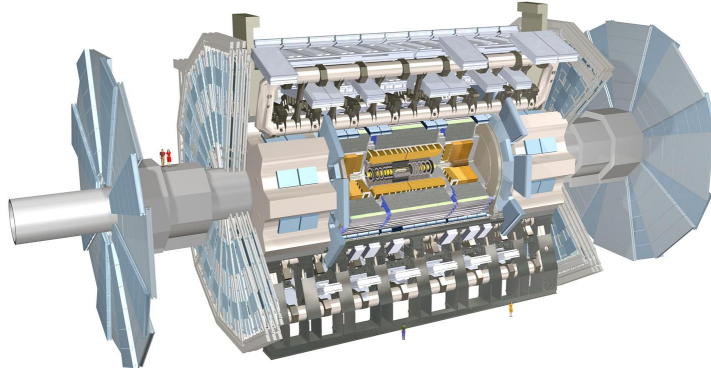


Figure 1.5: The ATLAS Experiment [17].

235     The ATLAS detector has been designed to measure every collision taking place in its core. With  
236     25 ns between collisions, this makes up 40 million bunch crossings per second. The maximum realistic  
237     achievable rate of recording is approximately 100 kHz [16]. A recorded collision is referred to as an  
238     event. Every event holds information acquired by all the detectors within ATLAS. This amounts to  
239     approximately  $\sim 10^7$  channels of data, yielding an event size of approximately 10 MB. Therefore the  
240     data rate at the maximum achievable rate is 3 TB/s. To reduce the amount of data stored a special  
241     classification system with a complex trigger logic, which is in place to decide which events should  
242     be stored and analysed further. It reaches a decision in the order of tens of microseconds after an  
243     event. If this is the case, the data acquisition system triggers the readout of the entire detector.  
244     This way the recorded event rate is reduced from 100 kHz to  $\sim 500$  Hz.

245     A complex Trigger and Data Acquisition system (TDAQ) is in place to distribute the clock signal,  
246     configure the detectors, perform data acquisition and handle the output data. The data are then  
247     stored at the CERN computer centre and distributed across the globe by means of the GRID – a  
248     distributed data analysis and data storage system.

## 249     1.5 Particle detectors

250     Particle detectors, or radiation detectors, have first come into use at the end of the 19th century.  
251     In 1895 Wilhelm Röntgen used a photographic plate onto which he shone X-rays. Soon after, in  
252     1912, Victor F. Hess discovered cosmic rays during a balloon flight. This paved the way for develop-  
253     ment of particle detectors. A cloud chamber was designed – a chamber filled with a supersaturated  
254     vapour of water or alcohol. If a highly energetic particle traversed the chamber, the mixture ionised,  
255     creating condensation nuclei. These traces were visible and were photographed. The particle de-  
256     tectors developed later relied on different types of interaction between the incident particles and  
257     the detector material, e.g. transition radiation, Cherenkov radiation and ionisation. The bubble  
258     chamber invented in 1952 used a superheated transparent liquid – a liquid heated just below its  
259     boiling point. A particle ionised the liquid, forming microscopic bubbles along its trajectory. Then  
260     followed the spark chamber and the wire chamber where the particle ionised the gas, causing a spark  
261     between two parallel plates at a high potential difference. These are nowadays used in a handful of

## 1.5. PARTICLE DETECTORS

---

262 experiments and may often be seen in museums as showcases. Next were ionisation chambers, which  
263 measured the induced current of the free ionised charges moving in an externally applied electric  
264 field. Finally in the 1960s, semiconductor detectors were introduced. Their principle of operation is  
265 similar to that of an ionisation chamber, with the difference that a semi-conductive material is used  
266 as an ionisation medium instead of gas. Nowadays an ensemble of several types of detectors is used  
267 as a specialised detector system. Many considerations need to be taken into account when designing  
268 such a system: detector geometry, segmentation, event rate, efficiency, readout, support structures,  
269 cabling, cooling, cost etc.

270 Particle detectors can be divided in two groups: tracking detectors and calorimeters. The former  
271 are designed to measure particle momentum, charge, origin and direction of flight, with a minimal  
272 impact on their flight path or energy with the aim to optimise the spatial resolution. The calorime-  
273 ters, on the other hand, measure the energy of the particles by stopping them. This means they  
274 need to be heavy and dense. A typical physics experiment nowadays consists of a tracking detector  
275 enclosed by a calorimeter. This way the energy, charge and momentum can be derived for every  
276 particle created in the collision.

<sup>277</sup> **Chapter 2**

<sup>278</sup> **Diamond detectors for radiation  
<sup>279</sup> detection**

<sup>280</sup> Diamond has been known for over two millennia, valued for its mechanical properties and its ap-  
<sup>281</sup>pearance. When the procedures for its synthesis were discovered, diamond made its way to a broad  
<sup>282</sup>range of industries which exploit its optical and electrical properties. The discovery of the Chemical  
<sup>283</sup>Vapour Deposition (CVD, described below) as a new synthesis process gave rise to a range of new  
<sup>284</sup>applications. Purer specimens are used in electronics, high-power switching devices, electrochemical  
<sup>285</sup>systems, radiation sensors, quantum computing etc. Recently it was found that it also exhibits su-  
<sup>286</sup>perconductivity [18]. This thesis focuses on the use of diamond for radiation detection. An example  
<sup>287</sup>of such a diamond sample is shown in figure 2.1.

<sup>288</sup> Compared to a natural diamond, a CVD diamond used as a particle detector has almost no impu-  
<sup>289</sup>rities (foreign atoms like nitrogen or boron). If proper procedures are followed, the diamond lattice  
<sup>290</sup>can be grown very uniformly. This in turn improves electrical properties of the grown sample. Such  
<sup>291</sup>a diamond is an almost perfect thermal and electrical insulator. However, its electrical behaviour  
<sup>292</sup>is similar to that of a semiconductor. For this reason this chapter first introduces semiconductor  
<sup>293</sup>detectors and then describes the principle of signal formation in semiconductors. Then it focuses on  
<sup>294</sup>the diamond sensor and its properties.

<sup>295</sup> **Chemical vapour deposition** (CVD) [19] is a process where a material is deposited from a gas  
<sup>296</sup>onto a substrate, involving chemical reactions. It is often carried out under high pressure and  
<sup>297</sup>high temperatures. It takes place in enclosed chambers called furnaces with careful regulation of the  
<sup>298</sup>temperature, pressure and gas mixture. Synthetic diamond is grown at 700–900 °C with a mixture of  
<sup>299</sup>hydrogen and methane gas. At this temperature the molecules dissociate into carbon and hydrogen  
<sup>300</sup>atoms. The carbon atoms are the building blocks and are deposited on the surface of the substrate.  
<sup>301</sup> Under carefully controlled pressure and temperature conditions with an added abrasive atomic hy-  
<sup>302</sup>ydrogen the graphitic bonds break and form into diamond bonds. The speed of the growth can be  
<sup>303</sup>anywhere between 0.1 and 10 µm per hour. The detector grade samples are grown at a rate of the  
<sup>304</sup>order of 1 µm per hour. They can grow up to several millimetres in thickness. The width of the  
<sup>305</sup>samples, however, depends entirely on the substrate used. Diamond can be deposited on various  
<sup>306</sup>materials: diamond, silicon, tungsten, quartz glass etc. The substrate material must be able to  
<sup>307</sup>withstand the high temperatures during the CVD process. The diamond substrate does not need  
<sup>308</sup>any surface pre-treatment. Carbon atoms form bonds with atoms in the existing crystal structure.  
<sup>309</sup> This is the homo-epitaxial growth where the newly deposited atoms retain the orientation of the  
<sup>310</sup>structure in the substrate. Other non-diamond substrates, however, need to be pre-treated, usually

## 2.1. SEMICONDUCTOR DETECTORS

---

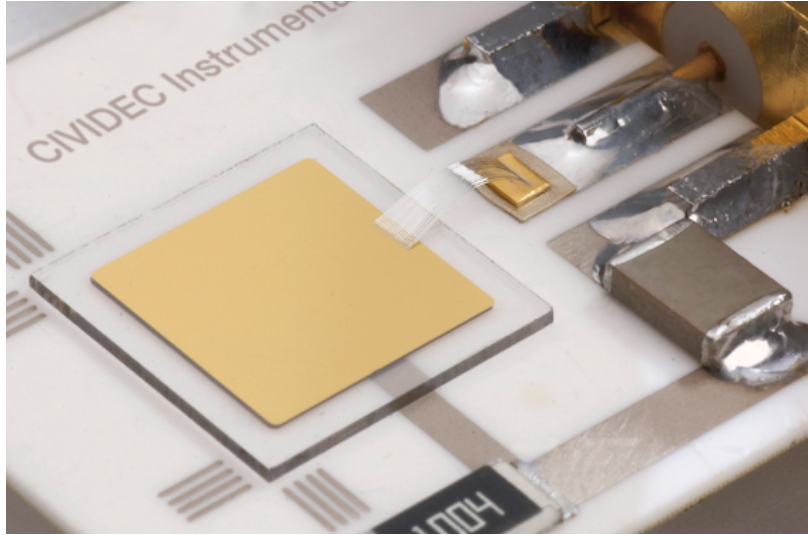


Figure 2.1: A pCVD diamond pad detector [20].

311 by being polished using diamond powder. Some powder particles remain on the surface, acting as  
312 seeds for the growth of small crystals or grains. These grains grow and at some point merge with the  
313 adjacent ones, making up a compact material. The lower side is later polished away. These diamonds  
314 are *polycrystalline* (pCVD) whereas those grown on a diamond substrate are *single crystal* (sCVD)  
315 diamonds. The area of the former can be large - up to  $0.5 \text{ m}^2$  or more compact  $75 \text{ cm}^2$  in the case  
316 of detector grade diamonds, which can be further cut into smaller parts. The sCVD diamonds, on  
317 the other hand, can currently only achieve sizes up to  $1.5 \text{ cm}^2$ .

## 318 2.1 Semiconductor detectors

319 Semiconductor is a class of solids whose electrical conductivity is between that of a conductor and  
320 that of an insulator – of the order of  $10^{-5} \Omega^{-1} \text{ cm}^{-1}$  [21]. Semiconductors consist of atoms with  
321 four electrons in their valence band, e.g. silicon–Si or germanium–Ge, or as combinations of two or  
322 more different materials, e.g. gallium arsenide–GaAs). The atoms in the lattice form valence bonds  
323 with adjacent atoms, creating solid crystal structures.

324 Semiconductor particle detectors are devices that use a semiconductor material to detect radia-  
325 tion. They work on the principle of an ionisation chamber. An incident particle ionises the atoms  
326 in the crystal lattice. The charges are freed if the deposited energy is higher than the energy band  
327 gap, i.e. the energy needed to excite an electron from its steady state to the conductance band.  
328 The freed charge carriers start drifting in an externally applied electric field, inducing current on  
329 the electrodes. The induced signal is amplified and read out by the electronics in the detector signal  
330 chain.

331 Semiconductor detectors are most widely used for tracking applications, like the Insertable B-  
332 Layer shown in figure 2.2 [22], which was installed in ATLAS Experiment in 2014. First, they can be  
333 produced in thin layers to minimise the impact on the path of the incident particles. Second, their  
334 low sensor capacitance allows for a fast signal response. Third, they are highly efficient and highly  
335 resistant to radiation damage. Finally, the industrial processes allow for a fine spatial segmentation,  
336 which in turn improves the track resolution of the detector systems.

337 Semiconductor sensors come in several configurations. The simplest type is a pad – a single

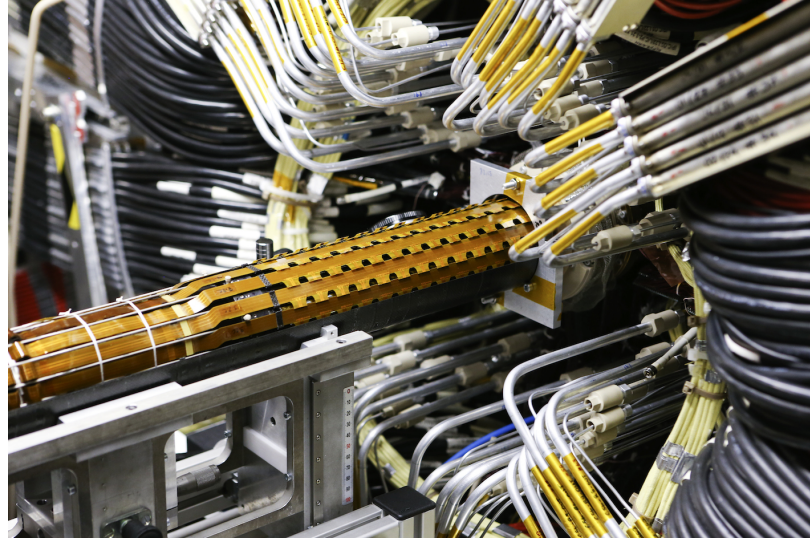


Figure 2.2: The Insertable B-Layer – a silicon particle tracker installed in the ATLAS experiment in 2014 [23].

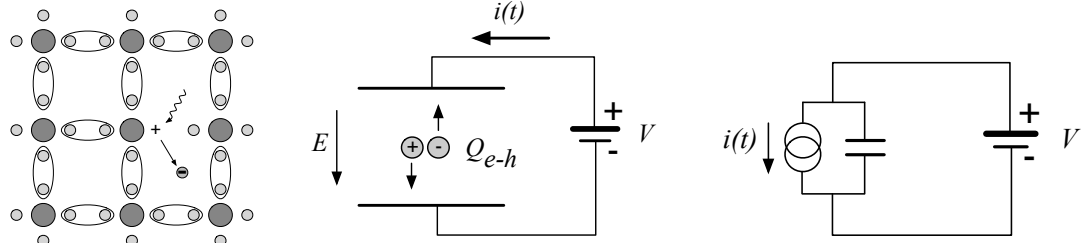
338 plate with two electrodes. Pads are used for particle counting and radiation monitoring. Next is a  
339 strip detector, a more finely segmented detector made out of long parallel sensing areas or strips.  
340 Normally each strip has its own signal line for readout. Usually the strip detectors are used in pairs  
341 – one detector is placed on top of the other at an angle to increase spatial resolution in both axes.  
342 The third and the most finely segmented is a pixel detector, consisting of a 2D array of independent  
343 sensing areas. In tracking applications, pixel detectors are used where the need for a high detection  
344 resolution and granularity requirement is the highest. Due to their high production cost and a high  
345 number of signal channels, they can only cover limited areas. Strip detectors can be used to cover  
346 larger areas in several consecutive layers.

## 2.2 Principles of signal formation in semiconductors

347 Particles can interact with the sensor in several ways, e.g. via bremsstrahlung [24], elastic or inelastic  
348 scattering or nuclear reactions [25]. Bremsstrahlung is radiation created when a particle is deceler-  
349 ated due to interaction with the electric field of the core of an atom. Elastic scattering is deflection  
350 of the particle's trajectory due to the pull from the nucleus without depositing any energy in it.  
351 This is in principle an unwanted effect in semiconductors as it deteriorates the spatial resolution of  
352 the sensor. Inelastic scattering is the interaction through which an electron in the atom is *ionised*.  
353 Nuclear reaction is the direct interaction between the incident particle and the core of the atom. All  
354 these effects are competing and are dependent on the particle's mass, momentum etc. The scope of  
355 this chapter is to discuss the ionisation mechanism in semiconductors.

357 The energy of the electrons forming valence bonds between atoms in the crystal lattice is within  
358 the *valence band* [21]. To break a bond and excite the electron into a *conduction band*, a sufficient  
359 energy has to be applied. The minimal energy required is equal to the energy band gap  $E_g$  of the  
360 semiconductor. Typical  $E_g$  values are 0.7 eV in Ge, 1.12 eV in Si and 1.4 eV in GaAs. Diamond  
361 with its 5.5 eV band gap is considered an insulator. The separation between the conductive and  
362 valence band is referred to as *forbidden gap* where no electron states can exist.

363 An electron excited into the conduction band leaves behind a positively charged ion with a



(a) Valence bonds in the crystalline structure can be broken, creating a free electron-hole pair

(b) The freed electron-hole pair starts drifting in the externally applied electric field. The electron and the hole both drift in the opposite directions towards the oppositely charged electrodes.

(c) Equivalent electrical circuit. The moving charges act as a current source.

Figure 2.3: In the equivalent electrical circuit diagram the electron-hole creation and drift can be modelled as a current source with a capacitor in parallel.

vacancy – a hole – in its valence band, as shown in figure 2.3a. A free *electron-hole pair* is thus created. The free electron travels through the crystal until it is recombined with another hole. Similarly the positive charge of the hole attracts a bound electron in the vicinity, causing it to break from the current bond and moving to the vacancy, thus leaving behind a newly created hole. The process continues, making it look like the hole is traveling through the material [21].

Both the electron and the hole are referred to as *charge carriers*. Without an externally applied electrical field, they propagate in random directions. Therefore on average there is no overall motion of charge carriers in any particular direction over time.

However, if an external electric field is applied to the crystalline structure, the free electrons and holes drift toward the positive and negative potential, respectively, as shown in figure 2.3b. While drifting, the charges couple with the electrodes, inducing current in the circuit, which is explained by the Shockley–Ramo theorem below. Upon reaching the electrodes the charges stop inducing the current. The equivalent electrical circuit is shown in figure 2.3c.

### 2.2.1 Signal induction by moving charges

The signal induction in a conducting plane by a point-like charge, which couples with an electrode, is derived in [26]. The electrode can in this case be modelled as an infinite conducting plane. When a point charge  $q$  is created (e.g. an electron-hole pair created via ionisation), its electrostatic field lines immediately couple with the electrode, as seen in figure 2.4a. The electric field on the metal surface due to a point-like charge  $q$  at the distance  $z_0$  is

$$E_z(x, y) = \frac{q z_0}{2\pi\epsilon_0(x^2 + y^2 + z_0^2)^{\frac{3}{2}}} \quad E_y = E_z = 0. \quad (2.1)$$

A mirror charge appears on the conducting plane, with a charge density distribution

$$\sigma(x, y) = \epsilon_0 E_z(x, y) = \frac{q z_0}{2\pi(x^2 + y^2 + z_0^2)^{\frac{3}{2}}}. \quad (2.2)$$

The charge density integrated over the entire plane yields a mirror charge  $Q$ , which is an opposite of point charge  $q$ :

$$Q = \int_{-\infty}^{\infty} \int_{-\infty}^{\infty} \sigma(x, y) dx dy = -q. \quad (2.3)$$

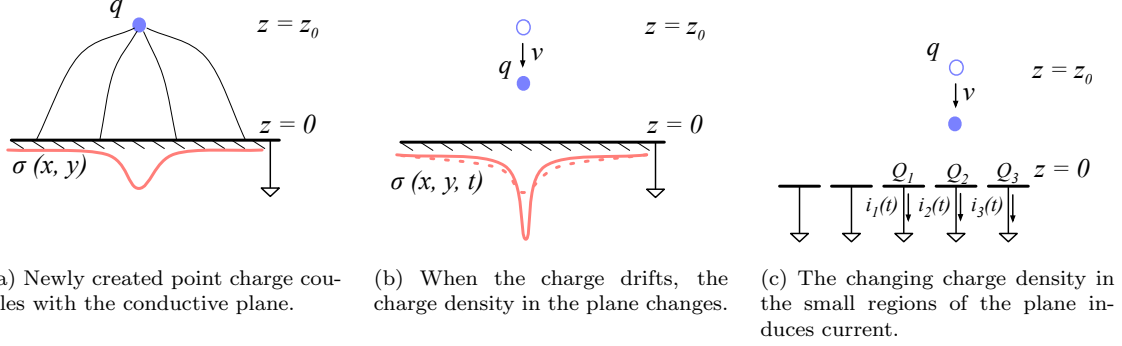


Figure 2.4: A point-like charge inducing current in a conductive plane.

386 The plane is then segmented into infinitely long strips with a width  $w$  whereby each of the strips  
 387 is grounded, as shown in figure 2.4c. Considering a charge density distribution 2.2, the resulting  
 388 mirror charge on a single strip  $Q_2$  directly below the point charge ( $x = 0, y = 0$ ) yields

$$Q_2(z_0) = \int_{-\infty}^{\infty} \int_{-w/2}^{w/2} \sigma(x, y) dx dy = -\frac{2q}{\pi} \arctan\left(\frac{w}{2z_0}\right) \quad (2.4)$$

399 If the charge starts moving towards the conducting plane, the mirror charge density distribution also  
 390 changes, as shown in figure 2.4b. As a result the  $Q_2[z(t)]$  changes with time. The changing charge  
 391 is in effect an induced electric current  $i_2(t)$ :

$$i_2(t) = -\frac{d}{dt} Q_2[z(t)] = -\frac{\partial Q_2[z(t)]}{\partial z} \frac{\partial z(t)}{\partial t} = \frac{4qw}{\pi[4z(t)^2 + w^2]} v. \quad (2.5)$$

392 The movement of the point-like charge therefore induces current in the conducting plane. The  
 393 induced current is linearly dependent on the velocity of the point-like charge.

### 394 2.2.2 Shockley-Ramo theorem

395 W. Shockley [27] and S. Ramo [28] independently proposed a theory which explains how a moving  
 396 point charge induces current in a conductor. The Shockley-Ramo theorem can therefore be used  
 397 to calculate the instantaneous electric current induced by the charge carrier or a group of charge  
 398 carriers. It can be used for any number of electrodes. It states that the current  $I_n^{\text{ind}}(t)$  induced on  
 399 the grounded electrode  $n$  by a point charge  $q$  moving along a trajectory  $\mathbf{x}(t)$  reads

$$I_n^{\text{ind}}(t) = -\frac{dQ_n(t)}{dt} = -\frac{q}{V_w} \nabla \Psi_n[\mathbf{x}(t)] v(t) = -\frac{q}{V_w} \mathbf{E}_n[\mathbf{x}(t)] v(t), \quad (2.6)$$

400 where  $\mathbf{E}_n(\mathbf{x})$  is the *weighting field* of electrode  $n$  in the case where the charge  $q$  is removed, electrode  
 401  $n$  is set to voltage  $V_w = 1$  and all other electrodes are grounded. The weighting field is defined as  
 402 the spatial differential of the *weighting potential*:  $\mathbf{E}_n(\mathbf{x}) = \nabla \Psi_n(\mathbf{x})$ . In the case of two parallel  
 403 electrodes, the weighting field is  $E_w = -\frac{d\Psi}{dx} = -1/d$ , where  $d$  is the distance between the electrodes.  
 404 The resulting induced current is therefore

$$i(t) = \frac{q}{d} v_{\text{drift}}(x, t), \quad (2.7)$$

405 whereby  $v_{\text{drift}}$  is the drift velocity of the point-like charge and  $d$  is the distance between the electrodes.  
 406  $d$  is defined by the dimensions of the sensor. The drift velocity is a function of the externally applied

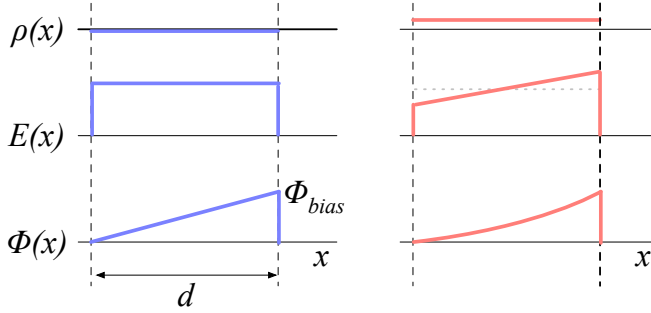


Figure 2.5: Left figure shows a profile of a diamond sensor only with an externally applied electric field. In the figure on the right a uniformly distributed space charge is added in the diamond, contributing to the internal electric field distribution. The induced current signal is proportional to the electrical field.  $d$  is the thickness of the diamond sensor.

407 electric field, as defined in section 2.3. If the electric field is set to a constant value, the induced  
 408 current is directly proportional to the drifting charge. Therefore, by measuring the height of the  
 409 induced current at a specific point of time the number of moving charges can be deduced.

### 410 2.2.3 Thermal excitation

411 Electrons can be thermally excited to the conduction band. The intrinsic concentration of thermally  
 412 excited electrons  $n_i$  in semiconductors is proportional to [21]

$$n_i \propto \exp\left(-\frac{E_g}{2k_B T}\right) \quad (2.8)$$

413 wherein  $k_B = 1.381 \times 10^{-23} \text{ m}^2 \text{ kg s}^{-2} \text{ K}^{-1}$  is the Boltzmann constant,  $E_g$  is the energy band gap  
 414 of the semiconductor and  $T$  is the temperature in K. Due to the small band gap in semiconductors  
 415 a significant amount of electrons already occupies the conduction band at room temperature due to  
 416 thermal excitation, according to the probabilistic distribution. To reduce this effect semiconductor  
 417 sensors are doped with donors and acceptors, forming a diode [21]. The diode is then inversely  
 418 biased to deplete the material of all free charges. Doped silicon fulfills most of the needs for particle  
 419 physics requirements and is therefore the most widely used material for particle detection. Diamond  
 420 with its high energy band gap on the other hand only has a negligible number of thermally excited  
 421 electrons at room temperature. Therefore a p-n junction is not needed, which simplifies the sensor  
 422 production.

### 423 2.2.4 Space charge

424 The Poisson equation shows that

$$\frac{d^2\Phi(x)}{dx^2} = \frac{dE(x)}{dx} = \frac{\rho(x)}{\epsilon} \quad (2.9)$$

425 where  $\rho(x)$  is the space charge distribution,  $E$  is the electrical field and  $\Phi$  is the voltage potential.  
 426 In an ideal diamond, the externally applied high voltage potential on the two electrodes decreases  
 427 linearly through the sensor. The electrical field is therefore constant throughout the sensor and  
 428 the space charge distribution across it equals 0. However, space charge may be introduced in the

material either by means of accumulating of charge carriers in the lattice (i.e. charge trapping) or already during sensor production. The space charge can be either permanent or changing – sometimes it is possible to reduce it, as is shown in chapter 3. All in all, it is very important to reduce it because it affects the shape of the electrical signal. Since the drift velocity of the charge carriers is proportional to the electrical field, the charges change their velocity while drifting through the space charge region. Figure 2.5 compares the voltage potential, the electrical field and the space charge for an ideal sensor as well as for that with a uniformly distributed positive space charge.

## 2.3 Carrier transport in a diamond sensor

This section describes the carrier transport phenomena in diamond. This theory provides the basis for discussion about the measurements in chapter 3. Table 2.1 compares the properties of diamond and silicon. Some of these values are revisited and used in the course of this thesis.

Property	Diamond	Silicon
Band gap energy $E_g$ (eV)	5.5	1.12
Electron mobility $\mu_e$ ( $\text{cm}^2 \text{ V}^{-1} \text{ s}^{-1}$ )	1800 [29]	1500 [21]
Hole mobility $\mu_h$ ( $\text{cm}^2 \text{ V}^{-1} \text{ s}^{-1}$ )	2500 [29]	450 [21]
Breakdown field ( $\text{V cm}^{-1}$ )	$10^7$	$3 \times 10^5$
Resistivity ( $\Omega \text{ cm}$ )	$> 10^{11}$	$2.3 \times 10^5$
Intrinsic carrier density ( $\text{cm}^{-3}$ )	$< 10^3$	$1.5 \times 10^{10}$
Mass density ( $\text{g cm}^{-3}$ )	3.52	2.33
Atomic charge	6	14
Dielectric constant $\epsilon$	5.7	11.9
Displacement energy (eV/atom)	43	13 – 20
Energy to create an e-h pair (eV)	13	3.6
Radiation length (cm)	12.2	9.6
Avg. signal created/ $\mu\text{m}$ (e)	36	89

Table 2.1: Comparison diamond – silicon [21, 29].

When the charge carriers are freed in a semiconductor with no concentration gradient and without an externally applied electric field, they scatter in random directions with a thermal velocity  $v_{th}$  [21]. Their integral movement due to thermal excitation equals zero.

**Diffusion** is caused by the concentration gradient. In its presence the integral movement is in the direction of the lower concentration until an equilibrium is reached. The concentration profile dissolves with time forming a Gaussian distribution with variance  $\sigma(t) = \sqrt{Dt}$  [21].

**Drift** is caused by an externally applied electrical field. In that case the carriers move along the field lines. In a sensor with a high applied field the diffusion contribution is negligible.

**Drift velocity**  $v_{drift}(E)$  is the speed at which the charge carriers drift through the diamond sensor [21].

**Mobility**  $\mu$  is a proportionality factor between the  $v_{drift}$  and the electric field  $E$  at low electric fields:  $v_{drift} = \mu E$ . Its units are in  $\text{cm}^2 \text{ V}^{-1} \text{ s}^{-1}$ .

**Phonon transport** is the transfer of energy of the moving charges to the lattice.

**Saturation velocity**  $v_{sat}^e$  is a velocity limit above which the carriers cannot reach. This is due to increasing phonon transport at a high electric field. The  $v_{sat}^e = v_{sat}^h = (14.23 \pm 0.12) \times 10^6 \text{ cm/s}$  for both positive and negative charge carriers has been derived from the measurements in [30]. The equation for  $v_{drift}$  is [31]

$$v_{drift}(E) = \mu(E)E = \frac{\mu_0 E}{1 + \frac{\mu_0 E}{v_{sat}}}. \quad (2.10)$$

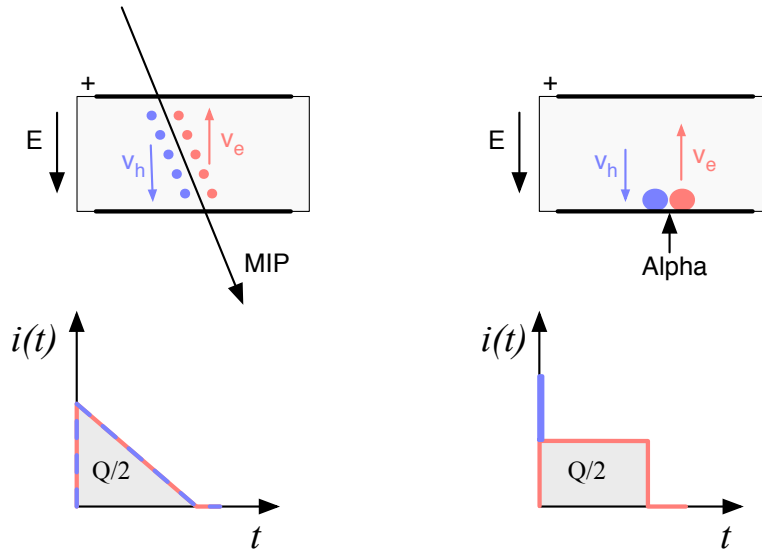


Figure 2.6: Charge carrier drift in diamond for  $\beta$  and for  $\alpha$  particles crossing the sensor at  $t = 0$ .

459 It can be retrieved experimentally via the transit time measured with the Transient Current Tech-  
 460 nique (TCT). This technique enables the measurement of transit time  $t_t$  of the carriers through the  
 461 sensor with the thickness  $d$ .

$$v_{\text{drift}}(E) = \frac{d}{t_t(E)}. \quad (2.11)$$

462 The velocities for holes and electrons usually differ. In diamond, the holes travel approximately  
 463 30 % faster than electrons at room temperature [29].

## 464 2.4 Radiation-induced current signals

465 When a highly-energetic particle travels through the sensor, it interacts with atoms in the lattice.  
 466 It ionises the valence electrons, creating electron-hole (e-h) pairs on its way. It can either deposit  
 467 only a fraction of its energy and exit the sensor on the other side or it can get stopped in the  
 468 sensor, depositing all of its energy. A special case is when it interacts with the core of the atom in  
 469 the middle of the sensor by means of a nuclear interaction. All these various types interactions  
 470 produce different amounts and different spatial distributions of e-h pairs.

471 The two most frequent types are shown in figure 2.6. The first figure shows the interaction of an  
 472 incident MIP. The electrons and holes created all along the trajectory of the particle immediately  
 473 start drifting towards the positive and negative electrode, respectively. At  $t = 0$  all charges drift  
 474 contributing to the maximum induced current. Those closest to the electrodes have a very short  
 475 drift path. They stop inducing current upon reaching the electrode. The resulting current signal  
 476 is a triangular pulse with a sharp rising edge and a linear falling edge. Gradually all the charge  
 477 carriers reach the electrode. The accumulated charge  $Q_s$  equals to the sum of the contributions of  
 478 the positive and negative charge carriers.

479 The second type of interaction happens when the particle is stopped in the diamond close to the  
 480 point of entry. Most of its energy is deposited in a small volume close to the electrode. A cloud of  
 481 charge carriers is created and the charges with the shorter path to the electrode disappear almost

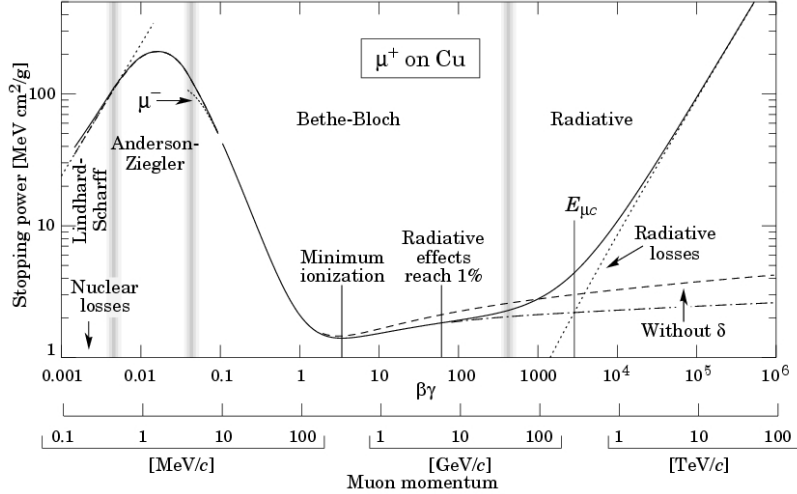


Figure 2.7: Stopping power according to the Bethe-Bloch formula [32].

instantly. The carriers of the opposite charge, however, start drifting through the sensor to the other electrode. In an ideal diamond sensor, their velocity is constant throughout the drift up until they are collected at the opposite electrode. The contribution of the first charge cloud is a peak with a short time. The cloud drifting through the sensor, on the other hand, induces a current signal with a flat top. The resulting signal has a shape of a rectangle, with a spike in the beginning. The accumulated charge  $Q_s$  is equal to a half of the deposited charge by the stopped particle.

The two aforementioned types of interactions have well defined signal responses. Nuclear interactions on the other hand yield various results. The resulting signal shape depends on the decay products of the interaction, which can be  $\alpha$ ,  $\beta$  or  $\gamma$  quanta or other nuclei, inducing a mixed shaped signal.

#### 2.4.1 Mean energy loss

A mean energy loss of a particle traversing the detector as a function of the momentum is given with the Bethe-Bloch equation [32]:

$$-\left\langle \frac{dE}{dx} \right\rangle = \frac{4\pi}{m_e c^2} \cdot \frac{n z^2}{\beta^2} \cdot \left( \frac{e^2}{4\pi\epsilon_0} \right)^2 \cdot \left( \ln \left( \frac{2m_e c^2 \beta^2}{I \cdot (1 - \beta^2)} \right) - \beta^2 \right) \quad (2.12)$$

The resulting function for a muon is shown in figure 2.7. At a momentum of around 300 MeV/c the incident particle deposits the lowest amount of energy. Hence it is referred to as the *minimum ionising particle* or a MIP.

#### 2.4.2 Signal fluctuation

Two important sensor properties are the magnitude of the signal and the fluctuations of the signal at a given absorbed energy. They determine the relative resolution  $\Delta E/E$ . For semiconductors the signal fluctuations are smaller than the simple statistical standard deviation  $\sigma_Q = \sqrt{N_Q}$ . Here  $N_Q$  is the number of released charge pairs, i.e. the ratio between the total deposited energy  $E_0$  and the average energy deposition  $E_i$  required to produce an electron-hole pair. [33] shows that the standard deviation is  $\sigma_Q = \sqrt{F N_Q}$ , where  $F$  is the Fano factor [33] (0.08 for diamond and 0.115 for silicon

## 2.4. RADIATION-INDUCED CURRENT SIGNALS

---

505 [34]). Thus, the standard deviation of the signal charge is smaller than expected,  $\sigma_Q \approx 0.3\sqrt{N_Q}$ .  
 506 The resulting intrinsic resolution of semiconductor detectors is

$$\Delta E_{\text{FWHM}} = 2.35\sqrt{FEE_i} \quad (2.13)$$

507 wherein  $E_i(Si) = 3.6$  eV and  $E_i(Di) = 13$  eV. E.g., for an  $\alpha$  particle with energy  $E_\alpha = 5.5$  MeV  
 508 the calculated resolution in diamond is equal to  $\Delta E_{\text{FWHM}} = 5.6$  keV. This defines the minimum  
 509 achievable resolution for energy spectroscopy with semiconductors.

### 510 2.4.3 Charge collection

511 The total measured charge  $Q_i$  is the integral of the induced current:

$$Q_i = \int i_{\text{ind}}(t)dt. \quad (2.14)$$

512 The expected charge  $Q_0$  can be calculated using the thickness of the sensor  $d$  and the average number  
 513 of e-h pairs created per  $\mu\text{m}$   $\delta_d$ , which is 36 e-h/ $\mu\text{m}$  for diamond according to table 2.1. The expected  
 514 charge created by a MIP flying through a sensor with a thickness  $d = 500$   $\mu\text{m}$  perpendicular to the  
 515 electrodes is

$$Q_{\text{MIP}} = \delta_d \cdot d \cdot q = 18 \times 10^3 \text{ eh} \cdot q = 2.9 \text{ fC} \quad (2.15)$$

516 where  $q = 1.6 \times 10^{-19}$  C is the elementary charge. If a particle stops in the sensor, it deposits all its  
 517 energy. In this case the number of created e-h pairs is calculated according to equation 2.16 using  
 518  $E_{\text{eh}}$ , the energy required to create an e-h pair. For diamond this value is 13, according to table 2.1.  
 519 For a 5.5 MeV  $\alpha$  particle emitted from an  $^{241}Am$  source the expected charge is

$$Q_\alpha = \frac{E}{E_{\text{e-h}}} \cdot q = \frac{5.5 \text{ MeV}}{13 \text{ eV}} \cdot q = 4.25 \times 10^5 \text{ eh} \cdot q = 68 \text{ fC}. \quad (2.16)$$

520 where  $E$  is the energy of the incident particle. which is almost for a factor of 24 larger than  
 521 expected charge of a MIP. The charge collection efficiency (CCE) is the ratio between the measured  
 522 and expected charge:

$$CCE = \frac{Q_i}{Q_0} = \frac{Q_i}{\delta_d \cdot d} \cdot 100\%. \quad (2.17)$$

523 The charge collection distance (CCD) is a measure of an average path that the charge carriers travel  
 524 before getting trapped:

$$CCD = \frac{Q_i}{\delta_d} \quad (2.18)$$

525 and is usually given in units of  $\mu\text{m}$ .

526 Carriers that get trapped stop contributing to the overall induced current on the electrodes. The  
 527 more charges are trapped along their drift path, the more the current induced on the electrodes is  
 528 decreased. This in turn yields a lower integrated charge. An expected CCE for non-irradiated sCVD  
 529 diamonds is close to 100 %. For highest quality non-irradiated pCVD diamonds it ranges between  
 530 40 % and 60 %. In other words, high-quality pCVD diamonds already have traps introduced by  
 531 means of grain boundaries, which are created in the growing process. Traps can also be created by  
 532 damaging the diamond using radiation (discussed in section 2.5). The more the sensor is irradiated,  
 533 the larger number of traps is introduced in the material and the higher is the probability that the  
 534 carriers are stopped on the way, reducing in turn the integrated charge. Therefore the CCD and  
 535 CCE can be used as a means to quantify the detector damage due to radiation.

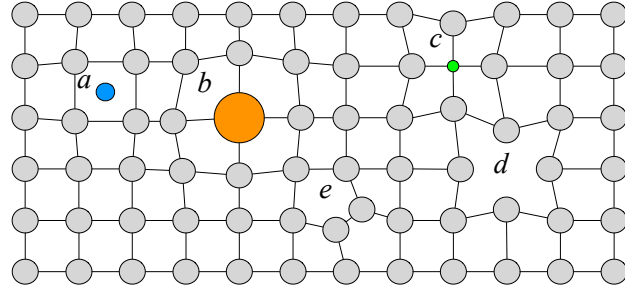


Figure 2.8: Impurities and non-uniformities in the crystal lattice due to radiation damage.

#### 536 2.4.4 Charge trapping

537 Various types of lattice defects can be created in diamond, similar to those in silicon [35]. Figure 2.8  
538 shows several examples of lattice damage:

- 539 a) foreign interstitial (e.g. H, Li),
- 540 b, c) foreign substitutional (e.g. N, P, B),
- 541 d) vacancy and
- 542 e) self interstitial.

543 These non-uniformities form new energy levels in the forbidden gap. These intermediate levels are  
544 referred to as charge traps because they can trap moving charge carriers. The energy level of the  
545 trapped carriers is reduced from the conduction band to the energy level of the trap. Different types  
546 of lattice damage have different energy levels. The carriers trapped in a shallow trap – an energy  
547 level close to the conduction band – have a high probability of being thermally excited back into the  
548 conduction band whereby they continue drifting towards the electrode. Their activation energy is  
549 therefore low. Those trapped in a deep trap close to the middle of the forbidden gap need a much  
550 higher activation energy, which in turn increases the average time to their release due to thermal  
551 excitation.

552 The energy band jumping goes the other way, too. The carriers in the valence band may use the  
553 intermediate energy levels as “stepping stones” to jump to the conduction band and start drifting in  
554 the externally applied electric field. These intermediate energy levels are referred to as the generation  
555 centres of leakage current.

556 The charge carriers that drift through the bulk get stopped in the charge traps with a certain  
557 probability. This trapping happens uniformly throughout the diamond. In other words, the number  
558 of carriers in the moving charge cloud is gradually reduced. This in turn reduces the induced current.  
559 The number of drifting carriers per unit of length follows a decaying exponential function

$$I(t) = I_0 + I(0) \cdot e^{-\frac{t-t_0}{\tau}}, \quad (2.19)$$

560 where  $I(0)$  is the initial induced current,  $I_0$  is the end current,  $t$  is time,  $t_0$  is temporal displacement  
561 of the pulse and  $\tau$  is the decay time constant. This value describes how long it takes before the  
562 amplitude of the pulse decreases to 63 % of its initial height.

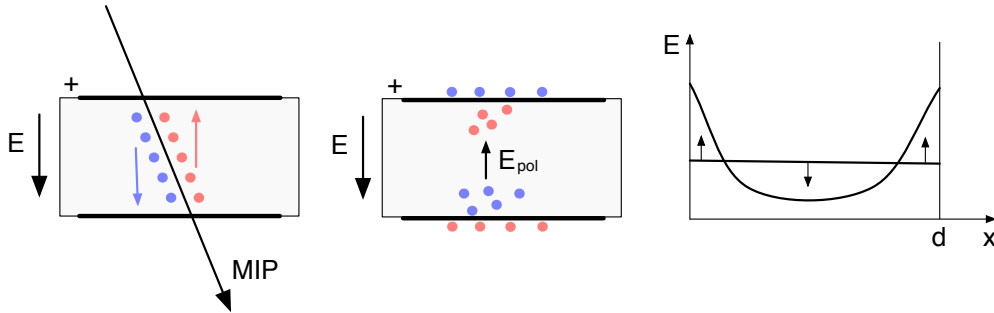


Figure 2.9: Polarisation due to space charge.

#### 2.4.4.1 Polarisation

Space charge may be introduced in the material by means of accumulating of charge carriers in local defects (i.e. charge trapping) or in the interface between the diamond and the metal electrode. The accumulated space charge deforms the electric field. This process is referred to as *polarisation*.

An example of creation of polarisation is with a MIP particle shown in figure 2.9. The created electrons and holes drift towards their respective electrodes. The amount of trapped charge is proportional to the density distribution and so the holes tend to get trapped close to the negative electrode and vice versa. The electric field formed by the trapped charge counteracts the applied electric field, leading to a reduced field in the centre of the diamond bulk. Since the electrodes are connected to a current source they charge up more due to electrostatic induction. The externally applied HV is conserved and so is the integral over the electric field. The reduction of the electric field in the centre of the bulk is compensated by an increase in electric field close to the electrodes. The actual shape of the electric field is defined by the distribution of space charge, which itself depends on the type and distribution of traps, the trapping and de-trapping times, the type of incident radiation and the rate at which charge carriers are created.

This effect is undesirable because it affects the shape of the electrical signal. Since the drift velocity of the charge carriers is proportional to the electrical field, the charge carriers change their velocity while drifting through the space charge region. Figure 2.5 compares the voltage potential, the electrical field and the space charge for an ideal sensor as well as for that with a uniformly distributed positive space charge. As discussed in [36], the main techniques to reduce polarisation are to either increase or alternate the bias voltage or to use a UV light to excite and release the trapped charges.

#### 2.4.4.2 Priming/pumping

Priming or pumping [37] is a process of irradiating the diamond with ionising radiation with a goal to improve the sensor properties. The pumping process strongly reduces the concentration of active carrier trapping centres. This leads to an enhancement of electronic properties of such material. The improved transport properties due to a reduced number of active charge traps give rise to an increased charge collection efficiency. The diamond is usually pumped for a few hours using a strong  $\beta$  source, preferably a  $^{90}\text{Sr}$  source with the activity of at least 50 MBq. The diamond remains in a pumped state from a few minutes to several days, depending on the quality of the material. A direct exposure to light results in an immediate return to an non-pumped state.

## 594 2.5 Radiation damage

595 Exposure to radiation degrades sensors by deforming the crystal lattice and introducing charge traps  
596 in the material.

597 Radiation damage varies with the type of radiation and its energy. There are several models  
598 existing [38, 39] that try to explain the impact of irradiation and to provide *damage factors* to  
599 compare the radiation damage between different particles. The standard way is to convert the  
600 damage into *1 MeV neutron equivalent fluence* [40]. Some models have been extensively verified with  
601 simulations and with experiments. In these experiments the charge collection in sensors is measured  
602 before and after irradiation. This procedure is repeated several times, with a measurement point  
603 taken after every irradiation. Then the charge collection for this set of measurements is plotted  
604 as a function of the radiation dose received by a specific particle at a specific energy. From this a  
605 damage factor  $k_\lambda$  can be extracted. Damage factors have to be measured across a range of energies  
606 and types of radiation to properly quantify the damage in the sensors. Finally they are compared  
607 to the simulations to validate the theoretical models.

608 Diamond is an expensive material and the technology is relatively new as compared to silicon.  
609 Therefore few institutes are carrying out diamond irradiation studies. To join the efforts, the RD42  
610 collaboration [41] has been formed. It gathers the experimental data from diamond irradiation  
611 studies. Unlike with silicon, the experimental results so far show no significant correlation with the  
612 NIEL (non-ionising energy loss) model [38], which correlates detector efficiency with the number of  
613 lattice displacements. Therefore an alternative model was proposed [39], correlating the diamond  
614 efficiency with the number of displacements per atom (DPA) in the material, taking recombination  
615 into account while omitting the phonon interactions. The idea is that if the recoil energy of an  
616 incident particle is higher than the lattice binding energy (42 eV for diamond), the atom is displaced  
617 from its original position. The newly formed vacancy acts as a trap for drifting charge carriers. The  
618 more displacements that form in the crystal, the higher is the probability that a drifting carrier gets  
619 trapped. However, different types of particles interact differently with the material. In addition  
620 the mechanisms of interaction at low energies are different to those at high energies. To assess  
621 the damage for individual particles at a range of energies, simulations need to be run first. The  
622 simulation shown in [39] shows the DPA model for a range of energies of proton, pion and neutron  
623 irradiation in diamond. Figure 2.10 contains the simulation results as well as the superimposed  
624 empirical results of several irradiation campaigns. According to the figure, a 300 MeV pion beam  
625 damages the diamond material twice as much as a 24 GeV proton beam. The data points obtained  
626 by RD42 are also added to the figure. They have been normalised to damage by 24 GeV protons.  
627 This value has been chosen because radiation damage at this energy and radiation type is well  
628 understood at CERN.

### 629 2.5.1 Irradiation damage factor

630 The irradiation damage factor  $k_\lambda$  is a means to quantify irradiation damage of a specific type of  
631 radiation at a specific energy. Via this factor different types of irradiation can be compared. It is  
632 obtained experimentally by measuring the CCD of a number of samples at various irradiation steps  
633 and fitting the equation 2.20 to the data.  $\lambda$  is the measured CCD,  $\lambda_0$  is the CCD of a non-irradiated  
634 sample and  $\Phi$  the radiation dose. As a reference, the damage factor for 24 GeV protons is set to  
635  $1 \times 10^{-18} \mu\text{m}^{-1} \text{cm}^{-2}$ .

$$\frac{1}{\lambda} = \frac{1}{\lambda_0} + k_\lambda \cdot \Phi \quad (2.20)$$

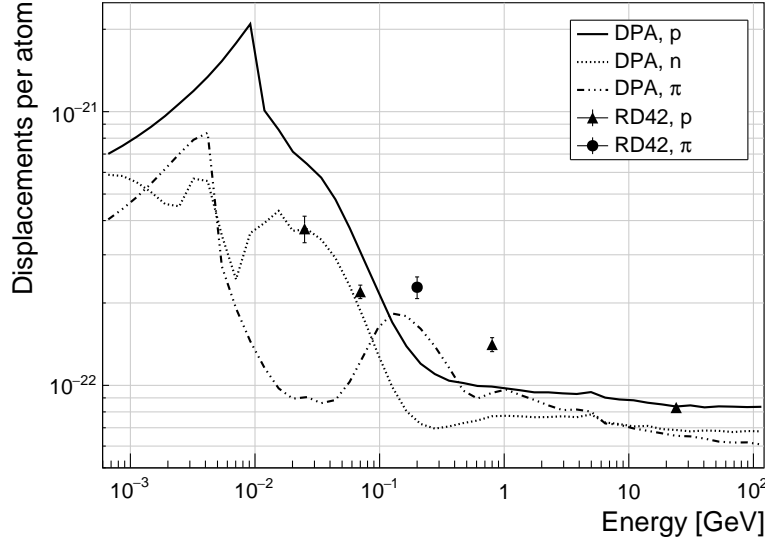


Figure 2.10: Diamond radiation damage - a model based on displacements per atom [39]. The figure shows the DPA as a function of the kinetic energy for protons, neutrons and pions. Added are data points for protons and pions by RD42 [42].

## 636 2.6 Temperature effects

637 The band gap energy in diamond is equal to  $E_g = 5.5$  eV while the average energy to produce an  
 638 electron-hole pair is  $E_{e-h} = 13$  eV. This means there is excessive energy deposited in the diamond  
 639 bulk. An incident  $\alpha$ -particle stops within  $\sim 10\text{--}15 \mu\text{m}$  of the bulk, transferring all its energy to the  
 640 lattice during deceleration. A part of this energy directly ionises the carbon atoms, creating free  
 641 electron-hole pairs.

642 The remaining energy, however, is converted into lattice vibrations – phonons [43, 29]. In other  
 643 words, the lattice within the ionisation volume of approximately  $\sim 15 \mu\text{m} \times \sim 2 \text{ nm}$  [29] is briefly  
 644 heated up. The hot plasma then cools down to the temperature of the surrounding material by  
 645 means of heat dissipation, i.e. phonon transport.

646 The free electron binds with the free hole into a bound state (not recombination) – the ex-  
 647 citon [44]. The exciton binding energy is 80 meV, which introduces an energy level within the  
 648 forbidden gap just under the conduction band. At higher temperatures the lattice provides enough  
 649 energy to thermally excite the electron from the exciton state back to the conduction band. At lower  
 650 temperatures, however, the exciton lifetime increases, which means that it takes a longer time for the  
 651 electrons to get re-excited to the conduction band. The re-excitation lifetime at room temperature  
 652 is  $\sim 30$  ps, increasing to  $\sim 150 \mu\text{s}$  at 50 K [29]. This means that some of the bound electrons do not  
 653 even start drifting within the period of  $\sim 10$  ns, which is the expected carrier drift time. When they  
 654 are finally freed, the current they induce is already hidden in the electronics noise. The effective  
 655 area of the observed current pulse is therefore smaller than that of a pulse induced by all the carriers  
 656 drifting at the same time. This in effect reduces the measured collected charge. The longer the time  
 657 constant, the lower the measured collected charge, as shown in section 3.4.2.1.

**658 2.6.1 Collected charge as a function of temperature**

659 The area below the current pulse is proportional to the charge collected by the diamond detector.  
 660 The collected charge is measured as a function of temperature. First, the amplitude values of the  
 661 averaged pulses at a bias voltage of  $\pm 500$  V and across the temperature range between 4 K and  
 662 295 K have to be integrated. Then a calibration factor is used to derive the charge for all data  
 663 points. The results of such measurements have been presented in [29]. Chapter 3 shows the results  
 664 of the measurements taken in the scope of this thesis.

**665 2.7 Electronics for signal processing**

666 This section describes the electronics of a detector, starting with a description of signal amplifiers  
 667 and then discussing the digitisation and signal processing. All these stages are necessary to extract  
 668 information from the sensor. First, the signal has to be amplified. Then it is digitised and finally  
 669 processed in a specially designed processor or a logic unit. A more detailed description of the detector  
 670 chain can be found in [45].

**671 2.7.1 Signal preamplifiers**

672 The signal charge generated in the sensor by a single energetic particle is of the order of a few fC.  
 673 The range of the induced current for single particles is typically between  $10^{-8}$  A ( $\beta, \gamma$  radiation)  
 674 and  $3 \times 10^{-7}$  A ( $\alpha$  radiation). Signals as low as these have to be pre-amplified before processing.  
 675 Depending on the measurement, several types of signal amplifiers can be used. The preamplifiers  
 676 are designed to minimise electronic noise while maximising gain, thus maximising the signal-to-  
 677 noise ratio (SNR). In addition, a bandwidth limit must be optimised to minimise the information  
 678 loss due to signal shape deformation. A critical parameter is the total capacitance, i.e. the sensor  
 679 capacitance together with the capacitance load of the preamplifier. The SNR improves with a lower  
 680 capacitance. Several types of amplifiers can be used, all of which affect the measured pulse shape.  
 681 Two preamplifiers are used most commonly, a current and a charge sensitive amplifier. Both are  
 682 described below.

**683 2.7.1.1 Current amplifier**

684 Figure 2.11a shows the equivalent circuit of a current source and a current amplifier. An amplifier  
 685 operates in current mode if the source has a low charge collection time  $t_c$  with respect to the  $R_i C_d$   
 686 time constant of the circuit. In this case the sensor capacitance discharges rapidly and the output  
 687 current  $i_o$  is proportional to the instantaneous current  $i_i$ . The amplifier is providing a voltage gain,  
 688 so the output signal voltage  $u_o$  is directly proportional to the input voltage  $u_i$ :

$$u_o(t) = A \cdot R_i \cdot i_i(t), \quad (2.21)$$

689 whereby  $i(t)$  is the induced current calculated using the Shockley-Ramo theorem.

690 The detector capacitance  $C_d$  together with the input resistance of the amplifier  $R_i$  defines the  
 691 time constant of the signal, as shown in figure 2.11b. The higher  $C_d$ , the slower is the response of  
 692 the amplifier. For the case of the diamond sensor, which has the capacitance of the order of 2 pF  
 693 and the input resistance of  $50 \Omega$ , the resulting time constant is  $\tau = 10^{-10}$  s. This yields the signal  
 694 rise time  $t_r \sim 2.2\tau = 2.2 \times 10^{-10}$  s.  $t_r$  is a function of the input bandwidth limit:

$$t_r = \frac{0.34}{BW} \quad (2.22)$$

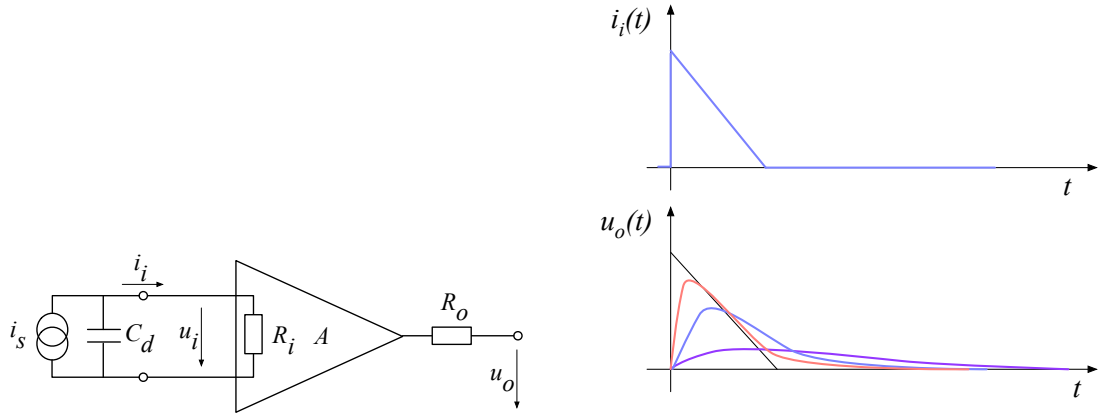


Figure 2.11: Left: a simplified equivalent circuit of a current amplifier. Right: an input and an output signal of the current amplifier.

695 where BW is the cutoff frequency. To ensure that the signal is not distorted significantly, the  $t_r$   
 696 must be shorter than 10 % of the pulse width:

$$t_r < \frac{\text{FWHM}}{10}. \quad (2.23)$$

697 For a 500  $\mu\text{m}$  thick diamond with a bias voltage of 500 V and electron collection, the drift velocity  
 698 is  $v_{\text{drift}} = 6 \times 10^6 \text{ cm/s}$  [29]. An  $\alpha$  particle with the energy of 5.5 MeV induces a current

$$i(t) = \frac{Q}{d} v_{\text{drift}} = 8 \mu\text{A} \quad (2.24)$$

699 where  $Q=68 \text{ fC}$  according to equation 2.16. The drift time  $t_{\text{drift}}$  of charge carriers through the sensor  
 700 equals the pulse FWHM and is

$$\text{FWHM} = t_d = \frac{d}{v_{\text{drift}}} = 8.3 \text{ ns}, \quad (2.25)$$

701 which means that the maximum rise time must be  $t_r = 0.83 \text{ ns}$  according to equation 2.23. The  
 702 minimum bandwidth limit for observing  $\alpha$  pulses for such a system is therefore 400 MHz according  
 703 to equation 2.22.

### 704 2.7.1.2 Charge-sensitive amplifier

705 In order to measure integrated charge in the sensor, a feedback loop is added to the amplifier, as  
 706 shown in figure 2.12a. The feedback can be used to control the gain and input resistance, as well  
 707 as to integrate the input signal. The charge amplifier is in principle an inverting voltage amplifier  
 708 with a high input resistance.

709 In an ideal amplifier the output voltage  $u_o$  equals  $-Au_i$ . Therefore the voltage difference across  
 710 the capacitor  $C_f$  is  $u_f = (A + 1)u_i$  and the charge deposited on the capacitor is

$$Q_f = C_f u_f = C_f (A + 1) u_i. \quad (2.26)$$

711 Since no current can flow into the amplifier, all of the signal current must charge up the feedback  
 712 capacitance, so  $Q_f = Q_i$ .

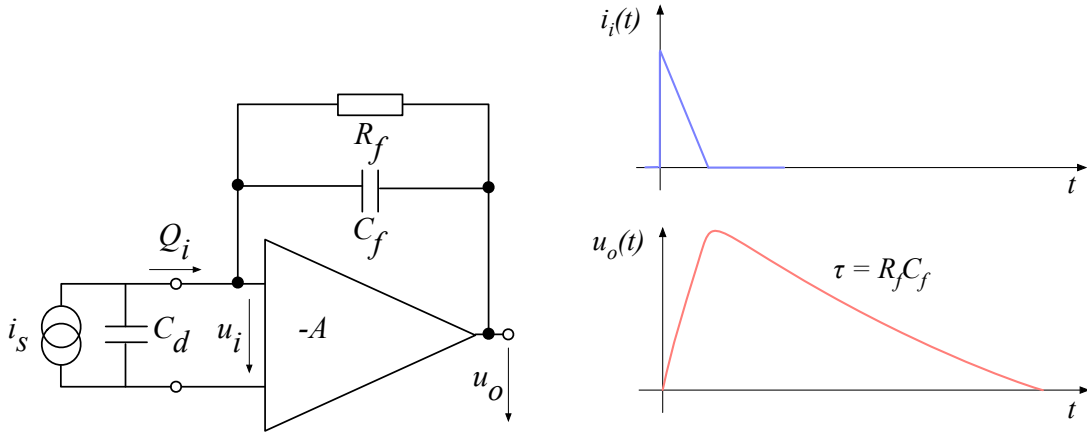


Figure 2.12: Left: a simplified equivalent circuit of a charge amplifier. Right: an input and an output signal of the charge amplifier.

713 In reality, however, charge-sensitive amplifiers respond much slower than is the duration of the  
 714 current pulse from the sensor. In addition, a resistor is added to the feedback line in parallel to  
 715 the capacitor. The resistor and capacitor define the decay time constant of the pulse, as shown  
 716 in figure 2.12b. This is necessary to return the signal to its initial state to be ready for a new  
 717 measurement.

718 A MIP deposits 2.88 fC in a 500  $\mu\text{m}$  thick diamond. In a pCVD diamond sensor with a quoted  
 719 CCE of 35 % the MPV of the collected charge is 1 fC. The low and high end of the Landau distribution  
 720 are at  $\frac{2}{3} \times \text{MPV}$  and  $10 \times \text{MPV}$ , therefore at 0.67 fC and 10 fC. To ensure a good separation between  
 721 the noise floor and the signal, the noise RMS must be 5 times lower than the signals with the lowest  
 722 charge deposition – below 0.133 fC, which equals  $836 \text{ e}^-$ . For an amplifier with the gain of 10 mV/fC  
 723 with such a noise floor, the voltage noise RMS on the output is 1.3 mV.

### 724 2.7.2 Analogue electronic noise

725 The electronic noise determines the ability of a system to distinguish different signal levels. The  
 726 analogue signal contains ample information about the type and energy of incident radiation, which  
 727 can quickly be erased or altered if the signal properties change. Therefore the noise contributions  
 728 to the signal must be well understood to qualify the information the signal is carrying. In electrical  
 729 circuits there are five common noise sources:

- 730 - Thermal noise
- 731 - Shot noise
- 732 - Flicker noise
- 733 - Burst noise
- 734 - Avalanche noise.

735 The last two contributions can be eliminated if present, so the focus is on the first three.

## 2.7. ELECTRONICS FOR SIGNAL PROCESSING

---

Considering  $n$  carriers of charge  $e$  moving with a velocity  $v$  through a sample of length  $l$ , the induced current  $i$  at the ends of the sample is

$$i = \frac{Q \cdot v_{\text{drift}}}{d} = \frac{nev}{d} \quad (2.27)$$

where  $d$  is the distance travelled. Two mechanisms contribute to the total noise: velocity fluctuations (thermal noise) and number fluctuations (shot noise, flicker noise). They are statistically uncorrelated and can therefore be added in quadrature.

**Thermal noise** or Johnson–Nyquist noise [46, 47] is the dominant noise contribution in the use case for diamond detector signal amplification and therefore defines the limitations of the detector system. This noise type is generated by the random thermal motion of charge carriers. The frequency range of the thermal noise is from 0 to  $\infty$  with a predominantly uniform distribution (white noise). The resulting signal amplitude has a Gaussian distribution. The spectral noise voltage density is

$$e_n^2 = 4k_B RT \quad (2.28)$$

where  $k_B$  is the Boltzmann constant,  $R$  is the input resistance of the amplifier and  $T$  its temperature. The total noise on the output depends on the frequency [48]:

$$u_{\text{on}}^2 = \int_0^\infty e_n^2 A^2(f) df. \quad (2.29)$$

Assuming a uniform gain across the frequency range between the low and the high cut-off  $\Delta f = f_{\text{max}} - f_{\text{min}}$ , the equation is simplified into

$$u_o = A \sqrt{4k_B RT \Delta f}, \quad (2.30)$$

where  $u_o$  is the RMS of the open-loop equivalent voltage. This equation shows that it is possible to reduce the noise RMS by either (1) reducing the input bandwidth, (2) reducing the resistance or (3) decreasing the temperature.

**Shot noise** occurs whenever charge carriers are injected into a sample volume independently of one another. The spectral noise current density in this case is proportional to the DC current:

$$e_i^2 = 2qI. \quad (2.31)$$

**Flicker noise** occurs when charge carriers are trapped and then released after a characteristic time  $\tau$ . For a number of traps with different  $\tau$ , the spectral noise density yields a near  $1/f$  distribution [48]. This noise contribution becomes more pronounced in heavily irradiated sensors with a high number of introduced charge traps.

### 2.7.3 Analogue-to-digital converters

An analogue-to-digital converter (ADC) is a device that converts the analogue electrical signal on the input to its digital representation – a series of digital values. This involves a quantisation – *sampling* of the signal at a defined sampling period, resulting in a sequence of samples at a discrete time period and with discrete amplitude values. The resolution of the ADC is the number of output levels the ADC can quantise to and is expressed in bits. For instance, an ADC with a resolution equal to  $n = 8$  bit has a dynamic range of  $N = 2^n = 256$  steps. The resulting voltage resolution  $Q_{\text{ADC}}$  at the input voltage range of  $V_{\text{ADC}} = \pm 50$  mV is then

$$Q_{\text{ADC}} = \frac{V_{\text{ADC}}}{2^n} = \frac{100 \text{ mV}}{2^8 \text{ bit}} = 0.39 \text{ mV/bit}. \quad (2.32)$$

With a sampling period of  $t_s = 1$  ns the sampling rate is  $f_s = 1$  GS/s (gigasample per second).

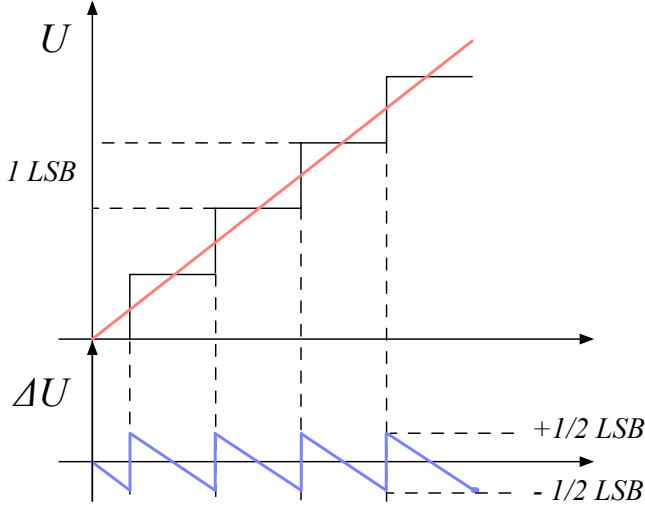


Figure 2.13: Input signal digitisation and quantisation error.

**Quantisation error and quantisation noise** (or a round-off error) is a contribution to the overall measurement error due to digitisation (rounding). The quantisation error is defined as a difference between the actual analog value and the closest digitised representation of this value, therefore by the least significant bit (LSB), as seen in figure 2.13. The input signal amplitude is typically much larger than than the voltage resolution. In this case the quantisation error is not directly correlated with the signal and has an approximately uniform distribution. The probability density function  $P(x)$  therefore has a rectangular shape bounded by  $(-\frac{1}{2}\text{LSB}, \frac{1}{2}\text{LSB})$ :

$$P(x) = \begin{cases} \frac{1}{\text{LSB}}, & -\frac{1}{2}\text{LSB} \leq x \leq \frac{1}{2}\text{LSB} \\ 0, & \text{otherwise.} \end{cases} \quad (2.33)$$

<sup>768</sup> The height equal to  $\frac{1}{\text{LSB}}$  preserves the integrated probability of 1. The variance of the distribution  
<sup>769</sup> is

$$\sigma^2 = \int P(x)(x - \mu)^2 dx. \quad (2.35)$$

<sup>770</sup> The population mean is  $\mu = 0$ , therefore

$$\sigma^2 = \int_{-\frac{1}{2}\text{LSB}}^{\frac{1}{2}\text{LSB}} \frac{1}{\text{LSB}} x^2 dx = \frac{x^3}{3\text{LSB}} \Big|_{-\frac{1}{2}\text{LSB}}^{\frac{1}{2}\text{LSB}} = \frac{\text{LSB}^2}{12}. \quad (2.36)$$

<sup>771</sup> The RMS of the quantisation noise is defined as the square root of the variance:

$$\Delta Q_{\text{ADC}} = \sqrt{\sigma^2} = \frac{1}{\sqrt{12}} \text{LSB} \sim 0.289 \text{ LSB}. \quad (2.37)$$

<sup>772</sup> For the example above the quantisation error equals  $\Delta Q_{\text{ADC}} = 0.11 \text{ mV}$ . The error depends strongly  
<sup>773</sup> on the linearity of the ADC, but this is out of scope of this document as the devices used have ADCs  
<sup>774</sup> with a very good linearity.

775 **2.7.4 Digital signal processing**

776 The digitised signal can be processed to extract useful information. Therefore after the signal  
777 amplification and digitisation the signal is routed in a device which handles the digital analysis. The  
778 signal can either be processed immediately (in real time) or it can be saved to a data storage for  
779 analysis at a later stage (offline). The devices carrying out the processing can be multipurpose (e.g.  
780 Field Programmable Gate Arrays) or dedicated (e.g. Application-Specific Integrated Circuits).

781 **Field Programmable Gate Array** (FPGA) is an integrated circuit designed to be reprogrammable  
782 and reconfigured after manufacturing. It consists of a set of logic gates that can be interconnected in  
783 numerous combinations to carry out a set of logic operations. Many such logic operations can take  
784 place in parallel, making the FPGA a powerful tool for signal processing. FPGAs are often used  
785 during system development or in systems in which the requirements might change with time. They  
786 can be reprogrammed in the order of seconds. In addition, the logic design only needs minor changes  
787 when migrating to a newer version of the FPGA chip of the same vendor. The FPGAs also offer  
788 faster time-to-market with comparison to application-specific solutions, which have to be developed.  
789 On the other hand, the price per part can be significantly higher than for the application-specific  
790 solutions. Also, their other major disadvantages are a high power consumption and a relatively  
791 low speed as compared to more application-specific solutions. However, today's solutions are ca-  
792 pable of clock speeds higher than 500 MHz. Together with the integrated digital signal processing  
793 blocks, embedded processors and other modules, they are already very powerful and versatile. All  
794 in all, FPGAs are a good choice for prototyping and limited production, for projects with limited  
795 requirements for speed and complexity.

796 **Application-Specific Integrated Circuit** (ASIC) is an integrated circuit designed for a specific  
797 use. The design cannot be modified after chip production, as is the case with FPGAs. On the other  
798 hand, the ASICs can be optimised to perform a required operation at a high speed and at a low  
799 power consumption. In addition, due to the specific design the size of the chip can be much smaller.  
800 ASICs can be designed as hybrid chips, containing both a digital and an analog part. Finally, ASICs  
801 can be designed to withstand much higher irradiation doses than FPGAs and can therefore be used  
802 in harsh environments like in space or in particle colliders. To update the chip, the design has to be  
803 submitted to a foundry, which produces the new chips with a turnover time of 4—6 weeks. The costs  
804 of a submission are high, but the price per part can be reduced significantly with a high volume.  
805 To sum up, ASICs are used for high volume designs with well defined requirements where some  
806 stringent constraints in terms of power consumption and speed have to be met.

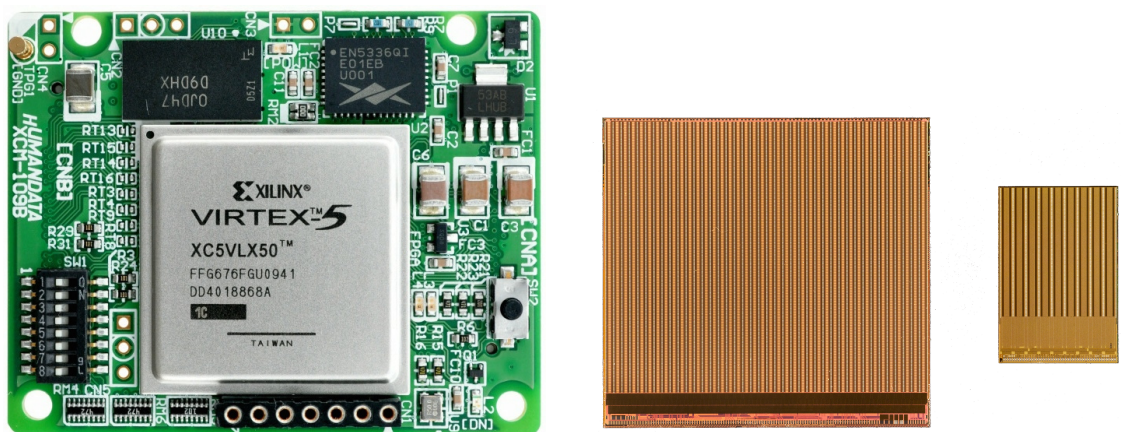


Figure 2.14: An example of a Xilinx Virtex 5 FPGA [49] and an FE-I4 and FE-I3 ASIC chip [50].



807 **Chapter 3**

808 **Diamond irradiation study**

809 The aim of the study in this chapter is to find the operational limitations of diamond detectors  
810 for spectroscopy and tracking applications. The chapter contains the measurement results of data  
811 taken with diamond sensors. First the measurement setup is described in section 3.1. Then the  
812 measured particle spectra are shown in 3.2. This is followed by a study of effects of the irradiation  
813 damage on the electrical signal of the diamond detector. The last section shows the results of the  
814 measurements of irradiated diamond samples at cryogenic temperatures. The studies compare the  
815 experimentally acquired data with the theory from the previous chapter and define limitations of  
816 the diamond detectors in terms of radiation and temperature.

817 Diamond sensors are mainly used for two types of measurements: particle counting and spec-  
818 troscopy. The first type of measurements depends on the sensor efficiency – its ability to detect all  
819 or at least a known percentage of incident particles. The energy of the particles is not so impor-  
820 tant; what bears the information is the rate and the spatial distribution. Here the particles do not  
821 necessarily stop in the bulk – they exit the sensor with a slightly lower energy. In spectroscopy,  
822 on the other hand, the particles stop within the sensor, depositing all their energy. This energy is  
823 then measured by collecting the freed charge carriers. The goal of the experiments described in this  
824 chapter is to:

- 825 1. Quantify the efficiency of the sCVD diamond in counting mode,
- 826 2. Quantify the degradation of the efficiency as a function of fluence,
- 827 3. Quantify the macroscopic effects on charge carrier behaviour as a function of the fluence and
- 828 4. Define limitations for use in spectroscopy.

829 The results discussed here show that there are several limitations for using diamond as a radiation  
830 detector. All of them need to be taken into account when designing a new measurement device.  
831 The irradiation study allows for an estimation of the lifetime of the detector and a prediction of the  
832 longterm signal degradation as a function of fluence. The result of the study is a correction factor,  
833 which can be applied during data analysis to ensure that the analysis results are stable despite the  
834 detector degradation.

835 **3.1 Measurement setup**

836 The first step of designing a measurement setup is to define the measurement conditions, such as  
837 the temperature, the type of radiation and its flux. The second step is to ensure that the setup

### 3.1. MEASUREMENT SETUP

---

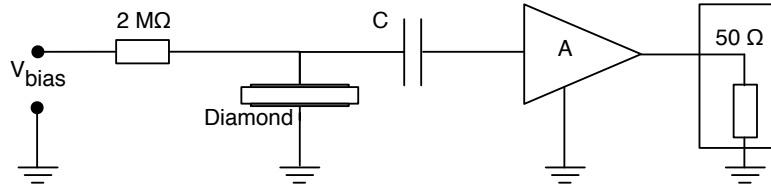


Figure 3.1: Diagram of a diamond detector readout chain.

838 is insensitive to external electromagnetic interferences and that it minimises electrical noise in the  
839 system. The setup needs to be calibrated before use.

840 The measurements using diamond that are explained in these chapters have been carried out  
841 using several measurement setups, but they are all similar in terms of the electrical signal chain.  
842 The measurement chain consists of three main parts: a diamond sensor, a signal preamplifier and a  
843 readout device, as seen in figure 3.1. The signals propagating along the analogue chain are fast – in  
844 the GHz bandwidth range – and with low amplitudes – of the order of tens of  $\mu\text{V}$ . This gives rise  
845 to the importance of shielding from external radio-frequency (RF) interferences. Also, the carrier  
846 and the preamplifier have to have a matched impedance. Finally, the system needs to be grounded  
847 properly.

#### 848 3.1.1 Preamplifiers

849 Two preamplifiers are used for the measurements, one sensitive to charge and the other to current.  
850 *CIVIDEC Cx* (figure 3.2a) is a charge sensitive amplifier. Its high SNR is achieved due to a low  
851 equivalent noise charge of  $300 \text{ e}^-$  with an additional  $30 \text{ e}^-$  per each pF of the sensor capacitance. A  
852 reported gain of  $\sim 12 \text{ mV/fC}$  makes it a good choice for spectroscopic measurements with diamond  
853 sensors. *CIVIDEC C2* (figure 3.2b) [45] is a fast current preamplifier with a 2 GHz bandwidth limit.  
854 Both are embedded in an RF-tight aluminium box to reduce the noise pickup. Both have an AC  
855 coupled input and a  $50 \Omega$  output.

856 A 2 GHz bandwidth limit defines the minimum rising time equal to  $t_r \simeq \frac{0.34}{BW} = \frac{0.34}{2 \times 10^9} = 170 \text{ ps}$ ,  
857 therefore the system with a CIVIDEC C2 amplifier is capable of measuring pulses with a minimum  
858 FWHM  $\simeq 170 \text{ ps}$ . The initial peak in the  $\alpha$  pulse has a lower FWHM; for example, if a charge  
859 carrier travelling through the bulk takes  $t_1 \sim 6 \text{ ns}$  to reach the electrode on the opposite side  
860 ( $d_1 \sim 500 \text{ }\mu\text{m}$ ), the carrier with the opposite charge and a shorter path to the closer electrode –  
861 max.  $d_2 \sim 10 \text{ }\mu\text{m}$  – only takes  $t_2 \sim \frac{d_2}{d_1} t_1 = 120 \text{ ps}$ . Such a short drift time induces a current pulse  
862 that is too narrow for the system to detect.

##### 863 3.1.1.1 Calibration

864 The amplifiers have to be calibrated before use to determine their gain. Both are calibrated using a  
865 square signal generator with a known amplitude step of  $U_{\text{in}} = (252 \pm 5) \text{ mV}$ . A 2 GHz oscilloscope  
866 with a 10 GS/s sampling rate is used to carry out the calibration.

867 **Cx charge sensitive amplifier** calibration necessitates an injection of a well known charge. There-  
868 fore the signal from a pulse generator is routed through a capacitor with a calibration capacitance  
869  $C_{\text{cal}} = (0.717 \pm 0.014) \text{ pF}$  and then to the input of the amplifier. The pulse area behind the capacitor  
870 is  $a_{\text{cal}} = (5.0 \pm 0.5) \text{ pVs}$ , with the signal amplitude on the output amounting to  $U_{C_x} = (1.95 \pm 0.05) \text{ V}$ .

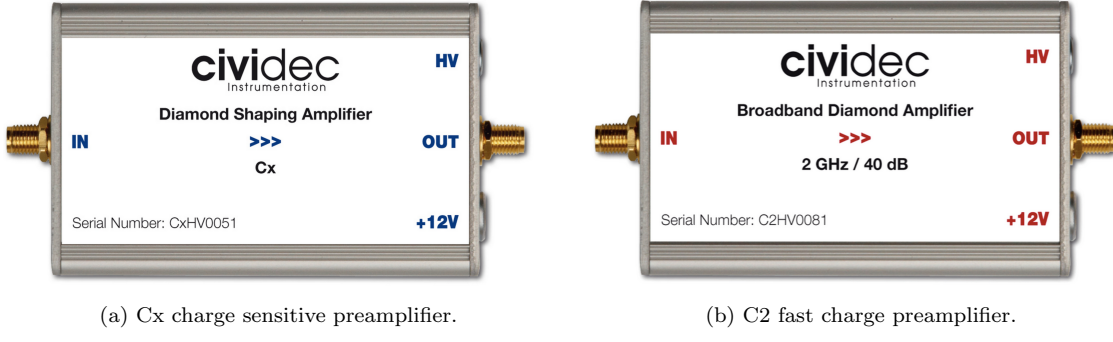


Figure 3.2: Amplifiers used for the charge and current measurements.

871 The input voltage step combined with the calibration capacitance yields a calibration charge

$$Q_{\text{cal}} = C_{\text{cal}} \cdot U_{\text{in}} = (181 \pm 5) \text{ fC}. \quad (3.1)$$

872 The gain of the Cx amplifier when comparing the integrated input charge to the output amplitude  
873 is

$$A_{\text{Cx}}^{\text{Q}} = \frac{U_{\text{Cx}}}{Q_{\text{cal}}} = (9.3 \pm 0.4) \text{ mV/fC} \quad (3.2)$$

874 whereas the factor between the area of the input current pulse and the output amplitude is

$$A_{\text{Cx}}^{\text{a}} = \frac{U_{\text{Cx}}}{a_{\text{cal}}} = (390 \pm 40) \text{ mV/pVs}. \quad (3.3)$$

875 The area-based amplification factor  $A_{\text{Cx}}^{\text{a}}$  can be used as an estimate for the integrated charge of a  
876 current pulse. However, it has a higher uncertainty ( $\sim 10\%$ ) than the amplitude-based factor  $A_{\text{Cx}}^{\text{Q}}$   
877 ( $\sim 4\%$ ) due to the measurement limitations of the oscilloscope.

878 **C2 current amplifier** calibration only requires the measurement of the amplitude gain. To keep  
879 the output signal amplitude within the  $\pm 1$  V linear range of the amplifier, the input signal amplitude  
880 has to be minimised. The signal from the generator is therefore routed through a 36 dB attenuator  
881 to decrease its amplitude to  $U_{\text{inAtt}} = (3.95 \pm 0.05)$  mV. Two amplifiers with different gains have been  
882 measured, because both are used for the measurements. The output of the first amplifier amounts  
883 to  $U_{\text{C2-1}} = (860 \pm 5)$  mV. This yields the amplification gain

$$A_{\text{C2-1}} = \frac{U_{\text{inAtt}}}{U_{\text{C2-1}}} = (217 \pm 3). \quad (3.4)$$

884 The second amplifier has the output equal to  $U_{\text{C2-2}} = (632 \pm 5)$  mV with the resulting gain of  
885  $A_{\text{C2-2}} = (152 \pm 3)$ .

### 886 3.1.2 Diamond samples

887 The sensor samples used for these studies have been acquired from Element Six (E6) [51]. They all  
888 have the same standard dimensions. sCVD diamonds with dimensions  $4.7 \times 4.7 \text{ mm}^2$  are already  
889 sufficiently large for most of the beam monitoring applications and still affordable. One sample  
890 with dimensions of  $5.6 \times 5.3 \text{ mm}^2$  produced by IIa Singapore [52] has also been characterised at  
891 CERN [53]. The target thickness for all samples is 500  $\mu\text{m}$ . Diamonds this thick yield a high  
892 enough signal-to-noise ratio for MIPs to be measured by the available electronics. Table 3.1 shows

### 3.1. MEASUREMENT SETUP

---

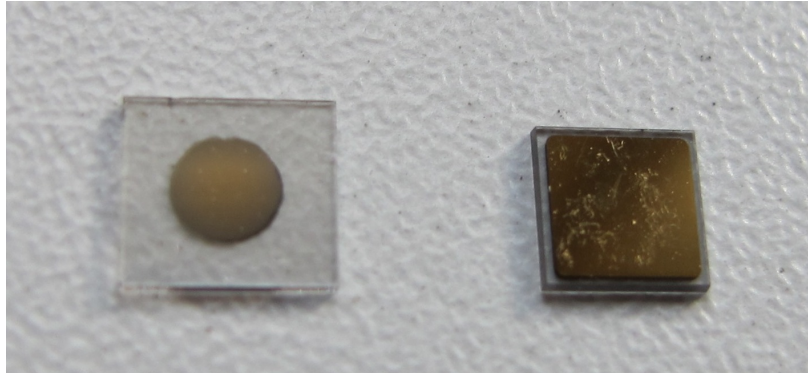


Figure 3.3: Two scCVD diamond samples: A IIa 1scdhq (left) and an E6 S37 (right).

893 all the samples used for this study. Two of them are measured before and after irradiation and then  
 894 compared. Irradiation doses for damaging the material need to be high – above  $10^{12}$  particles per  
 895  $\text{cm}^2$  to be able to observe a significant change in behaviour of a diamond sensor.

Name	Type	Producer	Dimensions [mm <sup>2</sup> ]	Thickness [μm]	Electrode	Irradiated
S37	sCVD	E6	4.7 × 4.7	548	Cr/Au	no
S50	sCVD	E6	4.7 × 4.7	537	Cr/Au	no
S52	sCVD	DDL	4.7 × 4.7	515	DLC/Pt/Au	$3.6 \times 10^{14} \frac{\text{n}}{\text{cm}^2}$
S79	sCVD	E6	4.7 × 4.7	529	Cr/Au	$1 \times 10^{14} \frac{\text{n}}{\text{cm}^2}$
ELSC	sCVD	E6	4.7 × 4.7	491	Cr/Au	no
1scdhq	sCVD	IIa	5.6 × 5.3	460	Cr/Au	no

897 Table 3.1: Diamond sensor samples used.

898 The diamond samples have quoted impurity densities of  $\leq 2 \times 10^{14} \text{ cm}^{-3}$  and nitrogen incorpo-  
 899 ration of  $\leq 10^{-9}$ . The electrodes were added by various companies and institutes. For instance, S52  
 900 was metallised by a company DDL (now defunct) while the Physics Department of the University  
 901 of Firenze, Italy metallised the S79. There are also several techniques for producing the electrodes.  
 902 The DDL contacts consist of three layers: DLC (diamond-like carbon)/Pt/Au with 4/10/200 nm  
 903 thicknesses, respectively. The metallisation for S79, on the other hand, is made up of Cr/Au with  
 904 a total thickness of  $\sim 400$  nm. The area coverage also differs from sample to sample. Diamonds  
 905 must not be metallised until the very edge as the proximity of contacts with a high potential may  
 906 lead to sparking. However, the areas not covered by the metallisation are less efficient because the  
 907 fringe fields at the edges are not as strong as in between the electrodes. This effectively reduces  
 908 the sensitive area of the sensors. In the diamonds used here the effective area is anywhere from  
 909 9 mm<sup>2</sup> to 18 mm<sup>2</sup>. The leakage current is below 1 nA, but increases for the irradiated samples. The  
 910 capacitance is of the order of  $(2.0 \pm 0.3)$  pF.

#### 911 3.1.3 Readout devices

912 Electrical signals in diamond detectors are in the GHz frequency range. To preserve the information  
 913 in the signals, the readout device with a high bandwidth limit must be used. For instance, a 20 MHz  
 914 limit is enough for the spectroscopic measurements with the Cx charge amplifier, but is insufficient  
 915 for the current measurements with the C2 amplifier.

916 Two devices are used take data shown in this chapter. The first choice is a 2 GHz LeCroy  
 917 WaveRunner 204MXi-A. This specific model has a sufficiently high bandwidth limit for the fast  
 918 current preamplifier signals. It offers a reliable solution for analogue signal readout of limited

919 amounts of data. However, its slow acquisition speed is a bottleneck in a test beam experiment. Its  
920 initial 100 Hz readout rate decreases to a mere 20 Hz within 20 minutes, because every single trigger  
921 is saved as a separate file and the Windows operating system is not capable of handling 10'000+  
922 files in a single directory easily. This is why it has been exchanged with a DRS4 [54], an analogue  
923 readout device developed by PSI, Switzerland. This compact device is capable of recording up to  
924 four waveforms at a time at a steady rate of up to 500 Hz. Its 700 MHz bandwidth limitation is  
925 sufficient for the signal from the charge amplifier.

### 926 3.1.4 Setup for the $\beta$ detection efficiency study

927 The efficiency study of the diamond sensors has been carried out at CERN in the North Hall test  
928 beam facility. There a straight high-energy particle beam of 120 GeV  $\pi$  is provided to the users  
929 to calibrate their detectors. The beam has a transverse spread of  $\sigma = 10$  mm in both axes. The  
930 particle rate is of the order of  $10^4 \pi \text{ cm}^{-2} \text{ s}^{-1}$ . A diamond sensor embedded in a printed circuit  
931 board (PCB) carrier has been placed in the beam spot perpendicular to the beam and connected via  
932 an SMA connector directly to a charge amplifier. The amplified signal is read out using a LeCroy  
933 oscilloscope and a DRS4 analogue readout system. A computer is used as a controller and data  
934 storage for the readout device. A beam telescope is used as a reference detector. It is a device that  
935 helps to cross-check the measurements of the devices under test (DUTs) and to carry out spatially  
936 resolved studies on the DUTs. It consists of several pixellated sensor planes placed in series, which  
937 can track a particle's trajectory with a precision of a few  $\mu\text{m}$ . The sensor planes are positioned in  
938 front of the DUT and behind it. Then the beam telescope acts as a trigger system – it triggers the  
939 readout of both the telescope data and DUT data when both the planes in front and behind the  
940 DUT record a hit by an incident particle. A particle detected by all the planes within the DUT  
941 window and the DUT itself counts towards its efficiency whereas a hit missed by the DUT means  
942 that the DUT is not 100 % efficient. To discard the hits that miss the DUT completely, a region of  
943 interest (ROI) can be chosen in the beam telescope planes. The equation for calculating the sensor  
944 efficiency is therefore

$$\epsilon = \frac{N_{\text{DUT}} \wedge N_{\text{telescope}}}{N_{\text{telescope}}} \quad (3.5)$$

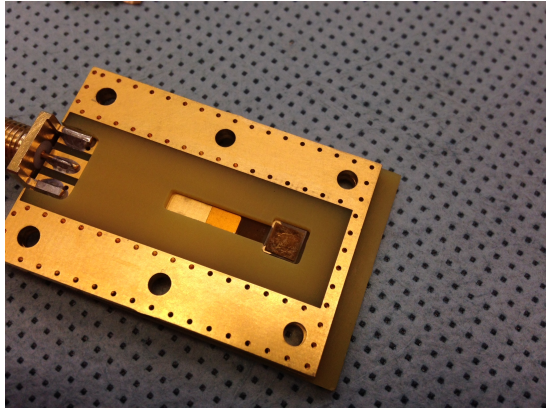
945 for an ROI smaller than the sensitive region of the diamond.

### 946 3.1.5 Room temperature $\alpha$ -TCT setup

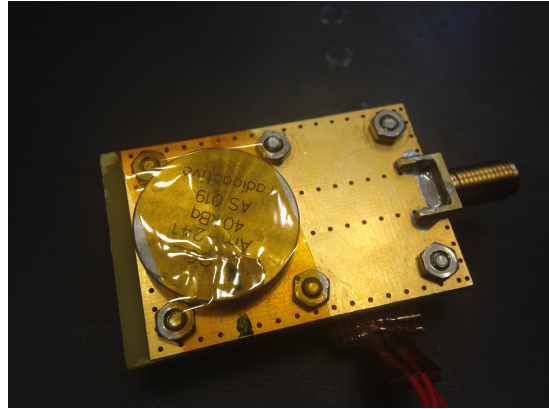
947 This TCT study is a follow-up of an extensive diamond TCT study at cryogenic temperatures [29].  
948 The room-temperature TCT measurements have been carried out in the laboratory. The setup  
949 consists of a diamond sensor embedded in a PCB carrier, a current amplifier and an oscilloscope.  
950 To measure  $\alpha$  particles, their energy loss during their trajectory has to be minimised. Therefore  
951 the diamond is placed inside a vacuum chamber. The chamber is a steel tube with a diameter of  
952 5 cm. On one side it is connected to a vacuum pump via a steel hose. A feedthrough with an  
953 SMA connector is placed on the other side. A CIVIDEC C2 current amplifier is connected directly  
954 onto the feedthrough. The amplified output is connected to the oscilloscope via an SMA cable.  
955 An  $^{241}\text{Am}$  source with a diameter of 2 cm and a height of 0.5 cm is fixed onto the sensor carrier  
956 (figure 3.4a, figure 3.4b). Then the carrier is inserted in the chamber and fixed in place using an  
957 air-tight clamp. The pump can then be switched on. It is capable of providing the inside pressure  
958 as low as  $10^{-4}$  mbar after approximately one hour of operation.

### 3.1. MEASUREMENT SETUP

---



(a) PCB carrier with an embedded diamond sample.



(b) Radioactive source over the carrier.

Figure 3.4: Positioning of the  $\alpha$ -source on top of the sensor carrier.

#### 3.1.6 Cryogenic $\alpha$ -TCT setup

The experiment at cryogenic temperatures has been carried out at the Central Cryogenic Laboratory at CERN. The room-temperature TCT setup has to be modified to allow for measurements at temperatures as low as 4 K. It consists of three parts:

1. a cryostat – a thermally insulated cylinder containing liquid helium,
2. an inlet – an air-tight mechanical tube with valves and feedthroughs at the top that is lowered in the liquid helium and
3. the diamond sample embedded in a PCB carrier with a fitted temperature sensor, a heater and cables leading to the feedthroughs.

The setup is described in detail in [29].

When the diamond sample is placed in the PCB carrier and the  $^{241}\text{Am}$  source is in place, the inlet is sealed and lowered in the empty cryostat. Then the inside volume of the inlet is evacuated down to  $10^{-5}$  mbar while the liquid helium is flowing into the cryostat. To improve the thermal contact between the diamond and the coolant, a small amount of helium gas is added inside the evacuated inlet, setting the vacuum to around  $10^{-3}$  mbar. This value changes with time, because the gas condenses on the walls of the inlet, reducing the number of floating particles. For this reason the helium gas has to be added on an irregular basis. Every addition causes a significant undershoot of the sample temperature, which has to be corrected for using a heater placed on the back of the PCB carrier. Also, the added gas deteriorates the vacuum inside the inlet. Furthermore, at approximately 60 K the helium gas has to be evacuated from the inlet to avoid a potential explosion due to the expansion of the gas with temperature.

When the sample is cooled to 4 K, the minimum temperature achievable by means of liquid helium without over-pressurising it, the measurements can begin. A temperature sensor placed on the back of the PCB carrier is used to measure the temperature of the sample. After every temperature data point, the current through the heater is increased, heating up the sample. The initial temperature time constant of the order of tenths of seconds at low temperatures increases with temperature. Even more so when helium is evacuated from the inlet at 60 K, removing the thermal bridge between the wall of the inlet and the diamond sample. At the room temperature (RT), the time constant is already of the order of minutes.

### 3.2 Charged particle pulses and spectra

In previous chapter the ionisation profiles for different types of radiation were discussed.  $\beta$  radiation induces a triangular electric pulse whereas  $\alpha$  radiation induces a rectangular one. However, their amplitude, width and rise/fall time depend heavily on the type of interaction with the diamond, the purity of the diamond and the bandwidth of the amplifier and the oscilloscope. This section shows the signal pulses of  $\alpha$ ,  $\beta$  and  $\gamma$  radiation with their respective energy distributions for the case of a diamond detector.

Figure 3.5 shows a set of pulses and an averaged waveform for 5.5 MeV  $\alpha$ , 2.3 MeV  $\beta$  and 1.3 MeV  $\gamma$  radiation using an  $^{241}\text{Am}$ , a  $^{90}\text{Sr}$  and a  $^{60}\text{Co}$  source, respectively. The particles are measured with the non-irradiated sCVD diamond S37.  $\alpha$  particles always produce the same signal pulse with a noise RMS of 2.7 mV. The averaging suppresses the noise while retaining most the information. It does, however, smear the rising and falling edge, increasing the rising and falling time.  $\text{Theta}_r$  is now of the order of 0.5 ns. Both  $\beta$  and  $\gamma$  pulses look similar - triangular and with a wide range of amplitudes. Here the pulse count is low, so the pulses with a high amplitude are not recorded. A trigger would need to be set very high to “catch” them with the oscilloscope.

### 3.2. CHARGED PARTICLE PULSES AND SPECTRA

---

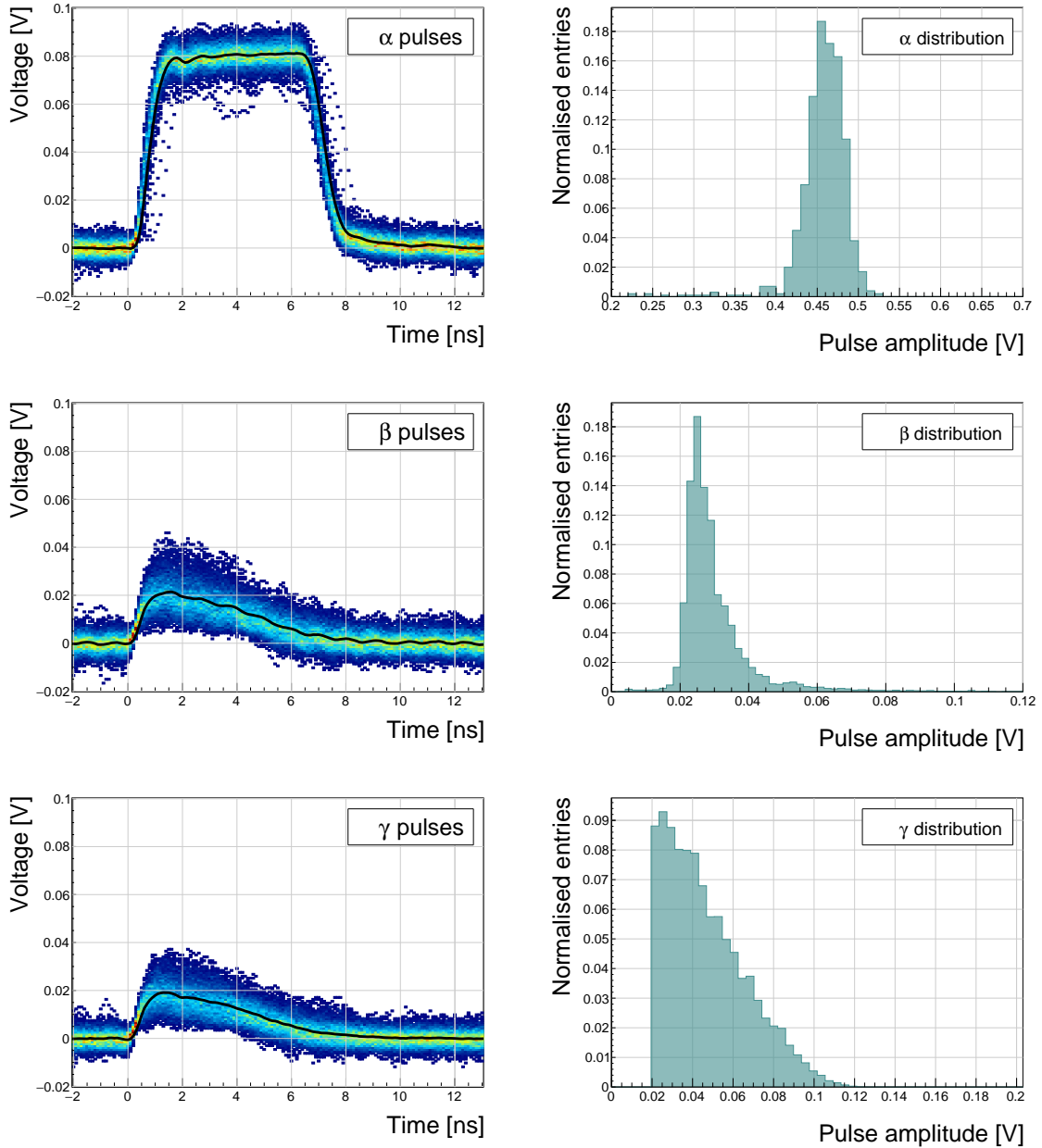


Figure 3.5: Superimposed and averaged pulses (left figures, current amplifier) and distributions of deposited energy (right figures, charge amplifier) for three types of radiation. Note the scale on the x axis of the distributions.

### 3.3 Radiation limitations

This section quantifies the decrease in charge collection efficiency as well as the effects on long-term measurement stability in irradiated sCVD diamonds.

#### 3.3.1 Irradiation study

This subsection contains a study of the effects of 300 MeV pion ( $\pi$ ) irradiation on the charge collection efficiency of sCVD diamond detectors. To carry out this study, two diamond samples were irradiated with 300 MeV pions ( $\pi$ , kinetic energy 191.31 MeV). The irradiation campaign took place at the Paul Scherrer Institute (PSI) [55] where the machine provides a flux of  $1.5 \times 10^{14} \pi \text{ cm}^{-2}$  per day. The quoted uncertainty on the measurement of the delivered dose is  $\pm 20\%$ . In addition, a deviation in beam energy can have a significant effect on the damage in the sensor, considering the pion damage curve in figure 2.10 at a  $\pi_{300 \text{ MeV}}$  point ( 191 MeV kinetic energy), which sits on a steep section of the DPA curve. The target fluences for S79 and S52 were  $(1 \pm 0.2) \times 10^{14} \pi \text{ cm}^{-2}$  and  $(3.6 \pm 0.7) \times 10^{14} \pi \text{ cm}^{-2}$ .

A test beam campaign was carried out to observe the charge collection efficiency at different bias voltage settings. The efficiency values acquired are used to determine the effective drop in efficiency as a function of fluence. This is to test if the collected charge  $Q$  is inversely proportional to the fluence  $\Phi$ . A procedure defined by a collaboration researching diamond behaviour RD42 has been applied to the measured values to extract the damage factor described in 2.5.

The following subsection contains measurements and results of a long-term stability study using  $\alpha$  and  $\beta$  particles. In particular, the charge collection efficiency with  $\beta$  and  $\alpha$  radiation as a function of time is measured. To investigate this effect on the scale of charge carriers, the change of TCT (transient current technique) pulses with time is observed. Finally, a procedure that improves the pulse shape and with it the charge collection is proposed.

##### 3.3.1.1 300 MeV $\pi$ radiation damage factor

Three diamonds – non-irradiated S37 and irradiated S52 and S79 – were tested in a  $\pi_{120 \text{ GeV}}$  test beam in the SPS North Experimental Area at CERN [56] before and after irradiation. The goal was to estimate the charge collection efficiency and charge collection distance as a function of fluence. The samples were primed prior to data taking using a  ${}^{90}\text{Sr}$  radioactive source. The data were then taken at a range of bias voltages ranging from 30 V to 900 V, yielding between  $0.06 \text{ V}/\mu\text{m}$  and  $1.8 \text{ V}/\mu\text{m}$  electrical field in the bulk. Every data point contained approximately  $5 \times 10^4$  measured particles. The charge deposited by the particles was measured using a CIVIDEC Cx charge preamplifier.

The integrated amplitude spectrum is a Landau distribution. Its most probable value (MPV) is used to calculate the most probable collected charge  $Q_i$ :

$$Q_i [\text{e}^-] = \frac{1}{1.6 \times 10^{-19}} Q_i [\text{C}] = 6'241 \cdot Q_i [\text{fC}] = 6'241 \cdot \frac{\text{MPV} [\text{mV}]}{A [\frac{\text{mV}}{\text{fC}}]}, \quad (3.6)$$

where  $A = 9.3 \text{ mV/fC}$  is the preamplifier gain factor and  $1 \text{ e}^- = 1.6 \times 10^{-19} \text{ C}$ .

The CCD for the three measured samples at a bias voltages ranging from  $0.2\text{--}1.6 \text{ V } \mu\text{m}^{-1}$  calculated using equation 2.18 is shown in figure 3.6. S37 exhibits a full collection distance already at  $0.4 \text{ V } \mu\text{m}^{-1}$  whereas the irradiated samples have a more gentle increase of CCD with increasing bias voltage. It is evident that at  $1 \text{ V } \mu\text{m}^{-1}$  the maximum CCD has not been reached in the case of S79 and S52. Nevertheless, to compare the measured data point with those provided by RD42, the CCD at  $1 \text{ V } \mu\text{m}^{-1}$  has to be taken.

### 3.3. RADIATION LIMITATIONS

---

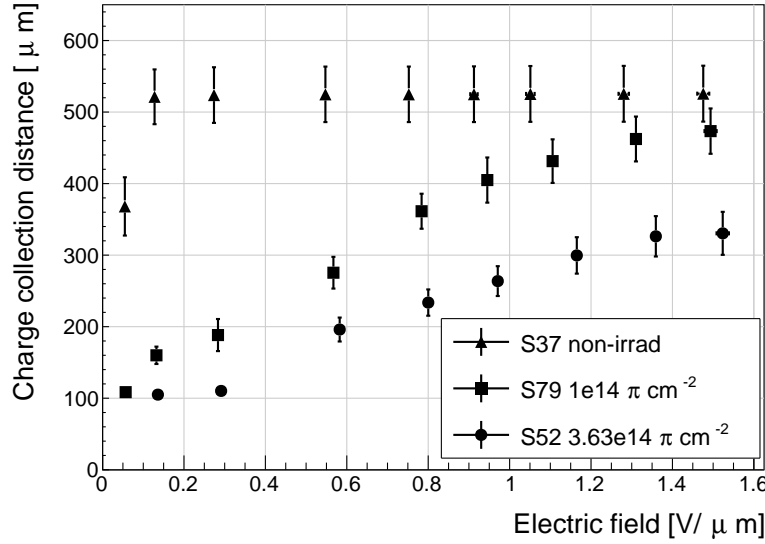


Figure 3.6: The figure shows the CCD for S37, S79 and S52 at a range of bias voltage settings.

The data points with the maximum CCD obtained in the test beam measurements are plotted as a function of fluence in figure 3.7. Equation 2.20 is fitted to the data points and a damage factor  $k_\lambda = (4.4 \pm 1.2) \times 10^{-18} \mu\text{m}^{-1} \text{cm}^2$  is obtained. The value is for a factor of two higher than the damage factor obtained by RD42. This could be due to an insufficient priming time ahead of the measurement. Figure 3.8 shows the effect of priming. The samples were only exposed to the radioactive source for a short time and might not have achieved the maximum charge collection. In addition, the diamond samples have not been polished and re-metallised after irradiation, as is the case for the RD42. A study of effects of re-metallisation on the charge collection has been done in [57] and supports this theory. Furthermore, with only two samples measured, the statistical uncertainty is high. For a better fit another measurement point at a higher fluence would need to be added. Nevertheless, it can be concluded that the 300 MeV pions damage the diamond bulk significantly more than the 24 GeV protons, as shown in chapter ??.

Another diamond irradiation study has been carried out using the Beam Conditions Monitor (BCM) at the CMS experiment [36]. The BCM's diamond sensors have been exposed to radiation from beam collisions with a wide spectrum of energies and particle types. The damage factors measured are an average of  $3.5 \times 10^{-17} \mu\text{m}^{-1} \text{cm}^2$  and  $9.2 \times 10^{-16} \mu\text{m}^{-1} \text{cm}^2$  for pCVD and sCVD diamonds, which is for a factor of 58 and 1500 higher than the RD42. These low charge collection efficiencies, however, are purported to be convoluted with other effects, such as polarisation, which will be discussed later in the chapter.

#### 3.3.2 Long-term measurement stability

An important requirement for particle detectors is a stable performance over long periods of time. For instance, the charge collection for a defined radiation type and quantity must not change over time or has to change in a predicted way. The stability of diamond detectors depends on many factors, e.g. material purity, polishing process, electrode material, irradiation damage etc. The aim is to study the behaviour of diamond under controlled conditions, with the goal to understand its

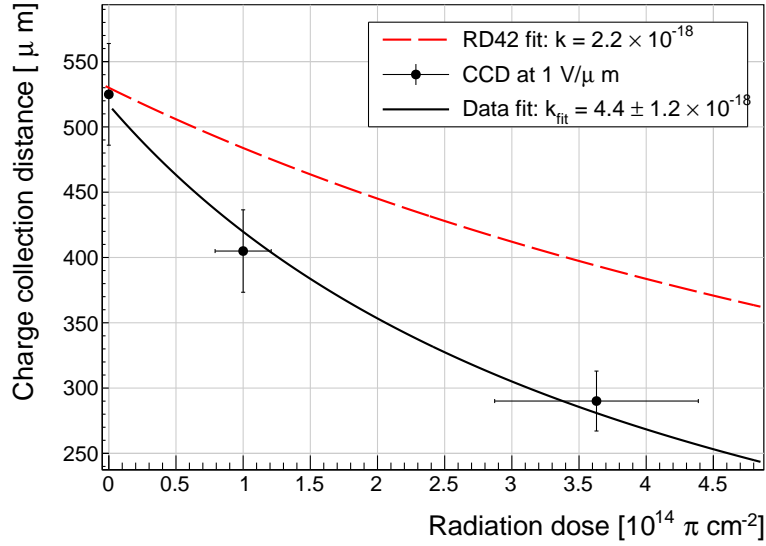


Figure 3.7: The charge collection distance at 1 V/ $\mu\text{m}$  bias voltage for the three diamond samples is plotted as a function of fluence. It is compared to the RD42 data for pion irradiation. The data points are about 15–25 % lower than expected from the RD42 data [42].

1068 limitations. One of these limitations is the fluence as it can affect the long-term stability of the  
1069 sensor during operation.

1070 The three diamond samples (S37, S79 and S52) have been exposed to two different types of  
1071 ionising radiation for a longer period to see if their behaviour changes over time. Two parameters  
1072 have been observed in particular:

- 1073 1. Charge collection of  $\beta$  particles and  
1074 2. Charge collection and ionisation profile of  $\alpha$  particles.

1075 **3.3.2.1  $\beta$  long-term stability**

1076 The diamond samples have undergone a long-term stability test at room temperature using  $\beta$  radia-  
1077 tion. This has been done using a  ${}^{90}\text{Sr}$  source emitting  $\sim 2.28$  MeV electrons at a rate of approximately  
1078  $10^4 \text{ e}^- \text{ cm}^{-2}$ . To simulate the initial conditions in HEP experiments, the sensors must not be primed  
1079 before starting the measurements. The measurement setup consists of a diamond sample (S37, S52  
1080 or S79) with the CIVIDEC Cx spectroscopic amplifier, a silicon diode with a CIVIDEC C6 amplifier  
1081 for triggering and a  ${}^{90}\text{Sr}$  source on top. A particle emitted by the source traverses the sensor bulk  
1082 and hits the silicon diode, triggering the analogue signal readout. The source is left on the top for the  
1083 course of the experiment. The measurements, however, are taken at discrete times. For every data  
1084 point, approximately  $10^4$  triggers have to be recorded. The offline analysis of the recorded signal  
1085 pulse amplitudes yields a Landau distribution for every data point. The current charge collection  
1086 relative to the initial charge collection for every sample is plotted as a function of the received  $\beta$   
1087 dose in figure 3.8. It shows that, for the irradiated samples, the charge collection efficiency improves  
1088 when the diamond sensor is primed with a  $\beta$  source. The effect is negligible for the non-irradiated  
1089 high-quality S37. Both relative increases are significant – 22 % for S79 and 55 % for S52. At a fluence  
1090 of approximately  $4 \times 10^6$  particles the charge collection is stabilised. At that point S79 achieves close  
1091 to a full efficiency (in absolute values – not shown) whereas S52 reaches approximately 50 %.

### 3.3. RADIATION LIMITATIONS

---

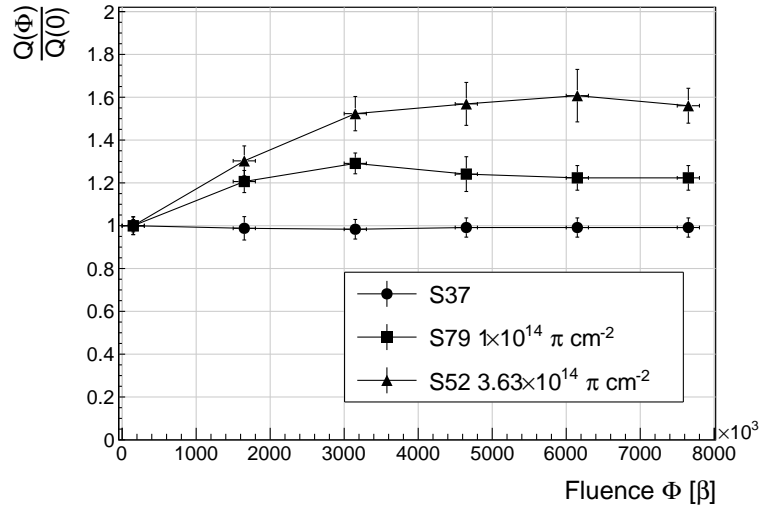


Figure 3.8: Relative increase of charge collection over time due to priming with the  $^{90}\text{Sr}$  radioactive source. The charge collection for the non-irradiated S37 stays constant. The bias voltage for this measurement is 1 V/ $\mu\text{m}$ .

To sum up, diamond provides a stable measurement of the  $\beta$  radiation detection after reaching a stable state. Even if damaged by radiation, it reaches a stable charge collection at a fluence of  $\sim 4 \times 10^6$  MIPs. Its efficiency decreases with a high fluence. However, the decrease can be accounted for if the damage factor and the rate and energy of the particles are known.  $\gamma$  radiation has a similar impact on the diamond as the  $\beta$ . The incident photons, if they interact with the diamond, prime the bulk, increasing the charge collection efficiency. The difference, however, is that the interaction probability (cross-section) is lower for gammas [58, 59].

#### 3.3.2.2 $\alpha$ long-term stability

This part discusses the stability of irradiated diamond sensors during  $\alpha$  measurements. An  $^{241}\text{Am}$  source has been used, emitting  $\alpha$  particles with a mean energy of 5.5 MeV with an average rate of  $7 \text{ s}^{-1}$ .

To test the stability of the diamond during  $\alpha$  measurements, the samples have been biased at +500 V and exposed to up to  $8 \times 10^3$   $\alpha$  hits while measuring their charge collection efficiency using the CIVIDEC Cx spectroscopic amplifier. The charge collected at every measurement point  $Q(\Phi)$  is compared to collected charge of the first measurement  $Q(0)$ . The resulting ratio  $\frac{Q(\Phi)}{Q(0)}$  for all samples is shown in figure 3.9. Each measurement point is an average of 30 consecutive  $\alpha$  hits. The observations are the following:

- $Q(\Phi)$  for the non-irradiated S37 is stable as compared to  $Q(0)$  over the course of the measurement.
- The initial efficiency of the irradiated S52 and S79 starts decreasing already at a low  $\alpha$  count.
- The charge collection efficiency of the unprimed irradiated samples drops much faster than after priming.

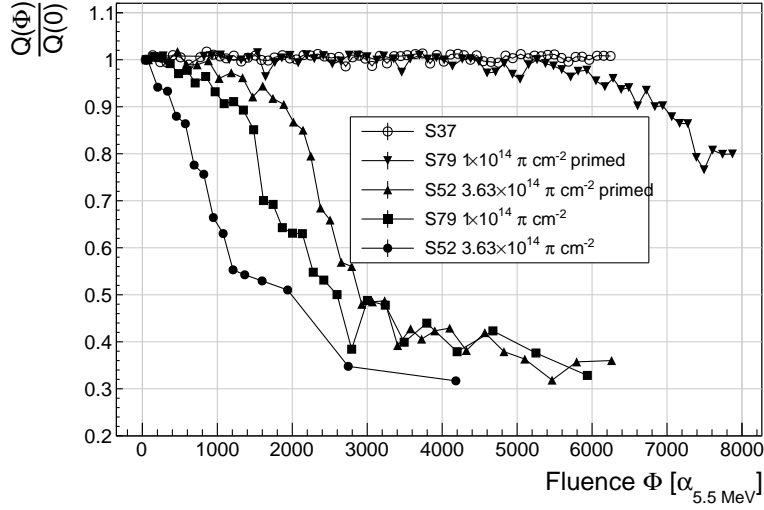


Figure 3.9: A relative drop in charge collection efficiency as a function of the received  $\alpha$  dose for non-irradiated and irradiated diamond samples.

1114 - The particle count rate decreases with decreased efficiency, which is clearly seen in the un-  
1115 primed S52 data where the data points at a low efficiency are much further apart.

1116 The absolute values are not shown here because only the relative drop is of interest in the scope of  
1117 the long-term stability tests.

1118 To investigate this sudden drop in efficiency, the current pulse shapes using a CIVIDEC C2  
1119 current amplifier have to be observed, as shown in figure 3.10. The shape of the pulse holds more  
1120 information about the charge carrier properties in the sensor than solely the value of the integrated  
1121 charge. This time only the primed S79 sample has been tested. Both the hole and the electron  
1122 collection are observed to determine whether they behave differently or not.

1123 The first observation in the raw acquired data in figures 3.10 is that the initially stable pulses  
1124 start deteriorating; several different shapes start appearing gradually, some still very similar to those  
1125 from the beginning while the others with almost zero amplitude.

1126 A more dedicated analysis of the first observation has been carried out as follows: at the beginning  
1127 of the test when the diamond is still operating stably, 60 pulses are recorded. An average pulse is  
1128 calculated. This is a reference pulse for the subsequent measurement points. Then an RMS of the  
1129 individual pulses  $\sigma_n$  with respect to the reference pulse is calculated and the resulting RMS values  
1130 are summed together into  $\sigma(0)$ :

$$\sigma(0) = \sum_{n=1}^{60} \sigma_n. \quad (3.7)$$

1131 All the subsequent data points also consist of a set of 60 pulses. At every data point the  
1132 summation of the RMS values of the individual pulses with respect to the initial averaged pulse  $\sigma$  is  
1133 calculated according to equation 3.7. The ratio between the initial  $\sigma(0)$  and discrete values  $\sigma$  gives  
1134 a measure of the change of the pulse shape with respect to the reference pulse at the start of the  
1135 measurement. Therefore the initial value is 1 and it decreases if the RMS values of subsequent data  
1136 points are higher. Figure 3.11 shows the ratio  $\frac{\sigma(\Phi)}{\sigma(0)}$ . From the data obtained it can be concluded that  
1137 the initial pulse shape quickly starts deteriorating. In fact, the deterioration of the shape follows

### 3.3. RADIATION LIMITATIONS

---

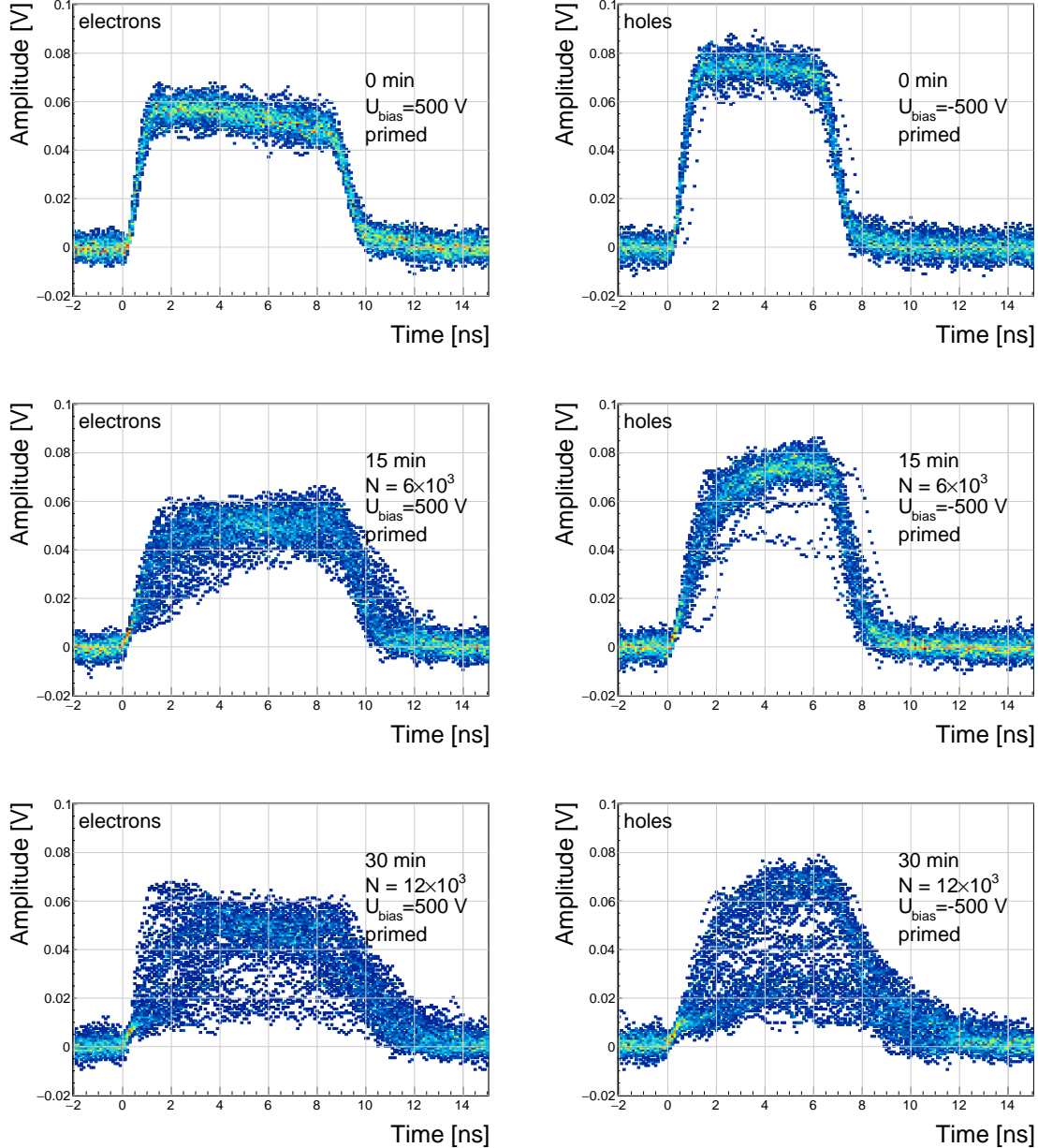


Figure 3.10: The signal of the irradiated and primed S79 deteriorates with time for both polarities. Every plot contains 60 superimposed pulses.

1138 an approximate exponential decay function, which can be fitted to the data. The resulting decay  
 1139 constants for electrons and holes are  $\tau_e = (4400 \pm 150) \alpha^{-1}$  and  $\tau_h = (3300 \pm 140) \alpha^{-1}$ . The electrons  
 1140 retain the initial shape for longer. The deteriorated shapes also seem to be for a factor of 2 better  
 1141 than those of the holes.

1142 **Discussion** One hypothesis is that this behaviour is caused by space-charge build-up. Charge  
 1143 carriers get stopped in the charge traps in the bulk for a long time, building up regions of space-  
 1144 charge. The built up space-charge affects the electric field. The field in turn affects the speed of the  
 1145 drifting charge carriers. Since the movement of the carriers is inducing the electric current, the field

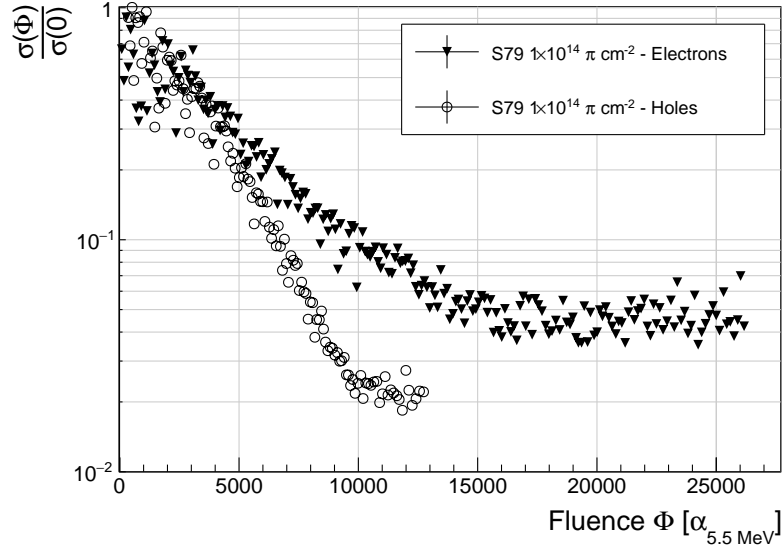


Figure 3.11: Deterioration of the pulse shapes with time.

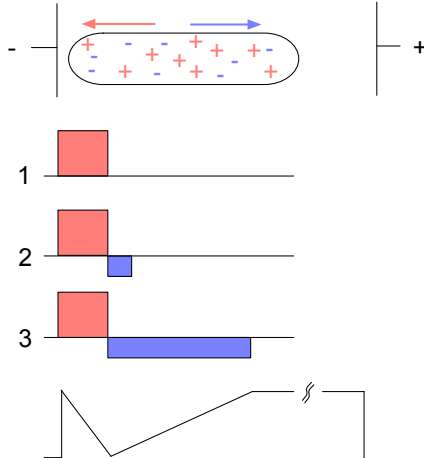


Figure 3.12: Space-charge build-up at the electrode.

1146 gradient can be observed in the current signal. The fact that the signal shapes vary significantly  
 1147 might be due to a very non-uniform electric field. Figure 3.12 shows how the space-charge might  
 1148 be built up at the entry point of the  $\alpha$  particle. The assumption is that the first 3  $\mu\text{m}$  of diamond  
 1149 surface are significantly more damaged than the rest of the material. Therefore the probability that  
 1150 charge carriers would get trapped at the edge of the sensor is higher. If the sensor is biased as shown  
 1151 in the figure, the positive charge cloud drifts towards the adjacent electrode while the negative cloud  
 1152 drifts through the sensor to the opposite one. Therefore most of the trapped carriers at the adjacent  
 1153 electrode are positive, forming a strong positive space-charge in the first few  $\mu\text{m}$  of the sensor (1). The  
 1154 negative carriers created by subsequent  $\alpha$  particles are attracted by the positive space charge and  
 1155 get trapped close to the positive space-charge (2). This negative space-charge region is gradually

### 3.3. RADIATION LIMITATIONS

---

stretched inwards (3). Together the two regions form a barrier which counteracts the externally applied electrical field. Such a distortion of the field prevents the charge carriers from drifting freely within the space-charge region. Only those negative carriers that diffuse through this barrier can start drifting towards the positive electrode. Others either recombine or are trapped, contributing to the build-up of the barrier.

This hypothesis explains the gradual loss of collected charge in figure 3.9 and the pulses with a slow rising edge in figures 3.10. However, it cannot explain the electron pulses with a negative slope. Further reading regarding the space-charge build-up is available in [60, 61, 62].

**Restoring the pulse shapes** Finally, an effort has been made to find a way for the pulse shapes to return to their initial state. Five methods are listed:

1. No source, with bias voltage,
2. No source, without bias voltage,
3. Priming with  $\gamma$  at a rate of  $400 \text{ s}^{-1}\text{cm}^{-1}$  without bias voltage,
4. Priming with  $\beta$  at a rate of  $1'000 \text{ s}^{-1}\text{cm}^{-1}$  with bias voltage and
5. Priming with  $\beta$  at a rate of  $1'000 \text{ s}^{-1}\text{cm}^{-1}$  without bias voltage.

Before starting each method, the diamond sample S79 is first primed using a  $^{90}\text{Sr}$  source for approximately one hour. Then the bias voltage is switched on and an  $^{241}\text{Am}$  source is put on top. The pulses produced by the incident  $\alpha$  particles have a proper rectangular pulse at the beginning, but then start changing – first gradually and later increasingly more in an erratic way, as described in the text above. After approximately 30 minutes, one of the methods is tested. When a “healing” procedure is started, a set of 60 pulses is taken at irregular points of time to observe the change in the pulse shape and to assess the quality of the “healing” procedure. Then the bias voltage is switched off and the sample is primed again to reset its state before starting with the next run.

The results depicted in figure 3.13 show that the methods (3) and (5) improve the shape, method (2) helps slowly, (1) does not show any change with time and (4) at first improves, but then significantly degrades the shape. The effect observed in method (4) has already been described in [63]. The “healing” process therefore depends on the rate of radiation, the bias voltage and the time of exposure. The ionising radiation creates free charges, which quickly recombine close to the place of generation. It is likely that they also release the charges trapped during the measurement, reducing the overall effect of the space-charge. The traps get filled with both flavours of carriers, thus they are neutralised. The pulse shape gradually returns to its initial state.

Procedure	Source	Type of radiation	Bias voltage	Effectiveness
1	/	/	ON	no
2	/	/	/	slow
3	$^{60}\text{Co}$	$\gamma$	/	YES
4	$^{90}\text{Sr}$	$\beta$	ON	no
5	$^{90}\text{Sr}$	$\beta$	/	YES

Table 3.2: Effectiveness of healing procedures.

**Summary** The shape of the pulses caused by  $\alpha$  radiation changes with time for irradiated samples. The shape of the pulses gets distorted. The charge collection decreases and its spread increases. The signal shapes are probably affected by a non-uniform electric field, which is caused by the build-up of space charge. The signal degradation happens even faster for non-primed diamonds. To “heal” the diamond – to bring the pulse shapes back to their initial shape – the sample must be primed

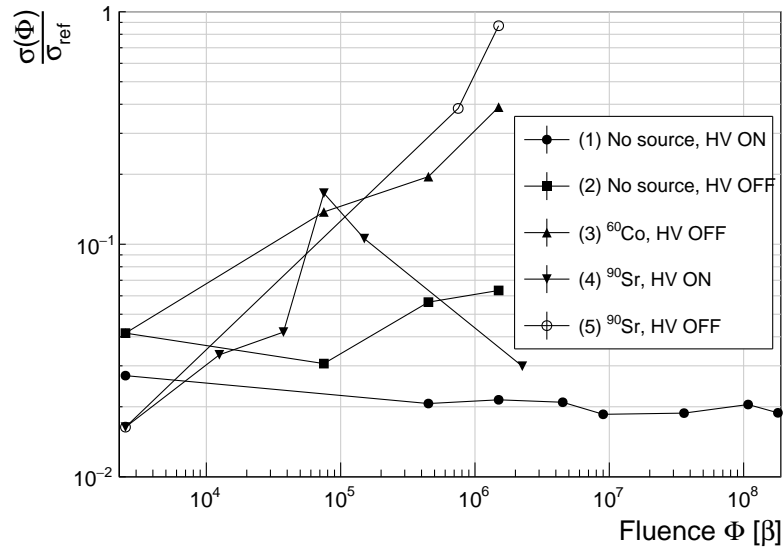


Figure 3.13: Comparison of the five procedures for the “healing” process for an irradiated diamond that had been exposed to  $\alpha$  radiation with a rate of  $10^1 \text{ s}^{-1}$ , with the bias voltage switched on, for at least 30 minutes.

<sub>1194</sub> using a  $\beta$  or a  $\gamma$  source for several minutes without bias voltage. Switching to the inverse polarity  
<sub>1195</sub> for a few seconds helps a bit, but in a long run distorts the signal, preventing it from returning to  
<sub>1196</sub> the initial shape.

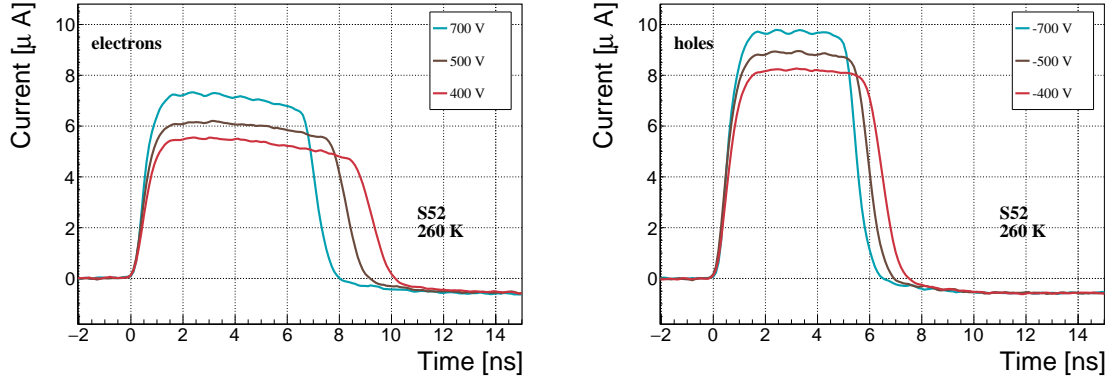


Figure 3.14: Varied bias voltage at a fixed temperature of 260 K.

## 3.4 Temperature limitations

A test has been carried out to evaluate the effect of temperature on the output signal of the diamond sensors. A cryostat filled with liquid helium is used to cool down the sensor during the measurement process. The current signal response to  $\alpha$ -particles is measured at 18 temperature points between 4 K and 295 K. At every temperature point a set of 300 pulses is recorded at various bias voltages. The resulting data show that the charge collection is stable from RT down to 150 K where it starts decreasing. It stabilises again at about one third of the initial value at 75 K. This behaviour was first measured and discussed by H. Jansen [29].

### 3.4.1 Temperature-variant $\alpha$ -TCT before irradiation

Three sCVD diamond samples have been tested at a range of temperatures using the  $\alpha$ -TCT technique. At each temperature point, the bias voltage is set to several positive and negative values. A set of 300 pulses is recorded at every data point and averaged offline. The resulting averaged pulses of sample S37 at the 260 K temperature point and a bias voltage of  $\pm 700$  V,  $\pm 500$  V and  $\pm 400$  V are shown in figure 3.14. The pulses induced by holes as charge carriers are shorter than those induced by electrons, which means that holes travel faster in diamond. The area of the pulse, however, is the same for both polarities, which corresponds to the fact that the same amount of charges is drifting in both cases.

Figure 3.15 shows pulses at a bias voltage set to  $\pm 500$  V across the range of temperatures between 4 K and 295 K. Several conclusions can be drawn by observing their shape. First, the pulse shapes change with decreasing temperature. The pulse time gets shorter and higher, hinting at the faster carrier drift velocity  $v_{\text{drift}}$ . Second, between 150 K and 75 K there is a significant change in shape – the time constant of the rising edge increases significantly and the pulse area decreases [29]. From 75 K down to 4 K there is no significant change. Last, the top of the pulse at the S52 is not flat, which means that a portion of the drifting charge is lost along the way. This is due to the built up space-charge, likely by means of crystal defects or impurities.

### 3.4.2 Temperature-variant $\alpha$ -TCT after irradiation

The irradiated S79 and S52 have been re-tested in the cryostat after irradiation. The aim is to observe how their pulse shapes change with decreasing temperature, in particular the decaying top

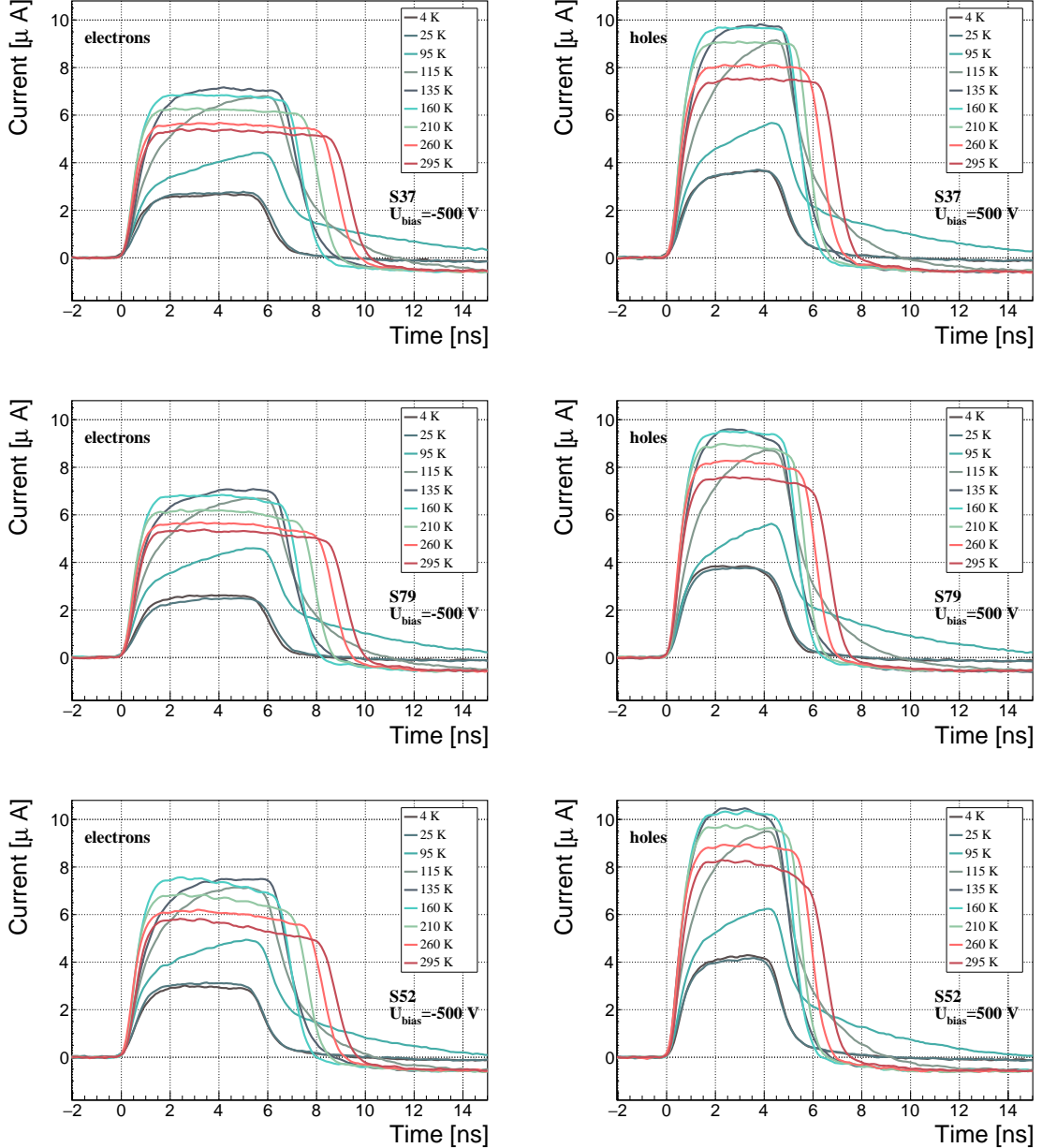


Figure 3.15: Several data points between 4 K and 295 K at a bias voltage of  $\pm 500$  V. The tilted top of the pulse on the bottom left figure is due to built-up space charge.

### 3.4. TEMPERATURE LIMITATIONS

---

of the pulses, as shown in figure 3.16. The decay time gives information on trapping of charge carriers while travelling through the diamond bulk. A variation of the decay time constant as a function of temperature might help to reveal the type and depth of the charge traps. To observe these effects, a number of requirements have to be met. First, the diamond samples are intentionally not primed prior to the experiment because priming would improve the pulse shapes and change the decay time constant of the signal. Second, keeping in mind that the pulse shape of irradiated diamonds changes with time, the duration of the measurement of an individual data point has to be short – of the order of 30 seconds. Last, the sequence of the bias voltage settings is important, the reason for which is explained below.

Temporal pulse changes are unavoidable. For instance, one measurement point takes approximately one minute. After the measurement, the bias voltage polarity is swapped for a few seconds to bring the diamond back into its initial state. A few seconds with respect to a minute are not enough, but due to time constraints this cannot be avoided. Therefore when the bias voltage is set to the next value, there is still some residual effect of the previous measurement. Similar to the effects of polarisation, this effect is also decreasing the pulse height. This can be observed in figure 3.16, which shows the resulting pulses of S52 for bias voltages of  $\pm 200$  V,  $\pm 300$  V,  $\pm 400$  V and  $\pm 500$  V at 230 K and 260 K. In this case the measurement sequence is: 230K (200 V, 300 V, 400 V, 500 V, -500 V, -400 V, -300 V), 260 K (-200 V, -300 V, -400 V, -500 V, 500 V, 400 V, 300 V). The changes in pulse shapes for holes at 230 K and 260 K cannot be attributed to the temperature change. Instead, the explanation lies in diamond polarisation. This means that, when exposed to an electric field with  $\alpha$  measurements ongoing, an internal electric field of inverse polarity builds up in the diamond, which effectively reduces the overall electric field. This internal field does not dissipate when the external bias voltage is switched off. The diamond becomes polarised. When switching the polarity of the external bias voltage, the internal and external electric field point in the same direction at the beginning, increasing the overall electric field and with it the pulse height. In figure 3.16 this happens when switching from 500 V (figure 3.16a) to -500 V (figure 3.16b) at 230 K. The built up polarisation contributes to the pulse having a sharp rising edge and a high amplitude. This effect decays during the next two voltage points. There are a handful of ways to avoid this polarisation effect in the data:

1. After every data point invert the bias voltage and leave it to return to a neutral state for the same amount of time,
2. Make a hysteresis of data points, going from minimum negative to maximum positive bias several times,
3. Reduce the measurement time at every bias voltage setting.

Unfortunately, options (1) and (2) are very time consuming and would increase the overall experiment time to over one day. The third option would worsen the resulting averaged pulses. Finally an alternative option has been chosen: alternating the starting bias voltage and the sequence at every temperature point. With this option, a maximum systematic error in analysing the pulse shapes is attained.

Figure 3.17 shows the irradiated S52 and S79 as well as the non-irradiated S37 for comparison, all at a bias voltage of  $\pm 500$  V and at several temperature points between 4 K and 295 K. It is evident that the radiation damage affects the shape of the pulses across all temperatures.

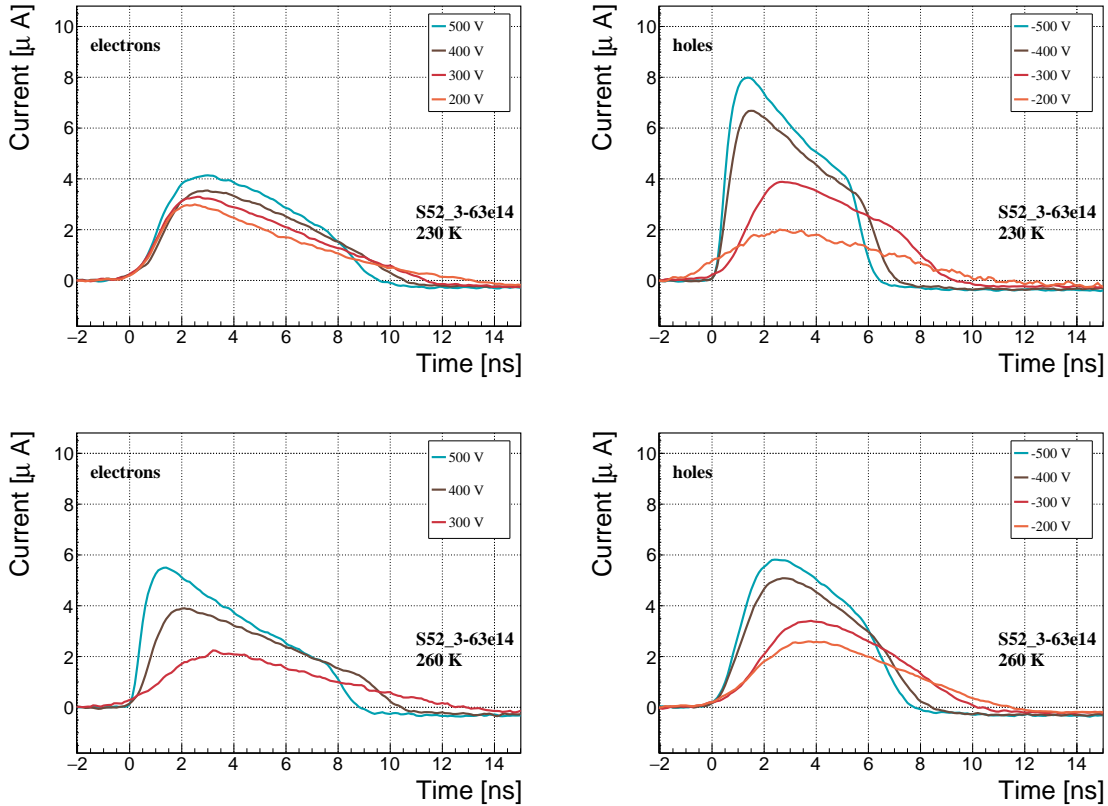


Figure 3.16: Varied bias voltage at a fixed temperature for an irradiated sample.

#### 3.4.2.1 Collected charge as a function of temperature

The collected charge as a function of temperature for electrons and holes is plotted in figures 3.18 and 3.19, respectively. In the framework of this thesis the focus is on the effect in the irradiated devices. The new contribution are the data points for the irradiated samples. The focus is on the temperature range between 4–75 K and 150–295 K whereby the effect of the re-excitation of bound electrons and holes is not prevailing. The values for all samples are fairly stable in the range between 4 K and 75 K and between 150 K and 295 K. However, in the values for the irradiated S52 some excursions can be observed. This is due to the sequence of the measurement steps, which results in a hysteresis effect explained in the preceding text.

The collected charge drops significantly from 150 K down to 75 K. In the non-irradiated samples the values in the lower temperature range are approximately 30 % of those in the high range. For the irradiated samples this difference is lower: 35 % for S79 and 50 % for S52.

An interesting detail in figure 3.18 is that the ratio between the values for non-irradiated samples and their irradiated counterparts at the lower temperature range is different than at the higher range. In other words, the charge loss due to irradiation damage is lower for temperatures between 4 K in 75 K than for temperatures between 150 K and 295 K. The irradiated S52 collects 78 % of the initial charge in the low temperature range, but only 59 % of the initial charge for the high range. The values for S79 for these two temperature ranges are 100 % and 90 %, meaning that the drop in charge collection efficiency after irradiation to  $1 \times 10^{14} \pi \text{ cm}^{-2}$  is negligible for temperatures below 75 K.

### 3.4. TEMPERATURE LIMITATIONS

---

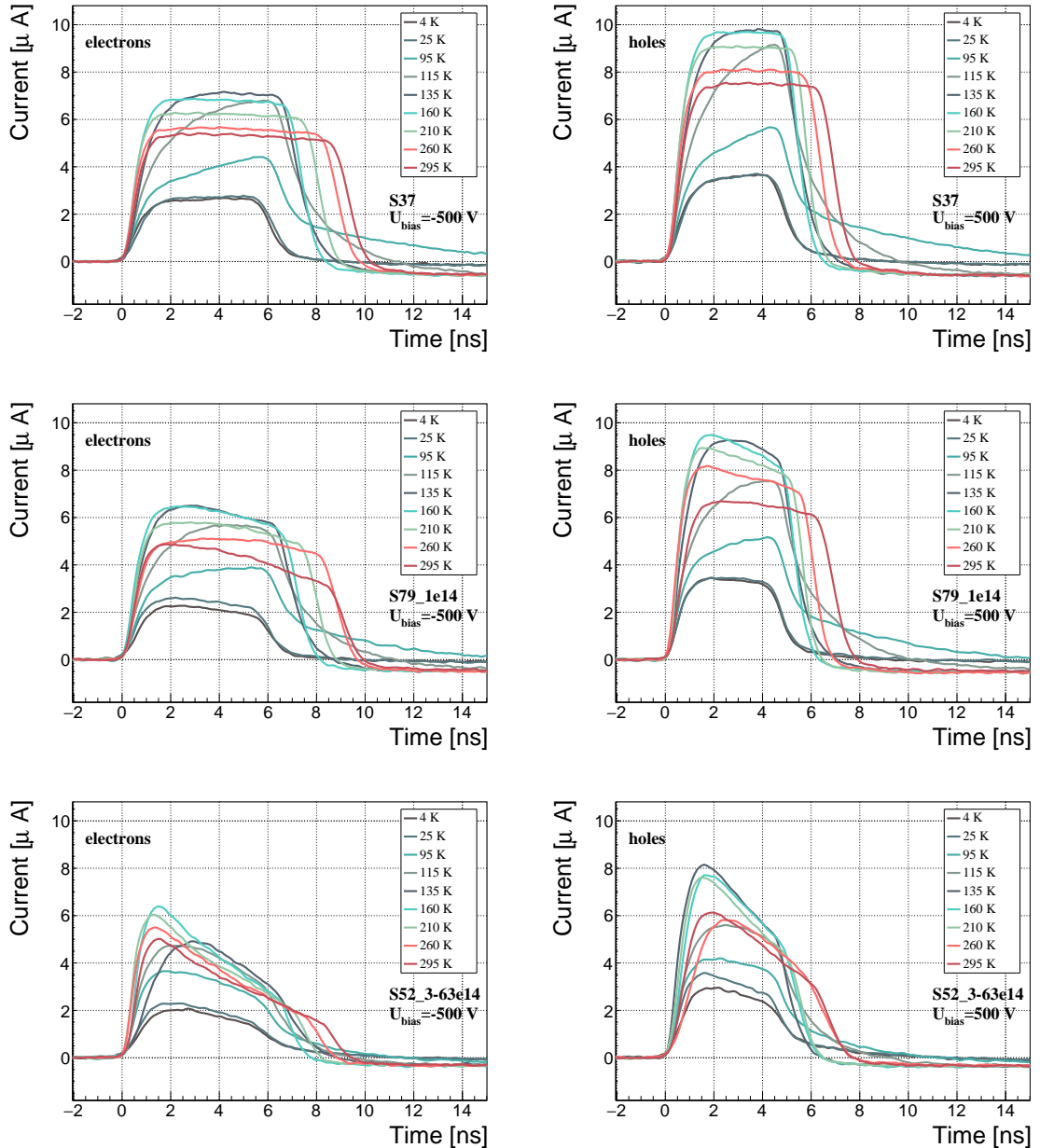


Figure 3.17: After irradiation: several data points between 4 K and 295 K at a bias voltage of  $\pm 500$  V.

1287 **3.4.2.2 Charge trapping**

1288 A decaying exponential function from equation 2.19 has been fitted to the decaying top of the  
 1289 averaged pulses at a bias voltages of  $\pm 400$  V and  $\pm 500$  V across all temperatures excluding the  
 1290 transitional range between 75 K and 150 K. The resulting decay time constants  $\tau$  are effective  
 1291 carrier trapping times. The values differ for individual temperature points due to changing pulse  
 1292 shapes with time by means of “polarisation”. This counts as a systematic error. Therefore the  
 1293 fitted  $\tau$  for  $\pm 400$  V and  $\pm 500$  V are averaged into one value representing the measurement at that  
 1294 temperature point. The time constants should be infinite for an ideal and non-irradiated sample.

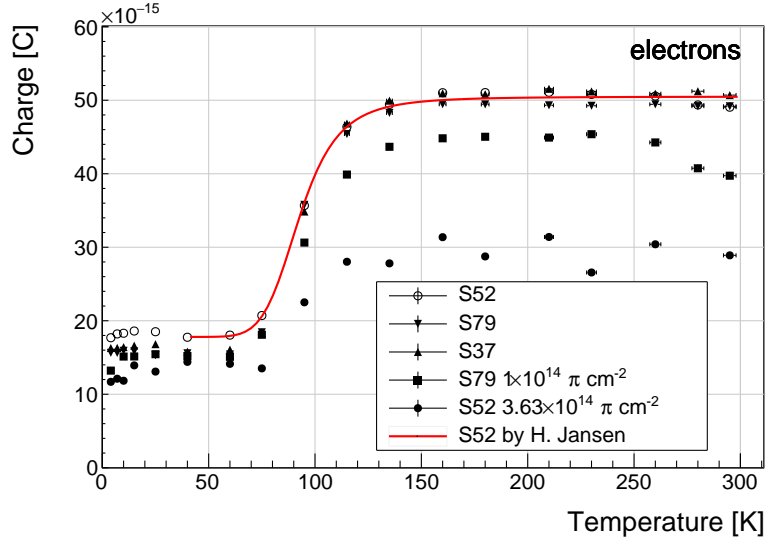


Figure 3.18: Collected charge for electrons as a function of temperature.

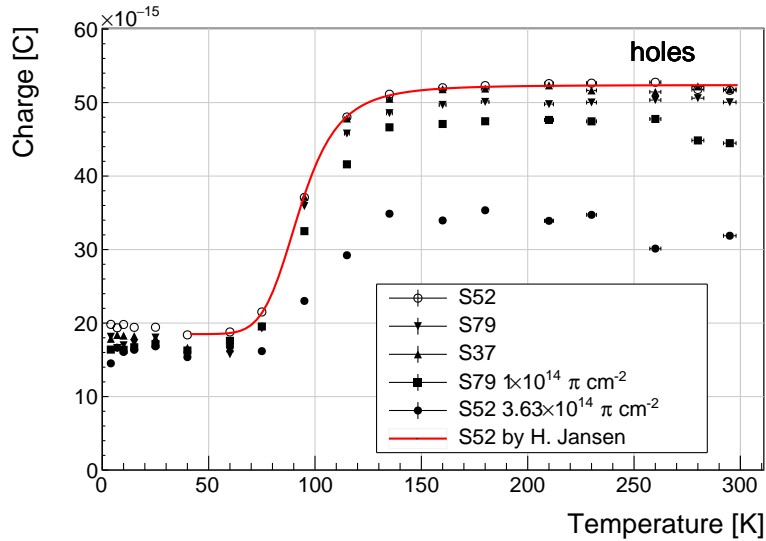


Figure 3.19: Collected charge for holes as a function of temperature.

As seen in figures 3.20a and 3.20b, the fitted values of the irradiated samples are fairly stable across all temperatures. There is a slight increase in the decay time constant of the S52 from  $(6.0 \pm 0.5) \times 10^{-9}$  s above 150 K to  $(8.5 \pm 0.9) \times 10^{-9}$  s below 75 K. This step is however not observable in the S79 data. With only one sample exhibiting this behaviour, the effect is not significant. Judging by the data acquired, the samples would need to be irradiated to doses above  $5 \times 10^{14} \pi \text{ cm}^{-2}$  to quantify this effect in detail. Building on this assumption, the conclusion is that the signal decay time constant for irradiated sCVD diamond is constant across the temperature range between 4 K and 295 K, excluding the transitional range between 75 K and 150 K where it cannot be quantified properly. All things considered, the values can be averaged into one single effective trapping time value for electrons and one for holes for further analysis. The effective trapping time is inversely

### 3.5. CONCLUSION

---

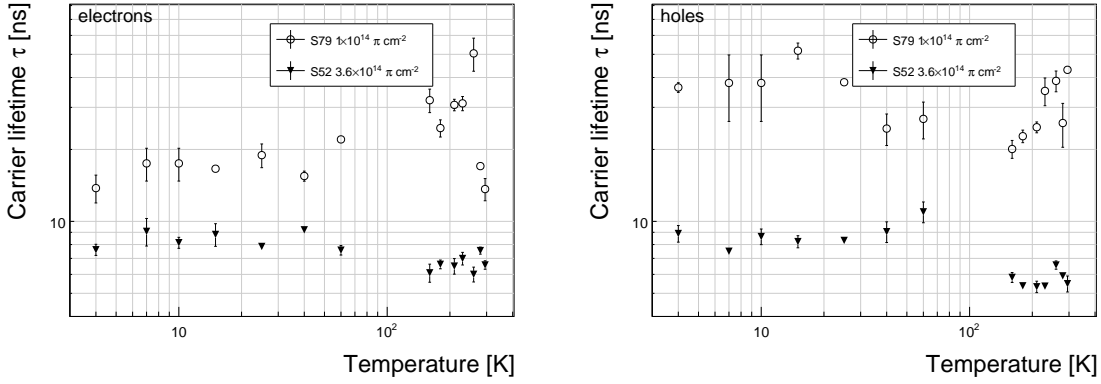


Figure 3.20: Charge carrier lifetime as a function of temperature for electrons and holes at  $\pm 400$  V and  $\pm 500$  V. The data points between 75 K and 150 K are omitted.

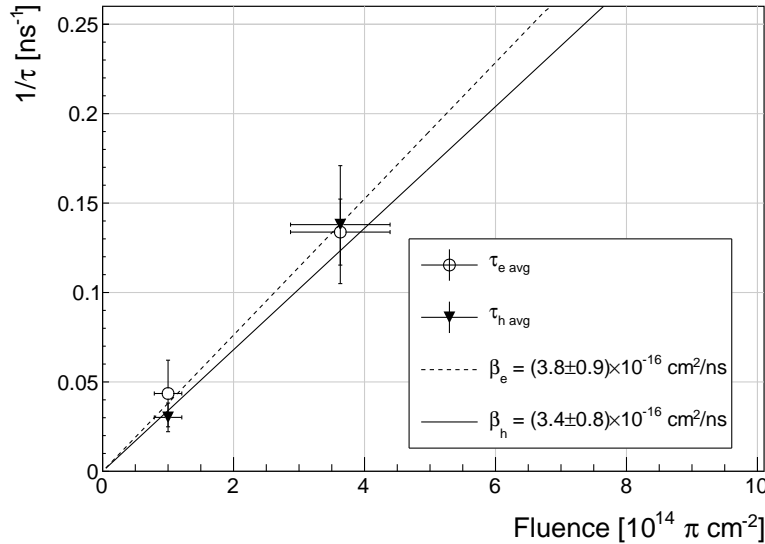


Figure 3.21: This figure shows the inverse charge trapping times averaged over all temperatures and plotted as a function of the  $\pi$  fluence.

1305 proportional to the fluence [64]:

$$\frac{1}{\tau} = \beta \cdot \Phi \quad (3.8)$$

1306 where  $\beta$  is the proportionality factor. A low  $\beta$  value would mean that the trapping centres in the  
1307 sensor are created with a low rate. Figure 3.21 shows the inverse trapping times of the non-primed  
1308 irradiated samples as a function of  $\pi_{300 \text{ MeV}}$  fluence.  $\beta$  is the slope of the fitted linear function. The  
1309 fitted factors are  $\beta_e = (3.8 \pm 0.9) \times 10^{-16} \text{ cm}^2/\text{ns}$  and  $\beta_h = (3.4 \pm 0.8) \times 10^{-16} \text{ cm}^2/\text{ns}$ . Comparing  
1310 to silicon detectors in [64], the value for the sCVD diamond is two times lower.

## 1311 3.5 Conclusion

1312 This chapter gives an overview of the capabilities and limitations of diamond as a particle detector.  
1313 Two effects on diamond are studied – radiation and temperature.

1314 Two sCVD diamond detectors were irradiated with 300 MeV pions. They were tested alongside  
1315 a non-irradiated sample to observe the changes in the ability to detect  $\alpha$ ,  $\beta$  and  $\gamma$  radiation. Their  
1316 charge collection efficiency was measured in a test beam facility. The results were compared to  
1317 the results from the RD42 collaboration and a DPA model. A radiation damage factor  $k_\lambda =$   
1318  $(4.4 \pm 1.2) \times 10^{-18} \mu\text{m}^{-1} \text{cm}^2$  was obtained for  $\pi_{300 \text{ MeV}}$  particles. The data point was not in  
1319 agreement with the data provided by RD42 nor with the model. However, the irradiation process  
1320 and the low number of tested samples hold a relatively high statistical uncertainty. In addition,  
1321 there was no diamond surface treatment done in between the measurements, as is the case in the  
1322 study conducted by RD42. The results obtained in the course of these measurements are going to  
1323 be fed into the existing pool of data in the RD42 collaboration.

1324 The next step was to test the long-term capabilities for  $\alpha$  detection. The shape of the ionisation  
1325 profile was investigated to determine the behaviour of the charge carriers in the irradiated diamond.  
1326 An exponential decay was observed in the pulses of irradiated samples, proving that there are charge  
1327 traps in the bulk that were created during irradiation. Then a long-term stability test was carried  
1328 out. The results show that the irradiated diamond detectors do not provide a stable and reliable  
1329 long-term measurement of  $\alpha$  particles. This might be due to a space-charge build-up in the bulk,  
1330 which changes the electric field, affecting the charge carriers. A procedure to improve the pulse  
1331 shape using  $\beta$  and  $\gamma$  radiation was proposed.

1332 Finally, the diamond sensors were cooled down to temperatures between 4 K and 295 K. Their  
1333 response to  $\alpha$  particles was observed. The results of the non-irradiated and irradiated samples were  
1334 compared. The effect of reduction for the number of drifting charges due to exciton recombination  
1335 was observed in both sets of data. The second set had a superimposed effect of charge trapping  
1336 during the drift, which was represented by an exponential decay in the signal. The decay time  
1337 constant did not change with temperature. Therefore all temperature points for individual samples  
1338 were averaged and the decay time constants were plotted as a function of fluence. Proportionality  
1339 factors for defect production rate  $\beta_e = (3.8 \pm 0.9) \times 10^{-16} \text{ cm}^2/\text{ns}$  and  $\beta_h = (3.4 \pm 0.8) \times 10^{-16} \text{ cm}^2/\text{ns}$   
1340 for non-primed diamonds were extracted.



1341 **Chapter 4**

1342 **Charge monitoring**

1343 ***The ATLAS Diamond Beam Monitor***

1344 **4.1 Introduction**

1345 Particle detectors in high energy physics experiments need to meet very stringent specifications,  
1346 depending on the functionality and their position in the experiment. In particular, the detectors  
1347 in the core of the experiment close to the collision point are subject to high levels of radiation. In  
1348 addition, they need to operate with a high spatial and temporal segmentation to be able to precisely  
1349 measure trajectories of hundreds of particles within nanoseconds. In addition, they need to be highly  
1350 efficient. In terms of the structure, their active sensing material has to be thin so as not to cause  
1351 the particles to scatter or get stopped, which would worsen the measurements. This also means  
1352 that they have to have a low heat dissipation so that the cooling system can be minimised or even  
1353 avoided. Finally, they need to be able to have a stable operation for several years without a required  
1354 intervention, because they are buried deep under tonnes of material and electronics.

1355 The material of choice for the inner detector layers in the HEP experiments is silicon. It can  
1356 withstand high doses of radiation, it is highly efficient (of the order of  $\sim 99.9\%$ ) and relatively low  
1357 cost due to using existing industrial processes for its production. Its downside is that, with increasing  
1358 irradiation levels, it needs to be cooled to increasingly low temperatures to ensure a stable operation.  
1359 This is not the case with diamond. In addition, diamond has a lower radiation damage factor, which  
1360 means it can operate in a radiation-heavy environment for a longer period.

1361 The ATLAS Diamond Beam Monitor (the DBM) [65] is a novel high energy charged particle  
1362 detector. Its function is to measure luminosity (described in section 4.2) and beam background  
1363 (particles not originating in the collision point) in the ATLAS experiment. Given its position in  
1364 a region with a high radiation dose, diamond was chosen as the sensing material. The monitor's  
1365 pCVD diamond sensors are instrumented with pixellated FE-I4 front-end chips. The pCVD diamond  
1366 sensor material was chosen to ensure the durability of the sensors in a radiation-hard environment  
1367 and the size of its active area. The DBM is not the first diamond detector used in HEP, but it is the  
1368 largest pixellated detector installed thus far, as shown in figure 4.1. It was designed as an upgrade to  
1369 the existing luminosity monitor called the Beam Conditions Monitor (BCM) [66] consisting of eight  
1370 diamond pad detectors. The BCM is able to perform precise time-of-flight (ToF) measurements.  
1371 The DBM complements the BCM's features by implementing tracking capability. Its pixelated front-  
1372 end electronics significantly increase the spatial resolution of the system. Furthermore, the DBM is  
1373 able to distinguish particle tracks originating in the collision region from the background hits. This

## 4.2. LUMINOSITY MEASUREMENTS

---

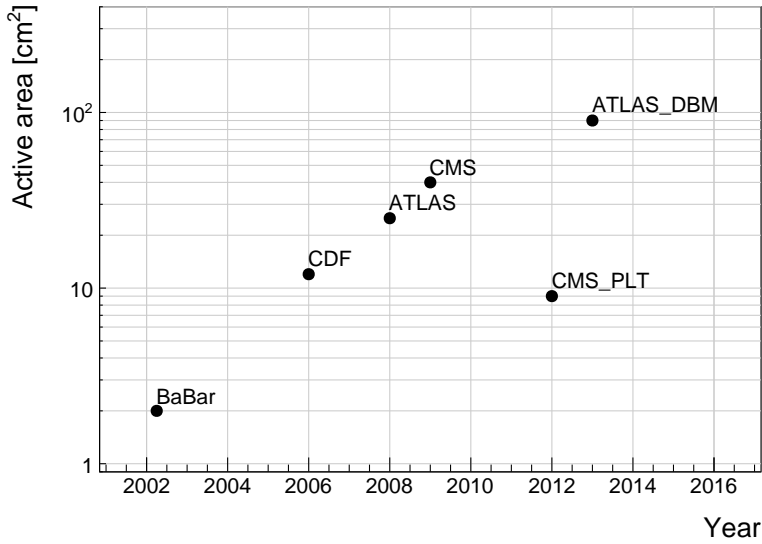


Figure 4.1: Diamond detectors installed in high-energy physics experiments in the last decade, sorted by the active sensor area. The first four detectors from the left are radiation monitors whereas the right two are pixel trackers.

1374 capability is a result of its projective geometry pointing towards the interaction region. This chapter  
 1375 first describes the principles of luminosity measurements. It then explains how the DBM carries out  
 1376 this task. Finally, some results from the commissioning and from the real collisions are presented.

1377 When a particle traverses a sensor plane, a hit is recorded in the corresponding pixel. Thus, a  
 1378 precise spatial and timing information of the hit is extracted. With three or more sensors stacked  
 1379 behind each other, it is also possible to define the particle's trajectory. This is the case with the  
 1380 DBM. Its projective geometry allows the particles to be tracked if they traverse the sensor planes.  
 1381 The DBM relates the luminosity to the number of particle tracks that originate from the collision  
 1382 region of the ATLAS experiment. Particles that hit the DBM from other directions are rejected as  
 1383 background radiation.

## 1384 4.2 Luminosity measurements

1385 Luminosity is one of the most important parameters of a particle collider. It is a measurement of the  
 1386 rate of particle collisions that are produced by two particle beams. It can be described as a function  
 1387 of the beam parameters, such as: the number of colliding bunch pairs, the revolution frequency, the  
 1388 number of particles in each bunch and the transverse bunch dimensions. The first four parameters  
 1389 are well defined. However, the transverse bunch dimensions have to be determined experimentally  
 1390 during calibration measurements. The ATLAS experiment uses the *van der Meer scan* [67] during  
 1391 low-luminosity runs to calibrate the luminosity detectors. This scan is performed by displacing one  
 1392 beam in a given direction and measuring the rate of interactions as a function of the displacement.  
 1393 The transverse charge density of the bunches can be estimated on the basis of the interaction rate.  
 1394 The calibrated luminosity detectors can then operate during high-luminosity runs.

1395 One approach to luminosity monitoring is to count the number of particles produced by the  
 1396 collisions. The luminosity is then proportional to the number of detected particles. A detector has  
 1397 to be capable of distinguishing individual particles that fly from the interaction point through the



Figure 4.2: A pCVD wafer [?]. The golden dots on the surface are the electrodes that are applied during the qualification test. The wafer is measured across the surface to find the regions with the highest efficiency.

1398 active sensor area. If the detector has at least three layers, it can reconstruct the particles' tracks,  
1399 which in turn yields more information on the their trajectory. This is one reason why detectors  
1400 with a high timing- and spatial segmentation are more suitable for these applications. The second  
1401 reason is that, with a high spatial segmentation, the detector does not saturate even at high particle  
1402 fluencies.

### 1403 4.3 Diamond pixel module

1404 The two most important parts of the diamond pixel module are the sensor, which translates the  
1405 incident ionising radiation into charge carriers as explained in chapter 2, and the pixellated front-end  
1406 chip, which collects the ionised charge with a high spatial segmentation, processes the recorded data  
1407 and sends them to the readout system. This section describes these two parts of the module and  
1408 their interconnection.

#### 1409 4.3.1 Sensors

1410 The DBM modules are instrumented with two types of sensors – pCVD diamond and silicon. The  
1411 silicon sensors are used as a fallback solution because there were not enough high-quality diamond  
1412 sensors available during the construction phase. In addition, a comparative study of irradiation  
1413 damage between silicon and diamond can be made with such a hybrid system.

1414 **Diamond sensors** The target material for this application is pCVD diamond. The reason for this  
1415 is that the active area of an individual sensor must be approximately  $2\text{ cm} \times 2\text{ cm}$ , which is too  
1416 large for the sCVD diamond (maximum sizes available are  $10\text{ mm} \times 10\text{ mm}$ ). pCVD material is also  
1417 a bit cheaper, which makes a detector with a large active area more feasible to build. The material  
1418 is provided by three companies: DDL, E6 and II-IV and it is grown in  $15\text{ cm}$  wafers, as seen in  
1419 figure 4.2. The target thickness of the wafers is  $500\text{ }\mu\text{m}$ . The minimum required charge collection  
1420 efficiency is  $40\%$  ( $\text{CCD} \geq 200\text{ }\mu\text{m}$ ) to ensure that the MPV of the collected charge for MIPs is still  
1421 well above the noise of the electronics even after heavy irradiation. They need to be operated at

### 4.3. DIAMOND PIXEL MODULE

---

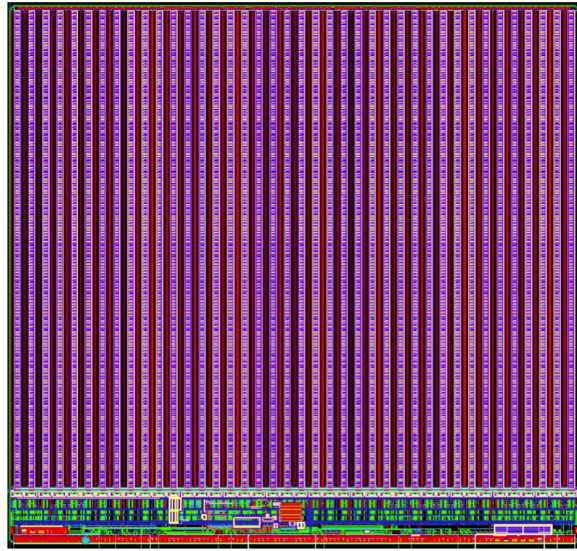


Figure 4.3: FE-I4 layout, top-down view. The pink area are pixels grouped into columns, the green area below is the common logic and the red strip at the bottom are the wire bond pads.

1422 bias voltages between 600 V – 1'000 V. On one side there is a single gold electrode applied across  
1423 the entire surface. On the other side a pixellated metallisation is added.

1424 **Silicon sensors** are standard  $n^+ - in - n$  planar sensors with a 200  $\mu\text{m}$  thickness and were fabricated  
1425 at CiS [68], a company from Erfurt, Germany. They are designed to have nearly a 100 % efficiency  
1426 when not irradiated. One side is segmented into pixels. Guard rings at the edges of the sensor  
1427 provide a controlled drop in potential, reducing the possibility of shorts at maximum design bias  
1428 voltages of the order of 1'000 V.

#### 1429 4.3.2 Front-end electronics

1430 The FE-I4 (front-end version four) [69] is an ASIC pixel chip designed specifically for the ATLAS  
1431 pixel detector upgrade. It is built as a successor to the current pixel chip FE-I3, surpassing it in size  
1432 of the active area ( $6 \times$  larger) as well as the number of channels/pixels ( $10 \times$  more). 336 such FE-I4  
1433 modules are used in the newly installed pixel layer called the Insertable B-Layer (IBL) [70]. The  
1434 DBM is also instrumented with these chips. The FE-I4's integrated circuit contains readout circuitry  
1435 for 26'880 pixels arranged in 80 columns on a 250  $\mu\text{m}$  pitch and 336 rows on a 50  $\mu\text{m}$  pitch. The size  
1436 of the active area is therefore 20.0 cm  $\times$  16.8 mm. This fine granularity allows for a high-precision  
1437 particle tracking. The chip operates at 40 MHz with a 25 ns acquisition window, which corresponds  
1438 to the spacing of the particle bunches in the LHC. It is hence able to correlate hits/tracks to their  
1439 corresponding bunch. Furthermore, each pixel is capable of measuring the deposited charge of a  
1440 detected particle by using the Time-over-Threshold (ToT) method. Finally, the FEI4 has been  
1441 designed to withstand a radiation dose up to 300 MGy. This ensures a longterm stability in the  
1442 radiation hard forward region of the ATLAS experiment.

1443 Each pixel is designed as a separate entity. Its electrical chain is shown in figure 4.4. The bump-  
1444 bond pad – the connection to the outside of the chip – is the input of the electrical chain, connected  
1445 to a free-running amplification stage with adjustable shaping using a 4-bit register at the feedback  
1446 branch. The analog amplifier is designed to collect negative charge, therefore electrons. The output  
1447 is routed through a discriminator with an adjustable threshold. This value in effect defines the level

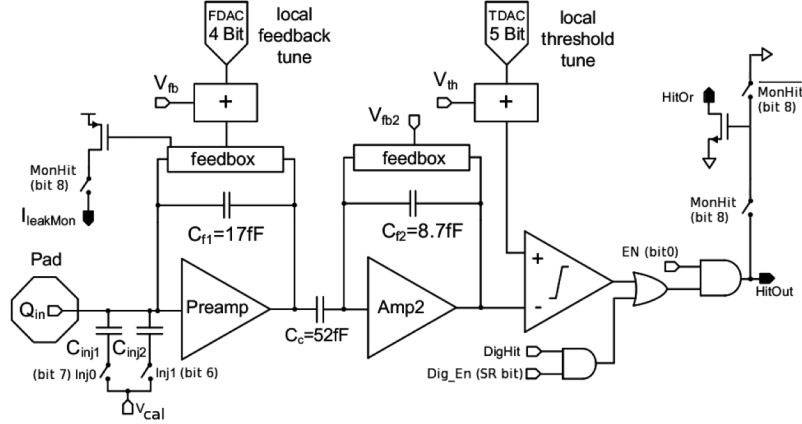


Figure 4.4: Schematic of an analog pixel. Courtesy of the FE-I4 collaboration.

at which the circuit detects a hit. In addition, there is a counter of the clock cycles (25 ns sampling) during which the signal is above the discriminator threshold. The value of the counter is proportional to the collected charge. The logic gates at the end of the chain are used to enable/disable the pixel and to issue a so-called HitOr flag – this signal is set whenever at least one of the pixels was hit and is used as a trigger for the readout. The output of the chain – HitOut – is routed into the logic of the chip where it is buffered and sent out to the readout system. The module receives all its commands from the system via a 40 MHz LVDS line. The commands are either settings for the pixel registers or triggers that start the data readout. The data are sent via an LVDS line at up to 320 Mbit/s, but by default at 160 Mbit/s, four times faster than the clock of the device. This allows the chip to clear out its buffers before new data are recorded, thus avoiding dead time and data pile-up. The FE-I4 has been successfully tested for trigger rates of up to 300 kHz, depending on the occupancy per trigger.

The DBM uses pCVD diamond with  $d_C = 500 \mu\text{m}$  thickness and silicon with  $d_{Si} = 200 \mu\text{m}$  thickness as a sensor material. The resulting most probable value (MPV) of the deposited charge for a minimum ionising particle (MIP) is calculated with the formula  $Q_S = d \cdot E_{e-h}$  and equals 18'000 electrons and 17'800 electrons, respectively, at a full charge collection efficiency. This is not the case with the pCVD material, whereby the expected charge collection efficiency is of the order of 50 % – around 9'000 e. This value further decreases with received irradiation dose. Therefore in order to detect the particles depositing energy on the far left side of the Landau spectrum, the threshold has to be set to a significantly lower value. On the other hand, if the threshold is set too low, it also detects the electronic noise and generates false hits. Typical noise amplitudes are in the range of 120 e – 200 e. A safe threshold range is approximately five times above this value. The target for the DBM is to set the threshold to 800 e.

The analog amplifier is implemented in two stages to get a fast rise time at a low noise and a low power consumption. The output signal of the analog amplifier has a triangular shape with a fast rise time and a long decay. The shape can be adjusted by tuning the amplifier feedback loop. Its length is proportional to the collected charge, but it needs to be calibrated first. This is done by means of two injection capacitors,  $C_{inj1}$  and  $C_{inj2}$ , seen in figure 4.4 with well defined capacitances. First, the charge  $Q_{cal} = V_{cal} \cdot (C_{inj1} + C_{inj2})$  is injected into the analog chain. Then the length of the output pulse is measured and finally the feedback value is changed to either lengthen or shorten the pulse in order to get to the required duration  $t_{cal}$ . The typical values are  $Q_{cal} = 5'000 \text{ e} - 16'000 \text{ e}$  at the

#### 4.4. MODULE ASSEMBLY

---

1479 time  $t_{\text{cal}} = 5 \text{ ToT} - 10 \text{ ToT}$ . The target values depend on the sensor, the type of a radioactive source  
1480 and the application. Therefore the initial threshold  $Th$  at 1 ToT and the calibrated value  $Q_{\text{cal}}$  at  
1481  $t_{\text{cal}}$  ToT give us a linear scale of collected charge with respect to time over threshold. However, in  
1482 practice this relation is nonlinear for lower thresholds, but since the goal of the measurements is to  
1483 track the particles rather than to measure their deposited energy precisely, this is sufficient.

### 1484 4.4 Module assembly

1485 Parts for the detector arrived separately and were assembled into modules at CERN’s DSF lab after  
1486 being checked for production faults. The assembled modules underwent a series of quality control  
1487 (QC) and burn-in tests to determine their quality, efficiency and long-term stability.

1488 A DBM single-chip module consists of a hybrid pixel module, a flexible PCB and the supporting  
1489 mechanics (a ceramic plate and an aluminium plate). The chip arrives already bump-bonded to the  
1490 sensor, be it diamond or silicon. First it is glued to the ceramic plate on one side and to the PCB  
1491 on the other using Araldite 2011 or Staystik 672/472. Staystik is re-workable and has a very high  
1492 thermal conductivity. The latter is important because the FE-I4 chips tend to heat up significantly  
1493 and need a good heat sink. The problem is that it has a curing temperature of 160/170 °C. This  
1494 temperature may cause some unwanted stress build-up between the FE-I4 and the diamond sensor  
1495 due to different coefficients of thermal expansion, pulling them apart. This would disconnect the  
1496 pixels, yielding large regions of the module insensitive to radiation. Araldite 2011 on the other hand  
1497 can be cured at lower temperatures – down to RT – but it has a lower heat conductivity. In the end  
1498 Araldite is used as a safer option. However, due to the longer curing, the entire assembly process  
1499 using Araldite is three times as long. After curing, the module is wire-bonded and attached to the  
1500 aluminium plate using screws made up of a radiation-resistant PEEK polymer. They have to be  
1501 tightened with a great care, because their screw head is only 0.2 mm – 0.6 mm away from the sensor  
1502 edge – the sensor displacement tolerance during gluing is of the order of 0.5 mm. Finally, the module  
1503 is put in an aluminium carrier which protects it from mechanical damage or electrostatic discharges.  
1504 Figure 4.5 shows an assembled module.

### 1505 4.5 Performance results

1506 This section gives an overview of the performance results of the DBM modules achieved during the  
1507 QC and the test beam campaign. The source tests were performed to check for disconnected regions  
1508 in the sensors and to measure the diamond’s efficiency. Only the modules with minimal disconnected  
1509 regions and maximum efficiency were chosen for installation.

#### 1510 4.5.1 Source test results

1511 The modules are tested in the lab using a Reconfiguration Cluster Element readout system [71]  
1512 and a moving stage with two degrees of freedom. They are placed onto the stage and connected to  
1513 the readout system and the power supplies. After ensuring the low- and high voltage connectivity  
1514 they are checked for the signal connectivity. If everything is operational, a series of automated tests  
1515 is run. Each of these tests calibrates a certain value within a pixel, whether it is the signal threshold  
1516 or the value for integrated charge. These are tuned in a way that the response to a predefined  
1517 calibration signal is uniform for all pixels across the sensor. This procedure is referred to as *tuning*.

1518 When the modules are tuned, they are tested using a  $^{90}\text{Sr}$  radioactive source. Two characteristics  
1519 of each module are checked: 1) operation of all pixels and 2) sensor efficiency.

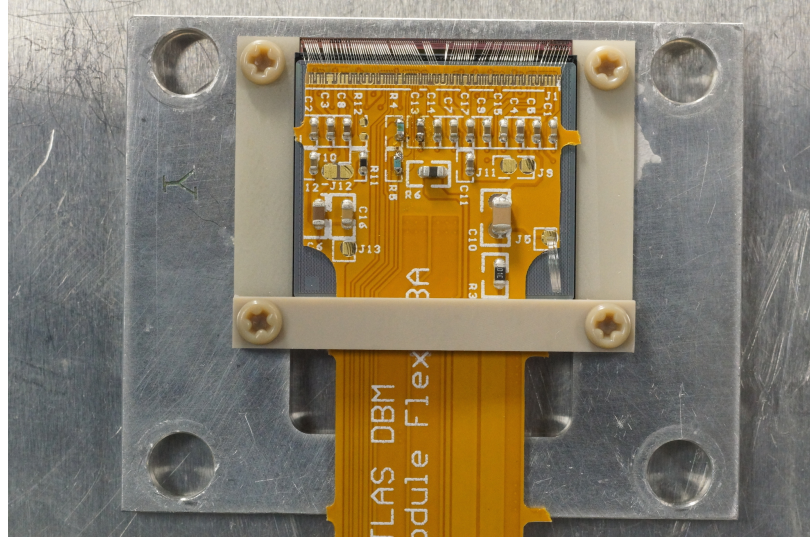


Figure 4.5: DBM module, top-down view. Visible is the flexible PCB with signal and power connections, the silicon sensor and a part of the FE-I4. Wire bonds from the PCB to the FE-I4 and to the sensor are also visible.

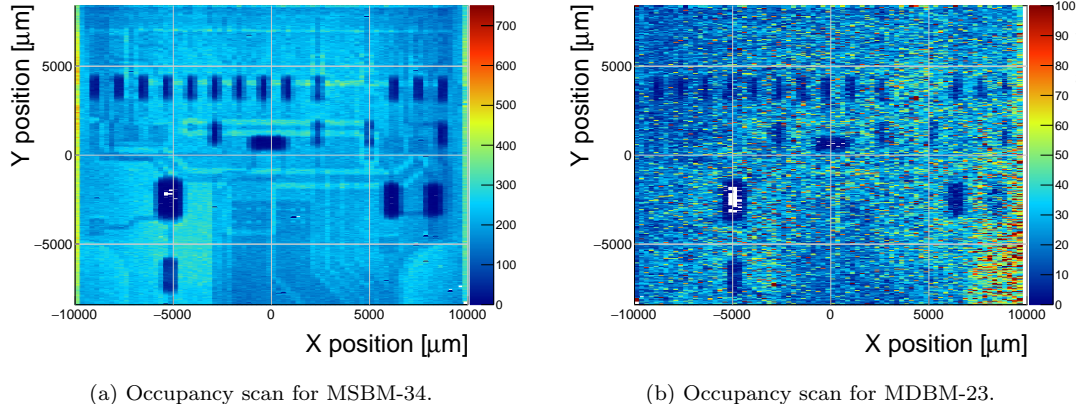


Figure 4.6: Occupancy scans for the silicon (left) and diamond sensor (right) to check for disconnected regions. Shadows of the electronic components are clearly visible because fewer electrons were able to traverse through such a higher amount of material.

#### **4.5.1.1 Pixel connectivity**

The first test is carried out to determine the number of disconnected pixels in the matrix. This is an important step in the DBM QC procedure, because it turns out that a significant portion of the flip-chipped diamond sensors exhibited very poor connectivity. The disconnected regions on the faulty modules ranged anywhere from 0.1 % – 80 % of the overall active surface. In two cases the sensor was even completely detached from the chip. Therefore the pixel connectivity turns out to be the most important qualification factor in the QC procedure. However, the only way to check it at the moment is to fully assemble a module and test it using a radioactive source. If the module turns out to be of poor quality, it is disassembled and sent for rework. The turnover time of this operation is of the order of one month, which affected the DBM installation schedule significantly. In the end the modules with less than 3 % disconnected pixels have been accepted.

## 4.5. PERFORMANCE RESULTS

---

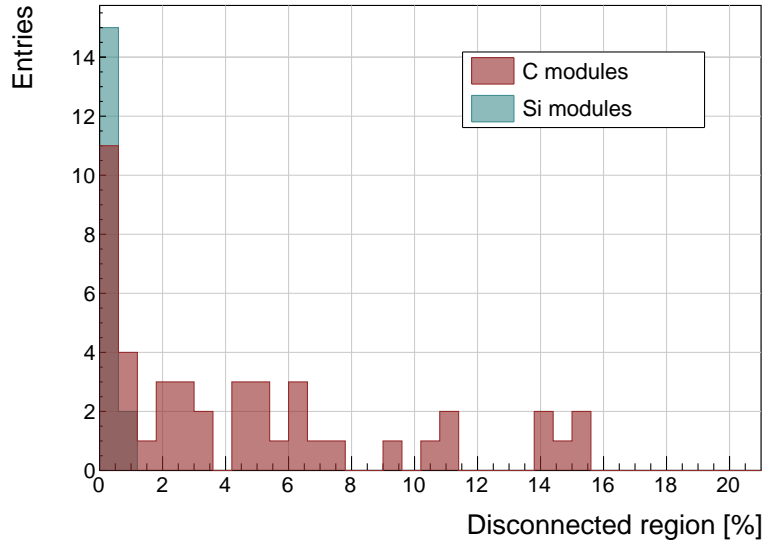


Figure 4.7: Disconnected regions for all modules derived from the occupancy scans.

The test for disconnected regions is carried out by moving the module under the source in X and Y direction so that the exposure over the entire plane is uniform. The resulting occupancy map reveals pixels that are not electrically coupled to the sensor via bump bonds. The occupancy scans are shown in figures 4.6a and 4.6b. The silicon module has a very uniform occupancy plot. So much so that the features of the overlaying flexible PCB can be observed. The rectangular shadows are the passive components whereas the lines are the traces in the PCB. Furthermore, a circular-shaped edge of the PCB can be seen on the bottom right side of the plot. These darker areas are such because fewer electrons can penetrate the material with a high density. In the case of the diamond, the features of the PCB can be observed as well, but are much less distinguishable as the plot is much more granulated – less uniform. This high variance in the diamond’s detection ability is due to the grain boundaries in the pCVD material which trap the drifting charges, rendering some regions significantly less efficient.

Figure 4.7 shows the distribution of disconnected regions across all tested modules. Silicon modules were performing as expected, with a minimum number of disconnected pixels.

### 4.5.1.2 Pseudo-efficiency

Only the modules that passed the pixel connectivity test undergo the second test stage in which the sensor’s efficiency is estimated. A scintillator is placed underneath the module and is used as a trigger. A particle that crosses the DBM module and hits the scintillator, triggers the module readout. In the end, the number of triggers is compared to the number of hits/clusters recorded by the module. These are shown in figures 4.8a and 4.8b.

However, the resulting ratio is only an estimate of the sensor’s detection efficiency. This is because the  $\beta$  particles scatter around the setup and sometimes hit the scintillator from other directions without traversing the module, producing empty triggers. Therefore the real sensor efficiency can only be measured in a high energy particle beam and using a beam telescope as a reference detector to measure the particle trajectories. Nonetheless, this *pseudo-efficiency* gives a rough estimate of the sensor’s quality.

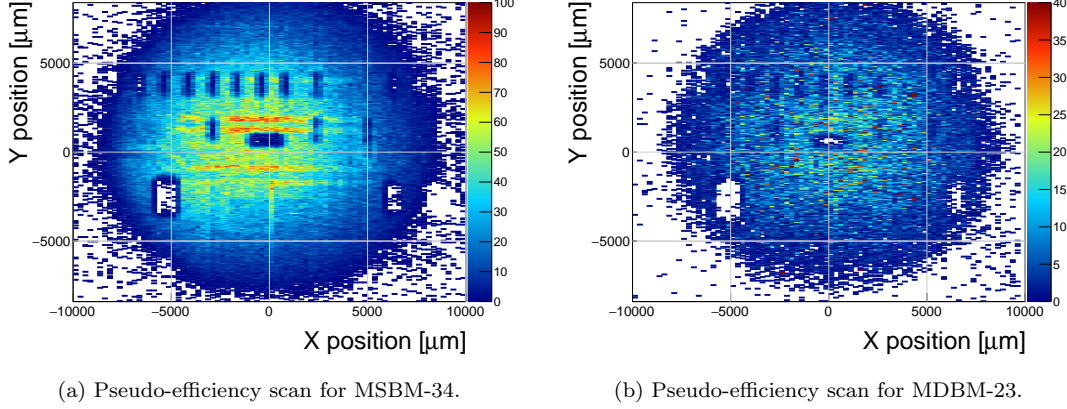


Figure 4.8: Pseudo-efficiency scans for the silicon (left) and diamond sensor (right) to estimate the efficiency of the sensors.

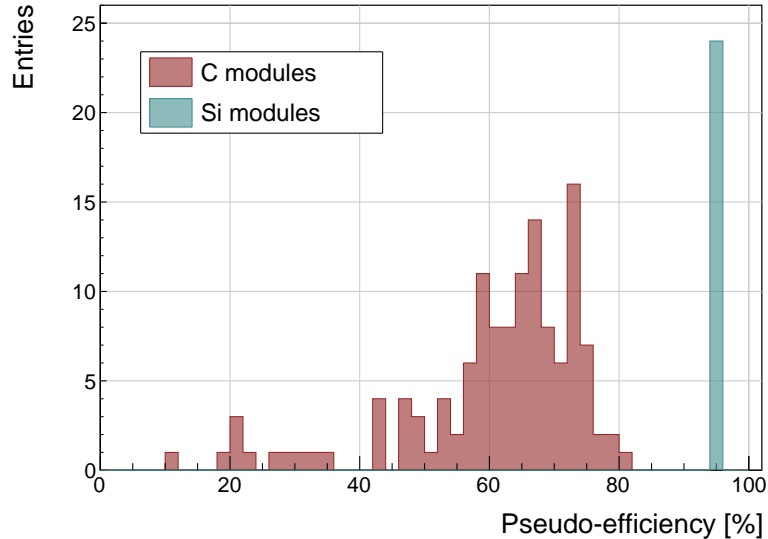


Figure 4.9: Pseudo-efficiencies for all modules at various threshold and voltage settings.

Figure 4.9 shows the distribution of pseudo-efficiencies for all modules that went through the QC. The majority of the silicon modules yield the pseudo-efficiency of  $(94.3 \pm 0.2)\%$ . Silicon sensors being 99.99 % efficient, this value is underestimated by about 5 %. The measured pseudo-efficiency of the diamond modules is  $(65 \pm 7)\%$ , with outliers down to 10 %. The value depends on the diamond quality, the set threshold and the applied bias voltage. The latter two settings are varied to check the behaviour of the modules under various conditions.

#### 4.5.2 Erratic current

A very important parameter for qualifying a module is the erratic current [72] in the sensor. This term describes the leakage current in a pCVD diamond that becomes unstable. It can develop gradually or can be triggered with a  $\beta$  source. Spikes appear in the otherwise stable leakage current. They can be up to three orders of magnitude higher than the base current. Sometimes the current

## 4.5. PERFORMANCE RESULTS

---

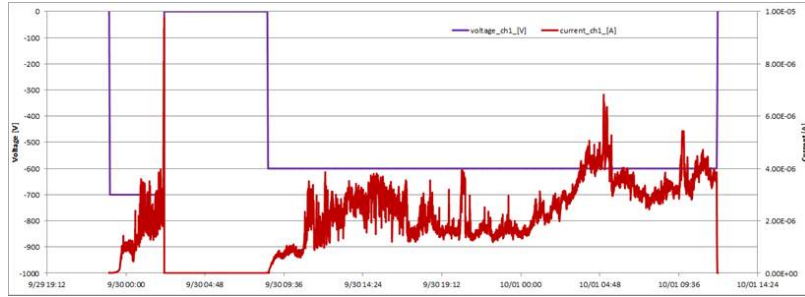


Figure 4.10: Erratic current in a DBM diamond module. The purple and the red signal line represent the applied bias voltage and the measured leakage current.

1568 also suddenly increases for a few orders of magnitude and stays at that level (e.g. from the initial  
1569 1 nA to 3  $\mu$ A). An example of such behaviour is shown in figure 4.10.

1570 The amplitude differs in magnitude from sensor to sensor. This effect is still not fully explained,  
1571 but the hypothesis is that the charges find a conductive channel along the grain boundaries, causing  
1572 discharges. These discharges are picked up by the pixel amplifiers in the FE-I4. A single discharge  
1573 can trigger a group of up to  $\sim$ 500 pixels, resulting in a *blob* on the detector occupancy map.  
1574 Sometimes the conductive channel stays in a conductive state, making one or more pixels always to  
1575 fire. These pixels saturate the bandwidth of the readout channel, so they have to be masked out  
1576 during measurements.

### 1577 4.5.3 Test beam results

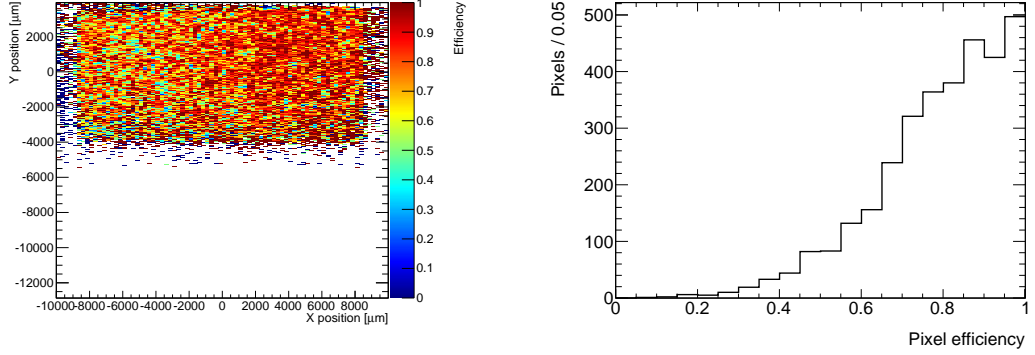
1578 The first two assembled prototype DBM modules, MDBM-01 and MDBM-03, were tested at DESY,  
1579 Hamburg, in a test beam facility. The aim of the measurements was to measure their efficiency, the  
1580 spatial distribution of the efficiency and the effect of the beam on the disconnected regions. A silicon  
1581 module MSBM-02 was measured to crosscheck the measurements. Since the silicon module is almost  
1582 100 % efficient, it was used as an “anchor” – the efficiency of the diamond module was measured  
1583 relative to that of the silicon module. Two beam telescopes were used as reference systems: Kartel  
1584 telescope [73] built by JSI institute from Ljubljana, and EUDET Aconite [74]. Both are instrumented  
1585 with six Mimosa26 pixel planes and capable of tracking particles with a 2  $\mu$ m pointing resolution.

1586 The test beam prototypes did not meet the acceptance criteria for production DBM modules in  
1587 the following areas: first, the stated CCDs were slightly below 200  $\mu$ m, which would be the DBM  
1588 minimum. Secondly, the applied bias voltages ranged from 1–2 V/ $\mu$ m. In addition, the threshold cut  
1589 could only be set to 1'500 electrons, which is higher than the DBM minimum (1'000 e). Nonetheless,  
1590 the resulting module efficiencies were still in the range between 70–85 %.

1591 To analyse the test beam data, Judith software framework [73] was used. Judith is capable  
1592 of synchronising data streams from several detector systems only connected via a trigger system,  
1593 reconstructing tracks and calculating efficiency for the DUTs. It was also used to reconstruct and  
1594 analyse the acquired Kartel test beam data together with the silicon and diamond module as DUTs.  
1595 A sample of the analysed data is shown in figures 4.11a and 4.11b.

### 1596 4.5.4 Summary of the QC

1597 All in all, 79 modules went through the QC procedure – 43 diamond modules and 36 silicon modules,  
1598 12 of the latter only for testing purposes. Figure 4.12 shows their production with time. 18 diamond



(a) This figure shows an efficiency map of ad DBM pVCD diamond module. Each bin corresponds to a single pixel. The triggering scintillator of the Kartel telescope is smaller than the DUT. Hence, the recorded hits can only be seen in the top half of the sensor.

(b) A pixel efficiency distribution from the run in figure (a).

Figure 4.11: An efficiency study of a prototype DBM diamond module in a test beam. The statistics are low ( $\sim 10$  hits/pixel) as the data were collected during a short run.

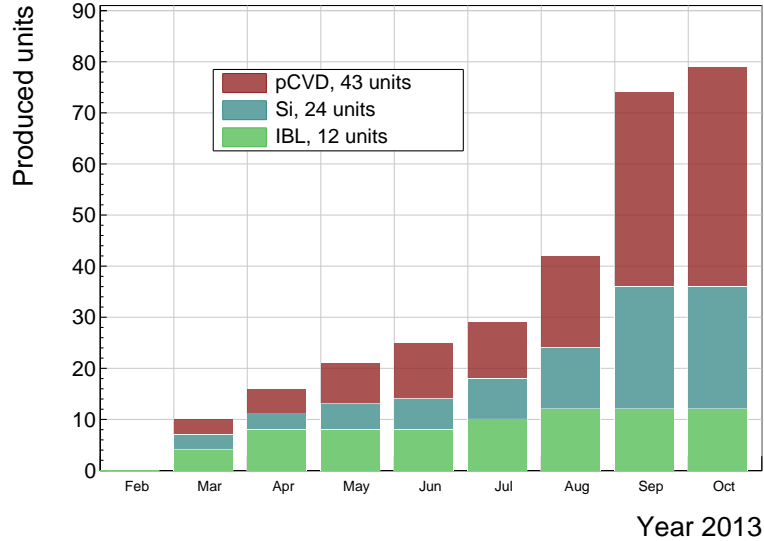


Figure 4.12: Module production with time.

1599 modules and 6 silicon modules were in the end chosen to be integrated into DBM telescopes and  
1600 installed into ATLAS.

## 1601 4.6 Installation and commissioning

1602 The DBM modules that passed the QC tests were assembled into telescopes – sets of three modules  
1603 one behind the other with a spacing of 50 mm. Of the 18 diamond and 6 silicon modules, 6  
1604 diamond and 2 silicon telescopes were built. A special care was taken when choosing the sets of  
1605 three diamonds. The modules with a similar pseudo-efficiency, leakage current, maximum stable high

#### 4.6. INSTALLATION AND COMMISSIONING

---



Figure 4.13: This photo highlights four telescopes installed onto the nSQPs and around the pipe.

voltage and shape of disconnected regions were grouped together. After assembly into telescopes, the modules were tested for their connectivity. Then the high voltage was applied and the leakage current was observed. This was an important point to check because all three modules shared the same high voltage channel. Any instabilities on one of the modules would cause problems on the other two. This would for instance happen if one of the modules had a much lower breakdown voltage. Due to time constraints, the telescopes were not built at the same time but instead the production was pipelined. As soon as two telescopes were ready, they were transported to Point 1 – the site where parts of the ATLAS detector were being put together. There they were prepared for installation onto the pixel detector structure that had been extracted from ATLAS due to pixel detector commissioning. The commissioning was nearing completion, so the technicians were preparing the detector for re-insertion. The cylindrical structure was being enclosed by four new service quarter-panels (nSQPs). This meant that with every day the access to the place of installation of the DBM was more difficult. The first two telescopes were still put into place when only one nSQP was in place. This allowed the installation process to be carried out from both sides. This proved to be helpful, because the process was lengthy and had to be done with great precision. It involved tightening several screws on both sides of the telescopes, adding thermal paste on the aluminium joints and removing the protective covers, revealing the fragile wire bonds. At the same time the surrounding electronics and cables had to be left untouched. The lessons learnt with the first part of the installation were helpful when installing the other telescopes. The last two were fitted onto the structure when three nSQPs were already in place, leaving only a narrow opening for access. The entire procedure was carried out blind. After every installation, the telescopes were tested again. First, the low voltage connectivity was checked and a set of tests was run on the FE-I4 front-end chips. An eye diagram was made to estimate the quality of the signal transmission. Then a  $^{90}\text{Sr}$  source was used to perform a source test on three modules at the same time. Leakage current was observed during the source test. The final test included running four telescopes (all on one side) at a time. All the tests were successful and the DBM was signed off.

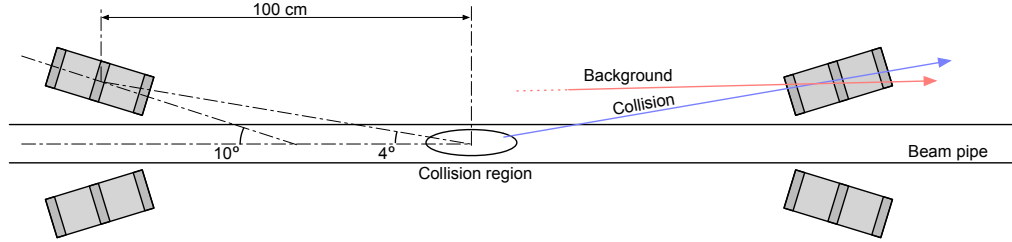


Figure 4.14: Position of the DBM in the ATLAS experiment.

### **4.6.1 Positioning in ATLAS**

The DBM is placed in the forward region of the ATLAS detector very close to the beam pipe, as shown in figure 4.14. Eight DBM telescopes reside approximately 1 m away from the collision region, four on each side. They are tilted with respect to the beam pipe for 10°. This is due to a specific phenomenon connected to erratic (dark) currents in diamond. Studies have shown [72] that the erratic leakage currents that gradually develop in diamond can be suppressed under certain conditions.

For instance, if a strong magnetic field is applied perpendicular to the electric field lines in the diamond bulk, the leakage current stabilises. The DBM was designed to exploit this phenomenon. The magnetic field lines in the ATLAS experiment are parallel to the beam. Hence, an angular displacement of the sensor with respect to the beam allows for the leakage current suppression. However, the DBM telescopes still need to be directed towards the interaction region. Taking these considerations into account, a 10° angle with respect to the beam pipe was chosen. The influence of the magnetic field on the particle tracks at this angle is very low as the field lines are almost parallel to the tracks. The tracks are therefore straight, which reduces the track reconstruction complexity.

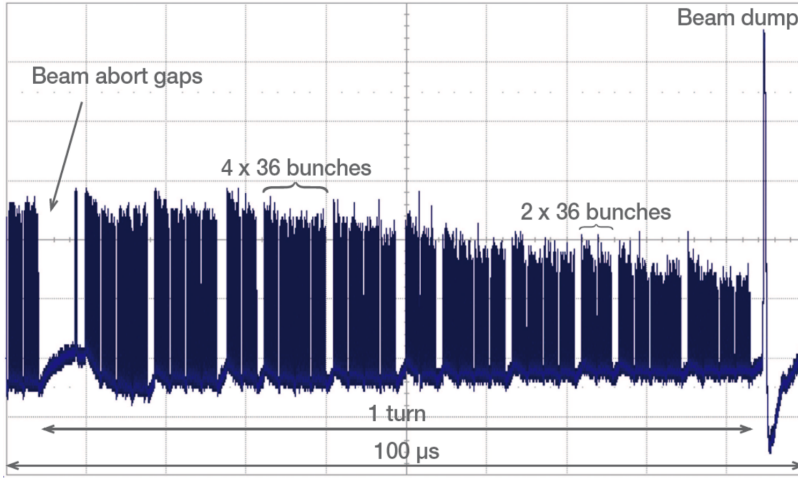


Figure 4.15: Time-resolved bunch structure at the LHC measured by diamond detectors [75]. The beam abort gap is clearly visible.

## 1647 4.7 First collision data

1648 The detector's capability of particle tracking has been tested during collisions. Only one telescope  
1649 was used to take data.

### 1650 4.7.1 LHC beam bunch structure

1651 As described in chapter 1, the LHC accelerates two beams of protons in opposite directions, intersecting at four collision points. Collisions take place in a collision region around the nominal collision point, with a gaussian spread. The particles in the beam are grouped in bunches. Not all bunch buckets are filled, as shown in a time-resolved plot in figure 4.15. Therefore some bunches arriving at the collision point do not have their corresponding bunches traveling in the opposite direction. 1655 These are referred to as non-colliding or *unpaired bunches* while those with their respective bunches in the opposite direction are *paired*. The unpaired bunches should not create any collisions. Nevertheless, 1658 some collisions might still be detected, whether as a result of stray particles hitting the beam pipe or the surrounding detectors or if the purportedly empty buckets still contain a small number of particles. 1660

### 1661 4.7.2 Collision point reference system

1662 If all three planes of the telescope are hit during a bunch crossing, a linear line is fitted to these hits and extrapolated towards the interaction region. This line represents the particle's trajectory. Two 1663 parameters are calculated: the radial distance  $R_0$  and the longitudinal distance  $Z_0$  between the line and the interaction point, as shown in figure 4.16.  $R_0$  and  $Z_0$  values at minimal  $d_0$  are therefore the 1666 cylindrical coordinates of the minimal distance between the particle's trajectory and the nominal 1667 interaction point. Figure 4.17 shows the theoretical gaussian distribution of  $R_0$  and  $Z_0$  (black) as 1668 well as the expected distribution as measured by one DBM telescope (blue). The latter is biased due 1669 to the positioning and the aperture of the telescope. The red distribution shows the contribution of 1670 the particles colliding with the beam pipe and the surrounding electronics, such as the IBL [76].

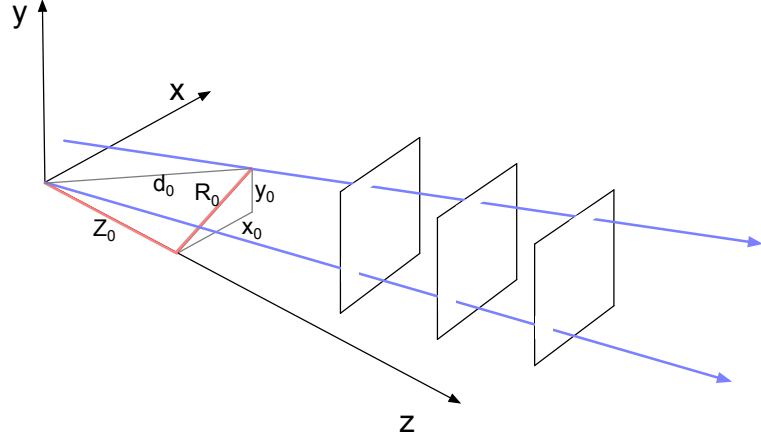


Figure 4.16: Two particle tracks. One originates in the centre of the collision region. The vertex of the other is at the radial distance  $R_0$  and longitudinal distance  $Z_0$  from the interaction point. Axis  $z$  is the beam direction. Three module planes intercept the particles and reconstruct their trajectory. The arrow on the top right shows the telescope used for data acquisition.

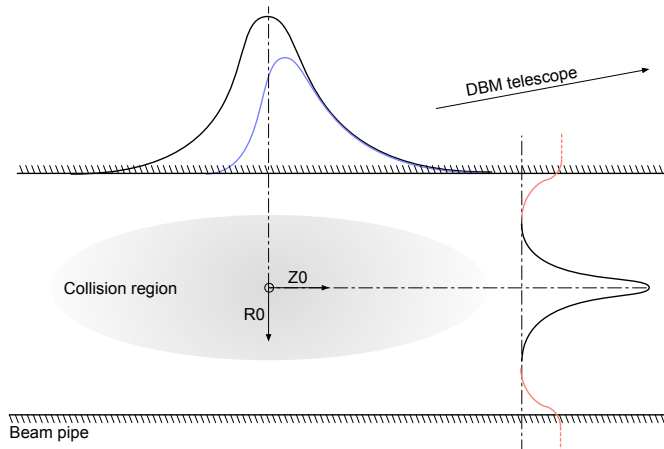


Figure 4.17: Distribution of collisions in the collision region. A single DBM telescope taking data records the collisions with a biased distribution marked blue. The red distributions stem from collisions of particles with the beam pipe or surrounding material.

### 4.7.3 Discussion

The data acquired with a single DBM telescope are shown in figures 4.18a and 4.18b. Histograms for collisions of paired and of unpaired bunches are plotted separately for each of the two cylindrical coordinates. For the colliding bunches, the majority of the reconstructed tracks has the origin close to the nominal interaction point, with a narrow spread in  $Z$  and  $R$ . A slight negative displacement in  $R_0$  and a positive displacement in  $Z_0$  are expected due to the positioning of the telescope.

For non-colliding bunches, the spread is wider. The  $R_0$  distribution has one peak in the middle, which means that the empty buckets still hold some particles which collide. The two peaks on the sides, however, show that a significant number of tracks has their origin at the radius of the beam pipe. Therefore these tracks are made by stray protons colliding with the beam pipe and the

## 4.8. CONCLUSION

---

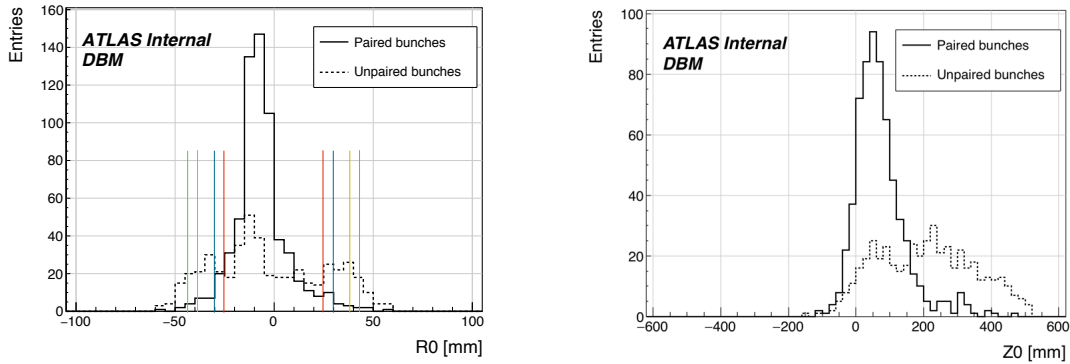


Figure 4.18: These two plots show two parameters of particle tracks recorded by one of the DBM telescopes: radial (left) and longitudinal (right) distance of the projected tracks from the interaction point. Note the different scale on the  $x$  axis. The red, blue, yellow and green lines mark the inner and outer radius of the beam pipe, the outer radius of the IBL and the outer radius of the IBL insertion tube [77, 76].

surrounding material. These collisions are unwanted as they do not produce any meaningful physics while still damaging the ATLAS detector by means of the scattered radiation. The  $Z_0$  distribution has a high spread in the positive direction. This bias is due to the positioning of the telescope. The peak that coincides with that of the paired bunches stems from collisions of stray particles. The second peak with a wide spread is due to collisions with the surrounding material.

## 4.8 Conclusion

The Diamond Beam Monitor has been designed as an upgrade to the existing luminosity detectors in the ATLAS experiment. It is the first diamond pixel tracking detector installed in a high-energy physics experiment. The pixelated front-end electronic chips ensure precise spatial detection of the charged high-energy particles. The projective geometry allows for particle tracking and background rejection. The detector is placed in a high-radiation forward region of the experiment. Therefore, radiation hardness of the chosen pCVD diamond sensors is an important requirement. The tests carried out in the test beam and in the laboratory confirmed that enough detector-grade DBM modules have been built to be installed in the experiment. The DBM is has been running in ATLAS since October 2013.

1696 **Chapter 5**

1697 **Current monitoring**

1698 *Real-time particle identification*

1699 Diamond sensors have a very fast signal response due to their low capacitance. The electrical  
1700 signal created by drifting charge carriers retains its shape without significant distortion. When the  
1701 sensor is used together with a fast current amplifier with a high broadband limit ( $\sim 2$  GHz) and  
1702 a readout device with a similar limit, the information about the drifting charges is retained. For  
1703 instance, a proton creates the free e-h pairs along its trajectory. The electrons and holes start drifting  
1704 immediately. Those closest to the electrodes recombine quickly whereas those at the opposite side  
1705 contribute to the induced signal for longer. The resulting signal is therefore a triangular pulse with a  
1706 steep rising edge and a gentle falling edge. It is possible to determine the drift velocity of the charge  
1707 carriers by measuring the width of the pulse, as was done in chapter 3. Furthermore, it is possible  
1708 to determine with a certain probability what is the type of incident radiation, judging by the shape  
1709 of the induced pulse. This, however, only applies to SCVD diamond material. Its uniform carbon  
1710 lattice allows the ionisation profiles to retain their shape, unlike in pCVD material, laden with grain  
1711 boundaries, or in even in silicon where the shape is deformed due to p-n junction non-uniformities.

1712 This chapter describes an application that carries out particle identification by means of the pulse  
1713 shape analysis. It was developed for measuring activity of a neutron reactor. In this case the device  
1714 has to be able to filter out the photon background with a rate several orders of magnitude higher  
1715 than the neutron rate. Overall detected rate in a neutron reactor can easily exceed  $10^8$  particles  
1716  $\text{cm}^{-2}\text{s}^{-1}$ , depending on the distance of the detector from the reactor core. The device has to be able  
1717 to cope with such high rates. It also needs to be dead time free or at least close to that, to minimise  
1718 the counting error. At these rates, it still has to be able to identify the types of pulse. This type of  
1719 online analysis cannot be done in software. It has to be implemented in an FPGA.

1720 **5.1 Motivation**

1721 Pulse shape analysis (PSA) is a common software tool for analysing sensor response to incident  
1722 particles. It is usually done by means of software that runs over big amounts of data that have been  
1723 acquired and saved to storage. This offline analysis can be repeated and improved. However, the  
1724 saved data take up a lot of storage space. In addition, saving raw waveform data requires a system  
1725 capable of a high data throughput and fast data storing. For instance, an oscilloscope can save up to  
1726 100 signal waveforms per second. This means that there is a high measurement dead time. To avoid  
1727 the high dead times, the software algorithms can be ported to the FPGA where they analyse the

## 5.2. REQUIREMENTS

---

1728 incoming signal in real time. The signal is then discarded and only the analysis results are saved,  
1729 decreasing the storage space significantly.

1730 The offline pulse shape analysis has already been used for particle identification with a diamond  
1731 sensor [78, 79]. An effort has been made to implement an online and real time application for this  
1732 analysis by porting the algorithms into an FPGA. This section first describes the device specifications  
1733 Then it describes in detail the PSA algorithms and the structure of the code. Afterwards it discusses  
1734 the performance results, which showcase the limitations of the device. Finally it describes the data  
1735 acquired with radioactive sources and in neutron reactors.

## 1736 5.2 Requirements

1737 Chapter 3 shows that the shape is heavily dependent on several factors, such as environmental  
1738 temperature and received irradiation dose. At temperatures lower than 150 K the signal from an  $\alpha$   
1739 starts deteriorating due to recombination of charges in the charge cloud. Sensor irradiation, on the  
1740 other hand, introduces charge traps, which cause the signal to decay exponentially. These two factors  
1741 are a significant limitation for particle identification. Priming can improve the charge collection and  
1742 longterm stability of the pulse shapes. To improve the measurement further, a high bias voltage has  
1743 to be applied, increasing the measurement SNR.

Factor	Operating range
Sensor material	sCVD diamond
Sensor thickness	500 $\mu\text{m}$
Temperature	150 K – 400 K
Radiation dose	$1 \times 10^{13}$ neq $\text{cm}^{-2} \text{s}^{-1}$
Charge carriers	holes
Bias voltage	$\sim 1 \text{ V } \mu\text{m}^{-1}$
Signal-to-noise	5

1745 Table 5.1: Limitations to particle identification.

## 1746 5.3 Device specifications

1747 The ROSY box has a single BNC input with the termination  $50 \Omega$  or  $1 M\Omega$  with a DC or AC  
1748 coupling. The analog chain has a 250 MHz bandwidth limit. The input range can be set from  
1749  $\pm 50 \text{ mV}$  up to  $\pm 5 \text{ V}$ . The signal offset can be set to any value within this range. The ADC samples  
1750 this signal with an 8-bit precision at a rate of up to 5 GSPS. The PSA uses the highest sampling to  
1751 achieve width measurement resolution of 0.2 ns. The spectroscopic application does not need such  
1752 a fine timing resolution and therefore operates at a reduced sampling rate of 0.8 ns. The amplitude  
1753 resolution depends on the chosen input range, but at 256 ADC counts per sample, it can be as low  
1754 as  $0.39 \text{ mV s}^{-1}$  at the range of  $\pm 50 \text{ mV}$  and as high as  $39 \text{ mV s}^{-1}$  at the range of  $\pm 5 \text{ V}$ .

1755 The logic structure of the PSA is designed using VHDL and runs on Xilinx Virtex 5. The PSA is  
1756 capable of a maximum counting rate of  $1.56 \times 10^8$  pulses per second, yielding a 6.4 ns double pulse  
1757 resolution. The analysis is more time consuming; the maximum throughput rate of the pulse shape  
1758 analysis is  $\sim 6 \times 10^6$  pulses per second. This means that after every pulse, the device has a dead  
1759 time of approximately  $(200 \pm 15)$  ns, depending on the width of the pulse being analysed. Any pulse  
1760 arriving during the analysis of the previous one is counted, but not analysed. Any two pulses with  
1761 the distance between the rising edges lower than 6.4 ns are counted as a single pulse.

1762 The device is very sensitive to noise pick-up. Therefore the setup must be designed to minimise  
1763 the pick-up by means of proper shielding, use of high-quality cables etc. The relatively low bandwidth

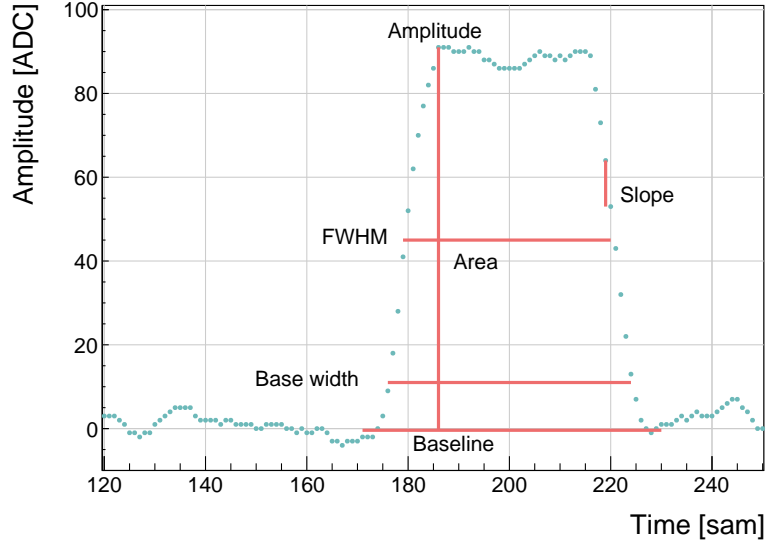


Figure 5.1: Pulse parametrisation.

1764 limit filters out some high-frequency noise, but not the ringing or higher noise spikes. That is the  
1765 task for the PSA.

## 1766 5.4 Pulse parameters

1767 A signal pulse on the input is parametrised during the analysis process. The PSA measures its  
1768 amplitude, area, width at the baseline and at half the maximum amplitude, and the slope of its  
1769 falling edge, as shown in figure 5.1. The amplitude is the difference between the baseline and the  
1770 highest sample in the pulse and is given in ADC counts as an 8-bit value. The area is defined as  
1771 the sum of amplitudes of all samples between two defined boundaries within the pulse. The width is  
1772 defined as the number of samples with a value higher than a set amplitude threshold. If the threshold  
1773 is at half the maximum amplitude, the resulting width is *full width at half maximum* (FWHM). The  
1774 falling slope is the maximum negative difference between values of two samples and is given in ADC  
1775 counts per sample.

1776 The most important pulse parameter is the pulse area. It is equal to the deposited charge of the  
1777 particle. It is also directly proportional to the energy of the particle that is stopped in the sensor.  
1778 The area distribution of a particle is therefore its energy spectrum. This is the target measurement  
1779 for all radiation types. All subsequent parameters are shown as a function of the pulse area:

- 1780 - FWHM [w, a]
- 1781 - Base width [bw, a]
- 1782 - Amplitude [A, a]
- 1783 - Amplitude  $\times$  Base width [A  $\times$  bw, a]
- 1784 - Base width-FWHM [bw-w, a]
- 1785 - Falling slope [s, a]

1786 The Amplitude  $\times$  Base width qualifier is referred to as the *calculated area*. The ratio between the  
1787 calculated area ( $a$ ) and the measured area ( $A \times BW$ ) is the *Form Factor* and is shown in figure 5.2.

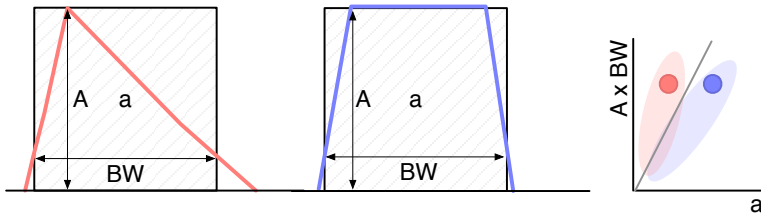


Figure 5.2: Form Factor. The red and blue dot in the right plot are the value entries of the two pulses shown. The red and blue oval shapes depict the regions for the values expected for triangular and rectangular pulses. By carefully choosing the linear qualifier (black line) and taking only the entries below the cut rectangular pulses can be identified.

1788 A Form Factor value of 1 means that the pulse shape is similar to a rectangle. A value of 2 means  
 1789 that the pulse has a triangular shape.

## 1790 5.5 Applications

1791 The FPGA firmware is designed for systems instrumented with CIVIDEC amplifiers and CIVIDEC  
 1792 sCVD diamond detectors. Three applications are available: *Spectroscopy*, *Pulse Shape Analysis* and  
 1793 *Counter*, each optimised for a specific task. Their capabilities are described below. The firmware  
 1794 runs in ROSY, a readout system produced by CIVIDEC.

1795 **Spectroscopy** is a tool for measuring energy spectra of radioactive sources. It is used in combination  
 1796 with the CIVIDEC Cx spectroscopic charge amplifier. The signal from the charge amplifier is  
 1797 analysed in real time. The FPGA measures the maximum amplitude of the signal. The amplitude  
 1798 value is ready at the end of the pulse and is stored in the amplitude histogram. Immediately after,  
 1799 the analysis is reset and the system is ready for a new acquisition. Upon request from the software,  
 1800 the histogram is read out, during which the analysis is paused. In addition to the histogram building,  
 1801 the firmware can also store raw pulse waveforms, which can be then read out by the software. The  
 1802 maximum allowed throughput is 1 million counts per second.

1803 **Pulse Shape Analysis** is a tool for measuring energy spectra of radioactive sources, with an ad-  
 1804 dditional feature. It can identify the type of radiation detected by the diamond detector. By means  
 1805 of the pulse analysis it can subtract the background radiation and only measure the signals from  
 1806 the defined radiation source. It is used in combination with the CIVIDEC C2 broadband current  
 1807 amplifier. The firmware receives a current pulse from the detector and digitises it. The pulse is then  
 1808 analysed and parametrised. The analysis module measures its maximum amplitude, full width at  
 1809 half maximum (FWHM), baseline amplitude, falling slope and its area. Then it compares the ob-  
 1810 tained pulse parameters with the qualifiers set by the software and determines what type of radiation  
 1811 hit the diamond detector. Depending on the qualifiers, the pulse can either be *accepted* or *rejected*.  
 1812 The firmware then stores the parameters of the analysed pulse into histograms. Two histograms  
 1813 exist for each parameter: one for all pulses and one for accepted pulses. In addition, there is one  
 1814 2D histogram (a scatter plot), which can plot two parameters one with respect to the other. Upon  
 1815 request from the software, all histograms are read out, during which the analysis is paused. The  
 1816 maximum allowed throughput is 1 million counts per second.

1817 **Counter** is a tool that measures the count rate and the mean time during counts. It is used in  
 1818 combination with the CIVIDEC Cx, C6 or C2 amplifier. It contains one histogram which holds the

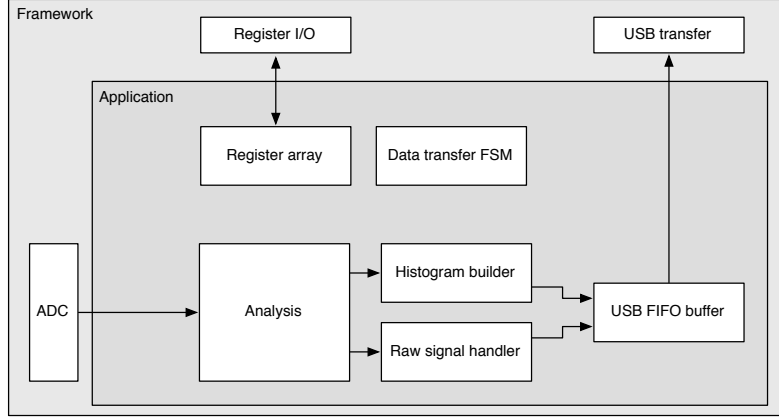


Figure 5.3: Firmware design structure.

1819 information about the mean time during counts. The counter is operational also during the readout  
 1820 of the histogram. The highest counting rate with enabled histogram writing is  $3 \times 10^7 \text{ s}^{-1}$ .

## 1821 5.6 Description of the firmware

1822 The applications are built on top of the Picotech platform. The base code handles the communication  
 1823 between the software and the hardware. Furthermore, it provides the interface to the ADC data,  
 1824 the input/output registers and the USB data transfer. The applications have a set of modules  
 1825 that handle the data input and output and a module for signal analysis, as shown in figure 5.3.  
 1826 The data handling modules are very similar in all the applications to ensure compatibility of the  
 1827 communication between software and firmware and the readout data format. The analysis module,  
 1828 however, is different from one application to the other. The data handling layer is the same for all  
 1829 applications and consists of the final state machine (FSM), the histogram builder, the raw signal  
 1830 handler, the USB FIFO buffer and the register array.

1831 The firmware is written entirely in VHDL. The diagram in figure 5.3 shows the module architecture.  
 1832 The ADC provides the module with 32 digitised signal samples every clock cycle (6.4 ns). The  
 1833 signal is routed directly to the pulse analyser and into the raw signal handler. The analyser outputs  
 1834 are connected to the I/O registers and to histogram buffers. Both the histogram buffers and raw  
 1835 signal buffers are connected to the USB FIFO through a multiplexor. The firmware communication  
 1836 to the controller is done via input/output (I/O) registers (control and status registers, counters) and  
 1837 serially via USB (histogram data, waveforms).

### 1838 5.6.1 Design constraints

1839 **Speed** The ADC provides 32 8-bit samples on every 6.4 ns clock cycle. It is not possible to e.g.  
 1840 sum all 32 values in a single cycle, because the summation takes too long to complete. This is why  
 1841 the summation has to be pipelined and carried out in three cycles. This adds up to the analysis  
 1842 duration, which in turn decreases the maximum pulse rate.

1843 **Firmware size** The PSA application makes use of a number of FIFO and RAM buffers to store the  
 1844 pulse waveforms and histograms. 48 32k block RAM modules have been used for the implementation,  
 1845 maxing out the available block RAM memory space on this FPGA. The analysis algorithm also takes

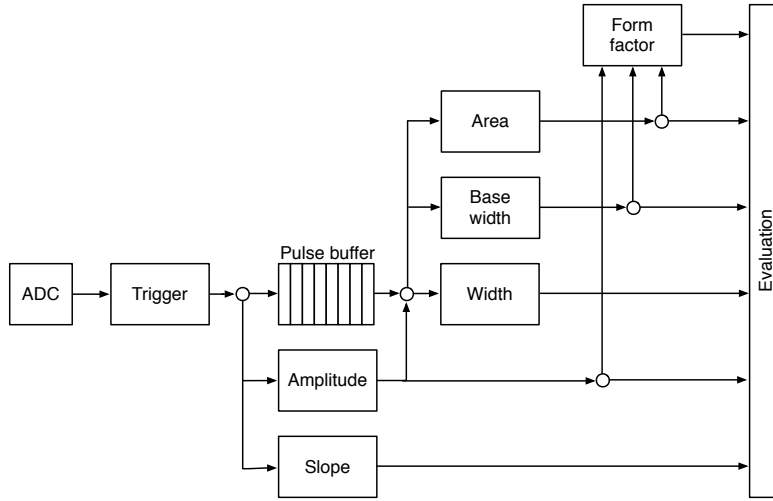


Figure 5.4: Code design plan.

1846 up a significant portion of the FPGA. Many of the operations are carried out on 256-bit long numbers  
 1847 received from the ADC, which quickly fills up the available logic. This is also why the place and  
 1848 route procedure takes a long time.

1849 **Power consumption** The reduction of the power consumption is not crucial for the intended  
 1850 applications.

### 1851 5.6.2 Analysis module

1852 This module is different for different applications. The Pulse Shape Analysis (PSA) application has  
 1853 the most complex module design. The spectroscopy application only uses a small part of that design  
 1854 and the Counter application an even smaller one.

1855 The analysis (or parametrisation) is carried out in several steps, as shown in figure 5.4. The  
 1856 triggering block starts the readout upon signal threshold crossing. The maximum slope of the  
 1857 falling edge is observed. The Amplitude block calculates the pulse height and retains the maximum  
 1858 amplitude while pushing the signal into the pulse buffer. Then the entire pulse is clocked out of  
 1859 the buffer while its FWHM, baseline width and area are measured. Finally, the Form factor is  
 1860 calculated. At the end the Evaluation block takes in all the parametrised information and classifies  
 1861 the pulse according to user-defined cuts.

1862 **Triggering** module handles signal polarity swapping, triggering on threshold and defining the trig-  
 1863 ger window. The real-time processing algorithm allows for a positive or an inverted input signal.  
 1864 However, the PSA only handles positive-polarity pulses. Therefore a negative signal is swapped  
 1865 in the *triggering* block. Signal analysis and readout are then triggered when the signal crosses a  
 1866 user-defined threshold. In addition, the signal has to be over the threshold for a defined number of  
 1867 samples. This is to avoid triggering on noise spikes. A double clock cycle delay is used on the signal  
 1868 to make sure that the recorded signal window includes the rising edge of the pulse as well as some  
 1869 baseline before it. A *trigger active* signal marks a window that contains the entire pulse including  
 1870 some baseline signal before and after it. The trigger can be vetoed by three signals: if the pulse  
 1871 analysis is still taking place, if the input signal exceeds the maximum voltage range or if the data  
 1872 transfer FSM is pausing the analysis due to data transfer to the controller.

1873 **Amplitude** block calculates the pulse height from the difference between the pulse and the baseline.  
1874 It also finds the position of the maximum amplitude within the clock cycle. It receives 32 8-bit  
1875 samples from the triggering block every clock cycle. Time delays in the logic prevent it to find the  
1876 maximum value of the 32 samples within one clock cycle (6.4 ns). Therefore the decision logic has  
1877 been pipelined in three stages, which means that the final maximum value is ready three clock cycles  
1878 after the end of the pulse.

1879 **Pulse buffer** is a FIFO that stores the signal while its amplitude is being measured. At the end  
1880 of the pulse the FIFO is read out so that the remaining measurements can take place.

1881 **Width** block uses the maximum amplitude to determine the *half-maximum* and to measure the  
1882 FWHM. To do so, it counts the samples that are above the half-maximum amplitude. However,  
1883 this method might also count high enough noise spikes before or after the pulse. Hence an improved  
1884 method, which “cleans” the measurement of unintentional additional noise, has been implemented.  
1885 It is described in section 5.6.3.

1886 **Baseline width** block is the same as the Width block, but it measures the width either at 50 %,  
1887 25 %, 12.5 % or 6.25 %, depending on the setting in the register. It also makes use of the special  
1888 method described in 5.6.3 to avoid overestimations due to including noise in the measurement.

1889 **Area** block measures the pulse area by summing up the amplitude values of the samples in the  
1890 pulse. The boundaries of the summation are defined with the crossing of the amplitude above a  
1891 certain threshold. Only the samples between those boundaries are summed up. The boundaries  
1892 can be set at 50 %, 25 %, 12.5 % or 6.25 % of the maximum amplitude of the pulse. The area  
1893 measurement makes use of the same routine as the FWHM and Baseline width block to remove the  
1894 potential outlying samples.

1895 **Falling slope** block measures the highest negative difference between amplitudes of two adjacent  
1896 samples, thus getting the maximum negative slope of the pulse. It is an experimental routine, only  
1897 used for academic purposes.

1898 **Form factor** block is used as a special qualifier for particle identification. It compares the weighted  
1899 measured area of the pulse with its weighted calculated “form”, which is defined as the multiplication  
1900 of the measured amplitude and baseline width. The equation is as follows:

$$x \cdot a - y \cdot A \cdot BW \geq 0, \quad (5.1)$$

1901 where  $a$  is the measured area,  $A$  is the amplitude,  $BW$  is the baseline width and  $x$  and  $y$  the  
1902 weighting factors for the measured and calculated area, respectively. The output of the block is the  
1903 boolean result of this equation.

1904 **Evaluation** block takes in all the parameters from the analysis blocks and compares them against  
1905 the user-defined qualifiers. If the parameters are within the bounds, the pulse is accepted, otherwise  
1906 it is rejected. The corresponding counters within the block are incremented.

### 1907 5.6.3 Area and width measurement

1908 The routine for measuring pulse area and width must have a specific algorithm implemented to carry  
1909 out the measurements correctly. The core point is that the routine precisely defines the edges of a  
1910 pulse. It does so by means of *vector cleaning*, presented in figure 5.5. An important input, beside the  
1911 ADC data and the measurement threshold, is the position of the sample with the highest amplitude.

## 5.6. DESCRIPTION OF THE FIRMWARE

---

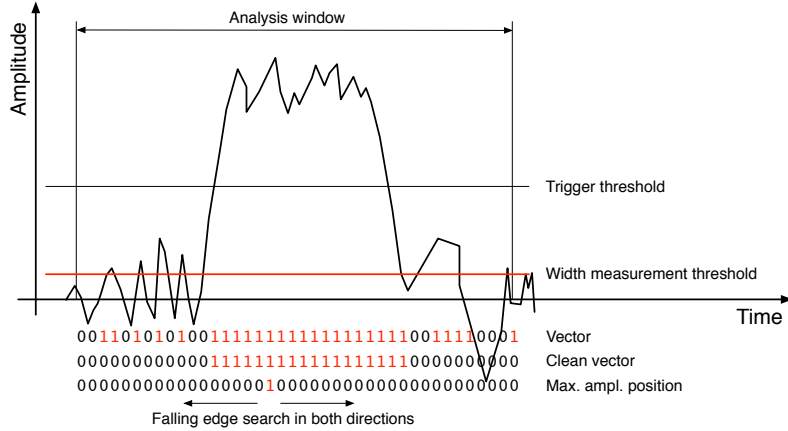


Figure 5.5: A sample pulse. The first vector shows which samples are above the width measurement height. The second vector is a clean vector. The third line shows the position of the maximum amplitude. The vector cleaning algorithm starts from the maximum amplitude and continues in both ways along the vector.

1912     The signal arrives from the ADC as a set of 32 8-bit samples every every clock cycle with a period  
 1913     of 6.4 ns. All 32 samples are compared against the width measurement threshold. If a sample value is  
 1914     equal or higher than this threshold, a binary 1 is set in a 32-bit *vector* on the position corresponding  
 1915     to the position of the sample in the incoming ADC data set. The resulting vector might also include  
 1916     some noise at the edges of the pulse, depending on the height of the width measurement threshold.  
 1917     The old routine simply counts the binary ones in this vector to get the pulse width. This works well  
 1918     for measuring the FWHM because the threshold was high. However, for width measurements at  
 1919     25 %, 12.5 % or 6.25 % of the pulse height this might already become a problem, because the noise  
 1920     might be counted in as well. This is why the new routine cleans the outliers in this vector before  
 1921     counting the remaining ones in the clean vector.

1922     The routine starts from the position of the maximum height. It follows the vector in both ways  
 1923     and finds the first falling edge (0 at this position and 1 at the previous one). From there on it  
 1924     rewrites any binary 1 with a binary 0. The resulting clean vector only has one bunched set of binary  
 1925     ones which are summed, yielding a precise pulse width. The area measurement is similar - it only  
 1926     integrates over the samples marked in the clean vector. Both measurement routines, for area and  
 1927     for width, are implemented separately so that the area routine can have a different threshold set.

1928     This section explains how the algorithm is designed. First, the idea for it was tested using Excel  
 1929     and was only afterwards ported to the VHDL. The underlying algorithm first cleans the vector. Then  
 1930     it passes the cleaned vector either to the width or area measurement, as shown in figures 5.6 and 5.7.  
 1931     The width measurement module only sums the ones in the vector whereas the area measurement  
 1932     module sums the data samples marked by the cleaned vector. Both modules issue a *valid* signal  
 1933     when they finish the measurement.

### 1934     5.6.3.1 Vector cleaning

1935     This is the most important block. Its inputs are: *vector*, *parsing active*, *position of the max.*  
 1936     *amplitude (PA)* and *its delay (DA)*. PA is a 32-bit binary number that shows the position of the  
 1937     sample with the maximum amplitude within the data block whereas the DA tells us how many clock  
 1938     cycles after the start of the parsing this PA block is. The vector cleaning module is designed as a

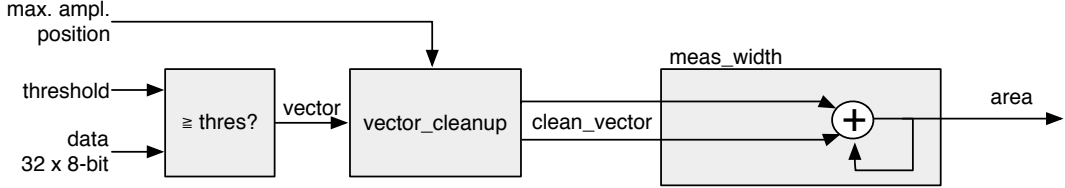


Figure 5.6: This block counts the remaining binary ones in the clean vectors and outputs this value as the pulse width.

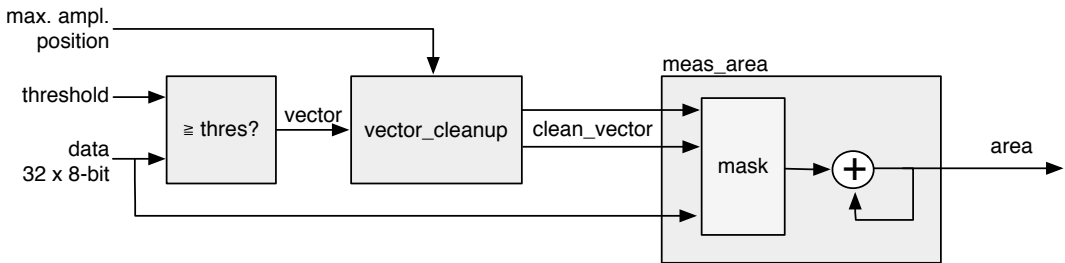


Figure 5.7: This block masks the input data with the clean vector and sums the remaining samples.

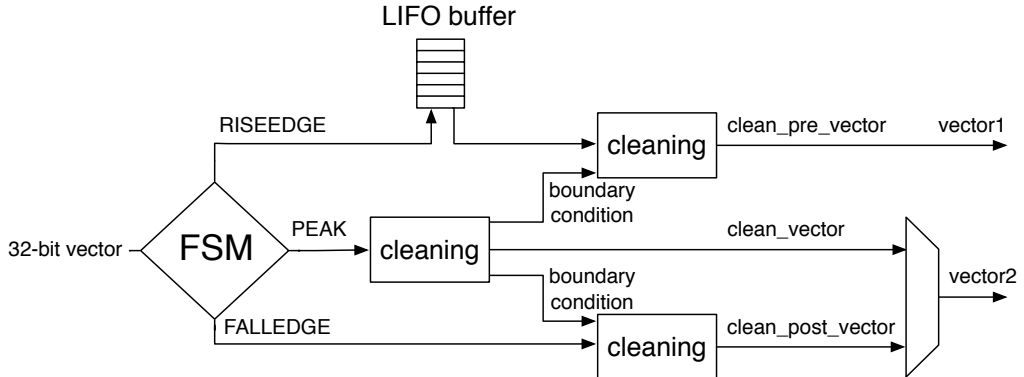


Figure 5.8: Vector cleaning routine outputs two vectors - one forward in time and one back in time from the peak of the pulse.

<sup>1939</sup> final state machine (FSM) with the states IDLE, RISEEDGE, PEAK, FALLEDGE and READY.  
<sup>1940</sup> The FSM is idle until it receives the *active* signal from the external module, marking that the vector  
<sup>1941</sup> parsing has commenced. It switches to RISEEDGE, which starts two procedures: 1) it fills the  
<sup>1942</sup> vector of the pulse's rising edge into a last-in-first-out (LIFO) buffer and 2) counts down from the  
<sup>1943</sup> DA value. When this counter reaches 0, the FSM changes its state to PEAK because the current  
<sup>1944</sup> vector on the input is the one containing the maximum amplitude. This data block is sent through  
<sup>1945</sup> the *peak algorithm*, which cleans the vector. The FSM switches to FALLEDGE state. Now both the  
<sup>1946</sup> previously buffered vector of the rising edge and current vector of the falling edge go through the  
<sup>1947</sup> *pre- and post- algorithm* where they are cleaned, but they get their boundary conditions from the  
<sup>1948</sup> *peak algorithm*. The output of this module is therefore two cleaned vectors in parallel – one forward  
in time and the other backwards.

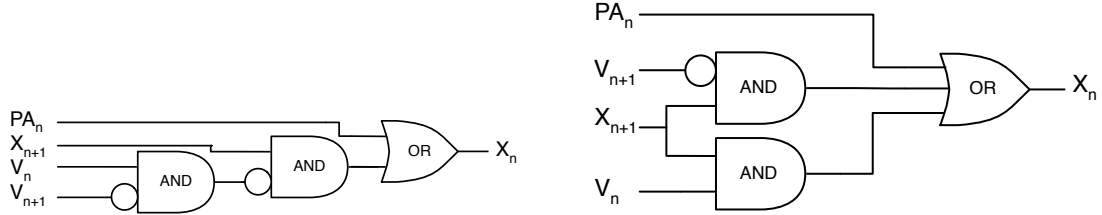


Figure 5.9: One logic step in the algorithm chain before and after Karnaugh minimisation.

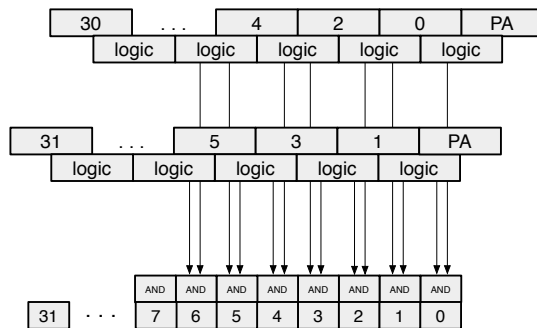


Figure 5.10: The vector is divided into two 16-bit logic chains. The algorithm logic is then run on the two chains separately. The results are then merged into one 32-bit clean vector by using a set of AND gates.

1950 **5.6.3.2 Algorithm**

1951 The underlying algorithm is sequential - it carries out a logic operation on vector bit on position 0,  
1952 uses the output of this operation for the operation on bit on position 1 and so on. This means that  
1953 it has to carry out 32 logic operations per clock cycle. With each operation taking approximately  
1954 0.3 ns, the entire logic chain takes approximately 10 ns to complete. With only 6.4 ns per clock  
1955 cycle, this means timing errors would occur. To fix the problem, a more complicated *decimated*  
1956 *algorithm* has been designed. It consists of two parallel logic chains. Each of the two only takes  
1957 every second bit into account (Chain one: 0, 2, 4 ..., 30. Chain two: 1, 3, 5 ..., 31). This makes the  
1958 chains effectively 16 bits long. The algorithm is run on the two chains and the results are merged  
1959 together at the end as shown in figure 5.10. This effectively reduces the number of sequential logic  
1960 operations to 18, which is within the timing constraints.

1961 **5.7 Control and data interface**

1962 Communication between the device and the controller PC is done via the API functions provided by  
1963 the producer. In addition, the API used by CIVIDEC has access to several extra functions. These  
1964 allow the user to download a customised bitfile to the FPGA, access the I/O registers and use the  
1965 USB data transfer.

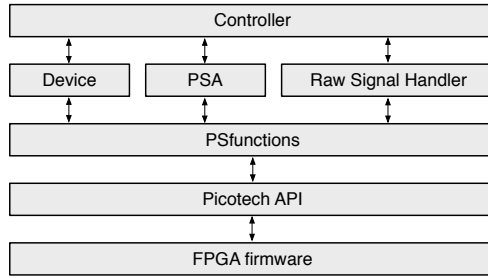


Figure 5.11: Abstraction levels of the controller software.

### <sup>1966</sup> 5.7.1 Software

<sup>1967</sup> The software has been designed in C++ in several levels of abstraction. Figure 5.11 shows the  
<sup>1968</sup> structure of the classes. The classes Device, PSA and RawSignalHandler are there to make it easier  
<sup>1969</sup> to read and understand the controller code. In principle the PSfunctions can also be accessed directly  
<sup>1970</sup> by the controller, but for this the instruction sequences must be well known and understood.

### <sup>1971</sup> 5.7.2 Data readout

<sup>1972</sup> The device records the data in two forms - as signal waveforms and as histograms of analysed pulse  
<sup>1973</sup> parameters. Both are available upon request from the controller. Only one of the two can be  
<sup>1974</sup> transferred via the USB line at a time.

<sup>1975</sup> The waveforms are saved into a FIFO buffer, which can hold up to 64 pulses of the length  
<sup>1976</sup> of  $\sim$ 500 samples. The data format for each pulse is such that it starts with a header containing  
<sup>1977</sup> the pulse timestamp and the sequential number, continues with the data samples and ends with  
<sup>1978</sup> a header containing all the measured parameters (width, amplitude, area, falling slope and form  
<sup>1979</sup> factor). When the FIFO is full, it issues a flag, which tells the controller that the data buffer is  
<sup>1980</sup> ready for readout.

<sup>1981</sup> The histograms are implemented into the FPGA's Block RAM. Their sizes range from 256 to  
<sup>1982</sup> 4'096 bins (8-bit to 12-bit histograms, respectively), depending on the required histogram resolution.  
<sup>1983</sup> For instance, the width parameter is measured with a 0.2 ns resolution and the expected maximum  
<sup>1984</sup> pulse width is less than 20 ns. This yields the maximum range of 100 bins, making an 8-bit histogram  
<sup>1985</sup> sufficiently large. The amplitude histogram range is defined by the 8-bit resolution of the ADC.  
<sup>1986</sup> The area measurement, however, yields higher values and can therefore have a more refined 12-bit  
<sup>1987</sup> binning. Finally, a single 12-bit 2D histogram is included, with six bits for every axis. It is used as  
<sup>1988</sup> an online scatter plot for comparing two measured parameters. An example for it is a comparison  
<sup>1989</sup> of the width against the area, which can help the user determine the cuts that need to be applied  
<sup>1990</sup> to the measurement. All implemented 2-D plots are shown in section 5.9.

## <sup>1991</sup> 5.8 Performance results

<sup>1992</sup> The PSA was tested in the laboratory first using a pulse generator and then with a radioactive  
<sup>1993</sup> sources. This section contains the results of the performance tests.

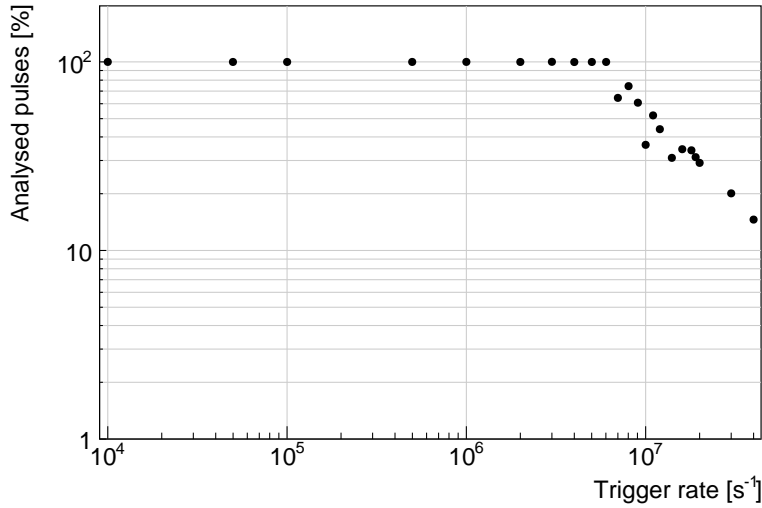


Figure 5.12: This figure shows the capability of the device to analyse all arriving pulses for a range of input frequencies. The highest achievable rate with zero lost pulses is  $6 \times 10^6 \text{ s}^{-1}$ .

### 5.8.1 Tests with a pulse generator

#### 5.8.1.1 Trigger rate

A pulse generator was used to verify the highest achievable rate at which the PSA still analyses every incoming pulse. The final state machine implemented in the pulse analysis module prevents the triggering block from issuing a trigger due to an incoming pulse if the previous analysis is still ongoing. Given that all the pulses were of the same length, the analysis duration was always the same. When the time between the incoming pulses was shorter than the time of the analysis, the pulses were not analysed. Figure 5.12 shows the sharp decline in the percentage of the analysed pulses when reaching the rate of 6 MHz. Therefore the overall analysis duration for a 10 ns pulse is approximately 200 ns.

#### 5.8.1.2 Linearity

A pulse generator was used to verify the linearity of the measurements across all input ranges. The pulse width and the amplitude were varied and measured both with the oscilloscope and the PSA to estimate the systematic error of the PSA measurements with respect to those taken by the oscilloscope. The results are shown in figures 5.13a and 5.13b. The measured amplitude error  $e_{\text{ampl}}$  is within  $\pm 3\%$  of the real value throughout the amplitude range. The width error  $e_{\text{width}}$ , however, increases significantly in the lower width range. This stems from the low bandwidth limit of the PSA, which affects the pulse shape via a slow rising and falling time, effectively smearing the pulse along the time axis. Therefore the PSA cannot measure rectangular pulses shorter than 2 ns.

#### 5.8.1.3 Stability

The input pulse signal was superimposed with the white noise generated by a CIVIDEC noise generator with a variable attenuation. The mixed signal yielded pulses with an SNR ranging from 5 (very noisy) to 100 (noise negligible). The PSA then performed the pulse parametrisation at different SNRs without changing the pulse shape. The results of the measurement errors for amplitude, width and area are shown in figures 5.14a, 5.14b and 5.14c. The amplitude is highly overestimated at a

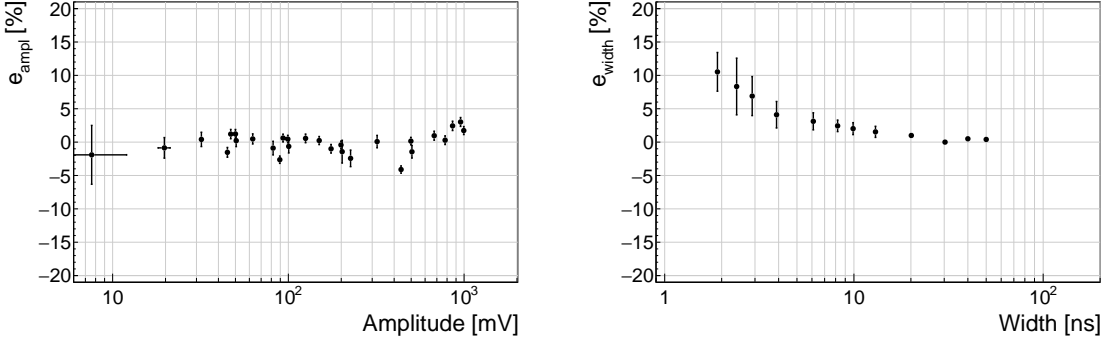


Figure 5.13: These figures show the measurement errors for amplitude (left) and width (right) across the measurement range.

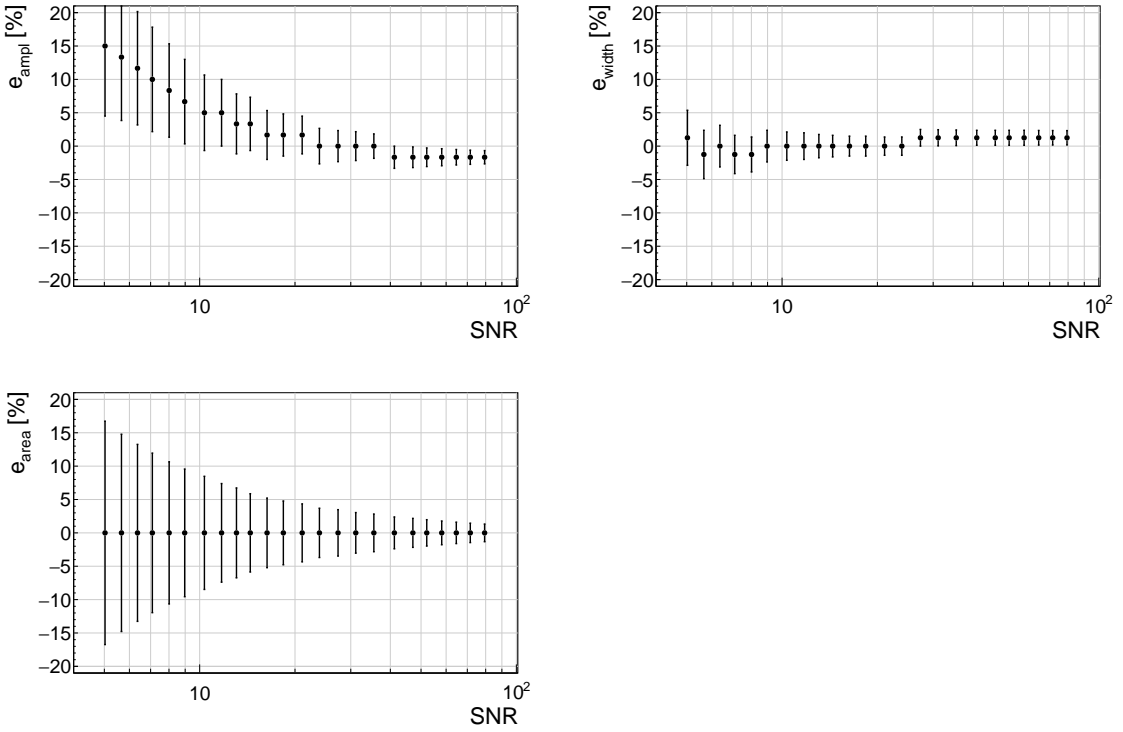


Figure 5.14: These figures show the measurements errors for amplitude (top left), width (top right) and area (bottom left) as a function of the signal-to-noise ratio.

2019 low SNR (high noise). This is because the algorithm takes the peak of the signal as the maximum  
2020 amplitude and these peaks are higher with a higher noise. Therefore the  $e_{\text{ampl}}$  is always positive  
2021 and increasing with increasing noise. The width measurement, on the other hand, is stable even for  
2022 the low SNR. The  $e_{\text{width}}$  does not exceed  $\pm 5 \%$ . Finally, the mean of the area measurement error  
2023  $e_{\text{area}}$  is always 0, but the spread of the error increases with noise. This means that the increased  
2024 noise only affects the resolution of the measured area spectrum, not its position.

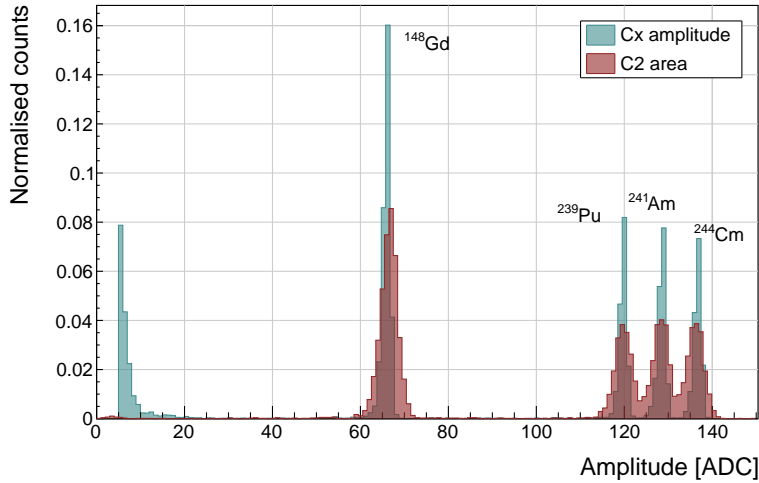


Figure 5.15: Energy spectrum of a quadruple- $\alpha$  source using a CIVIDEC Cx spectroscopic amplifier and a CIVIDEC C2 current amplifier.

#### 2025 5.8.1.4 Conclusion

2026 The results show that: 1) the amplitude, area and width measurement are linear for pulses at least  
2027 2 ns wide, 2) the highest rate of the PSA algorithm is  $\sim 6 \times 10^6$  pulses per second and 3) the lowest  
2028 SNR where the algorithm still functions is  $\sim 5$ , but the area measurement spread at that SNR is  
2029 significant.

#### 2030 5.8.2 Comparison between the charge-sensitive and current spectroscopy

2031 The calibration was done using a quadruple- $\alpha$  source containing  $^{148}\text{Gd}$ ,  $^{239}\text{Pu}$ ,  $^{241}\text{Am}$  and  $^{244}\text{Cm}$ .  
2032 Each of the radioactive elements emits  $\alpha$  particles with a specific energy: 3.2 MeV, 5.2 MeV, 5.5 MeV  
2033 and 5.8 MeV. The PSA in combination with the CIVIDEC C2 current amplifier was compared against  
2034 the 8-bit spectroscopic application in combination with the CIVIDEC Cx spectroscopy amplifier.

2035 Figure 5.15 shows the energy spectrum acquired by the two amplifiers. The  $^{241}\text{Am}$  peak measured  
2036 by the CIVIDEC Cx amplifier has an RMS of 0.8 ADC, which corresponds to a 32 keV energy  
2037 resolution. For comparison, the CIVIDEC C2 broadband current amplifier measures this peak  
2038 with an RMS of 1.9 ADC, which corresponds to a 75 keV energy resolution. Therefore the energy  
2039 spectrum measured by the current amplifier has a factor of 2.3 lower energy resolution.

## 2040 5.9 Source calibration

### 2041 5.9.1 Pulse classification

2042 Pulses induced by a specific radiation type have a specific pulse shape and therefore similar parameters.  
2043 This section outlines the parameter space for several types of radiation. Table 5.2 lists the  
2044 types of radiation and their respective pulse shapes. The types have been sorted into classes for  
2045 easier discussion. The table includes the radioactive sources that emit these particles.

*CHAPTER 5. CURRENT MONITORING  
REAL-TIME PARTICLE IDENTIFICATION*

---

Class	Particle type	Current signal	Source
2046	A	$\alpha$	Square pulse, $h^-$ drift
	B	$\alpha$	Square pulse, $e^-$ drift
	C	$\beta$	Triangular pulse
	D	$\gamma$	Triangular pulse
	E	n	Mixed pulse shapes
	F	p	Mixed pulse shapes

2047

Table 5.2: Current pulse classification.

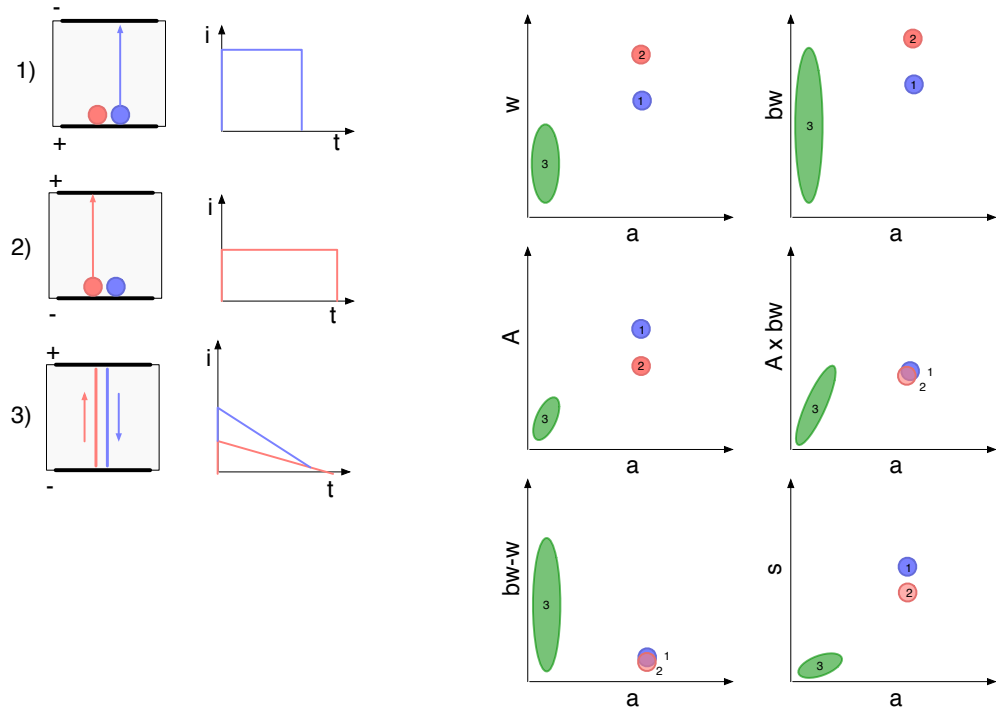


Figure 5.16: Class A, B, C, D.

2048 **5.9.1.1 Class A, B, C, D**

2049 An  $\alpha$  particle deposits all its energy at the point of entry in the sensor. Depending on the polarity  
2050 of the sensor bias voltage, either holes or electrons drift through the sensor, inducing a rectangular  
2051 current pulse.

2052 Schematic 1) in figure 5.16 shows the positive charge carriers drifting through the sensor and  
2053 the current pulse they induce – Class A. Holes produce a short and high rectangular pulse. The  
2054 parametric “fingerprint” of these current pulses is shown on the right side of figure 5.16, marked  
2055 with number 1. All  $\alpha$  particles deposit the same amount of charge. The width and the base width  
2056 are always the same as the drift velocity of the charge carriers does not change regardless of the  
2057 number of carriers drifting. The base value is slightly higher due to the rise and fall time of the  
2058 current signal. The amplitude is the same for all pulses. The same goes for the calculated area (a  
2059 product of the amplitude and base value). For an ideal pulse, the coefficient between the measured  
2060 area and the calculated area for a rectangular pulse is 1. The difference between the base width  
2061 and the width is close to 0 and depends on the rise and fall time of the current signal defined by  
2062 the electronics. The falling slope of the signal depends on the amplitude of the signal, therefore it  
2063 is constant for a nominal pulse.

2064 Schematic 2) in figure 5.16 shows the negative charge carriers drifting through the sensor and  
2065 the current pulse they induce – Class B. Electrons produce a wide and low rectangular pulse.  
2066 Parametrically Class B differs from Class A in the width, base width, amplitude and slope. The  
2067 former two are higher due to lower drift velocity of electrons. The amplitude is proportionally higher  
2068 to preserve the constant pulse area due to a constant deposited charge.

2069 Schematic 3) in figure 5.16 shows the configuration of the deposited charge created by an incident  
2070  $\beta$  particle – Class C. The positive and negative charge carriers induce a triangular pulse while drifting  
2071 to their respective electrodes. The number of electrons and holes created differs from pulse to pulse,  
2072 but follows a Landau distribution, as discussed in previous chapters. The amplitude of the pulse is  
2073 linearly dependent on the initial number of created carriers, but has a higher coefficient than that  
2074 of Class A or B. The same goes for the width and base width. The width of the pulses is lower  
2075 than that of Class A and B. The base width, however, can already be close to Class A and B for the  
2076 widest Class C pulses. The coefficient between the measured and calculated area is close to 2. The  
2077 difference between the base width and width is a wide distribution. The falling slope is a low value  
2078 for triangular pulses of all amplitudes.

2079  $\gamma$  particles interact with the diamond via Compton scattering, exciting an electron, which in  
2080 turn ionises the sensor. Therefore the predicted pulse shape – Class D – will be similar to that of  $\beta$   
2081 particles – Class C.

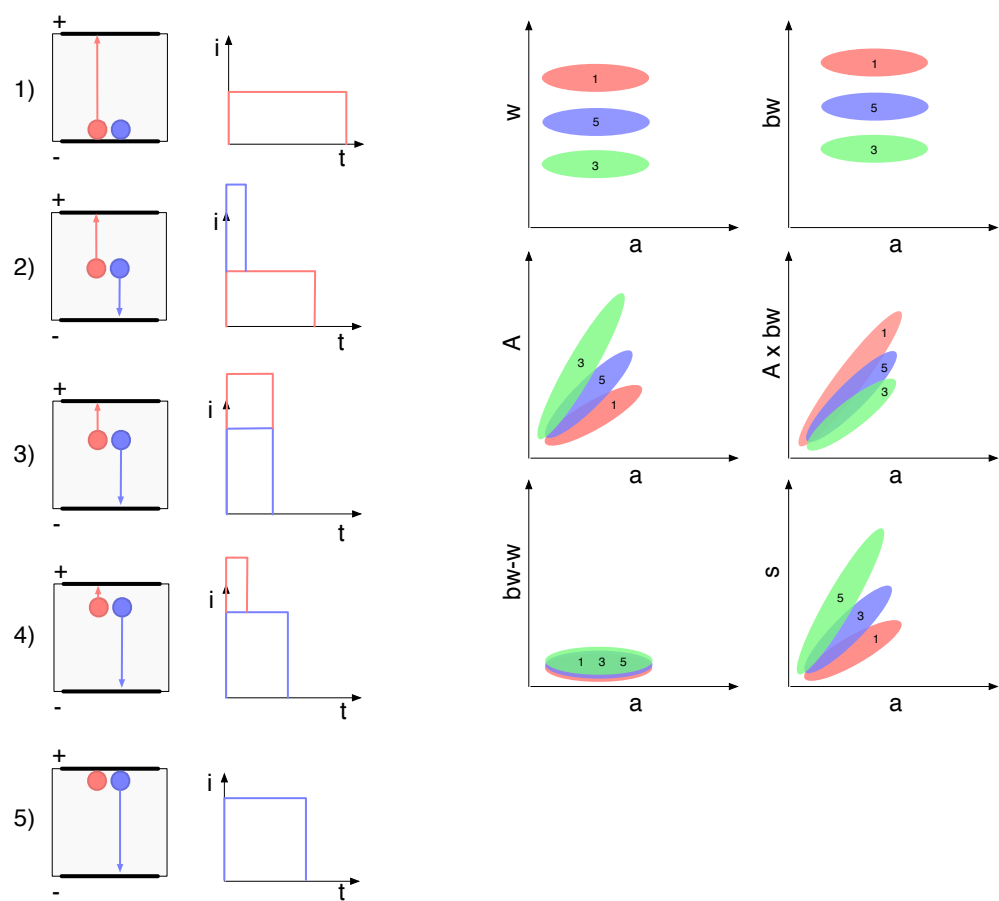


Figure 5.17: Class E.

2082 **5.9.1.2 Class E**

2083 Neutrons interact with the core of the carbon atoms, producing a range of particles ranging from  
2084  $\gamma$ ,  $\beta$  and  $\alpha$  to protons. Neutrons are therefore a source of Class A, B, C, D, E and F pulses. Class  
2085 E is a special case whereby  $\alpha$  particles are created at various points throughout the sensor. These  
2086 particles immediately deposit all their energy and the created electrons and holes that drift to their  
2087 respective electrodes induce a pulse with of a specific shape. Schematics in figure 5.17 show examples  
2088 of an  $\alpha$  creation in the sensor at five depths.

2089 Schematics 1) and 5) are equal to Class B and A type. The difference here is that the created  
2090  $\alpha$  particles have a range of energies and therefore the deposited charge has a wide range. Their  
2091 parametric fingerprint is similar to that of Class A and B, but is now spread over a wide range.  
2092 The width and base width are equal across the measured range, the same holds for the difference  
2093 between base width and width. The amplitude for both 1 and 5 increases linearly with the area.

2094 Schematic 2) shows a carrier creation in the middle of the sensor and its respective current pulse.  
2095 The holes drift faster and reach their respective electrode before the electrons reach the opposite  
2096 side. The resulting pulse has a high peak at the start where both charges contribute to the signal  
2097 and a long rectangular tail pertaining to the electron drift. Schematic 4) is similar to 2), with a  
2098 difference that in this case the electrons contribute to the initial peak. These two cases are not  
2099 shown in the parameter space.

2100 Schematic 3) shows a special case in which the created electrons and holes reach their respective  
2101 electrodes at the same time. This results in a short and high rectangular shaped current pulse. It is  
2102 narrower from 1) and 5). Its amplitude increase as a function of the area is faster than for the other  
2103 two. The same goes for the slope. Inversely, the calculated area increase as a function of the area is  
2104 slower due to a smaller base width.

2105 In summary, Class E pulses stem from neutron interactions at the electrodes or in the bulk,  
2106 forming three distinct lines.

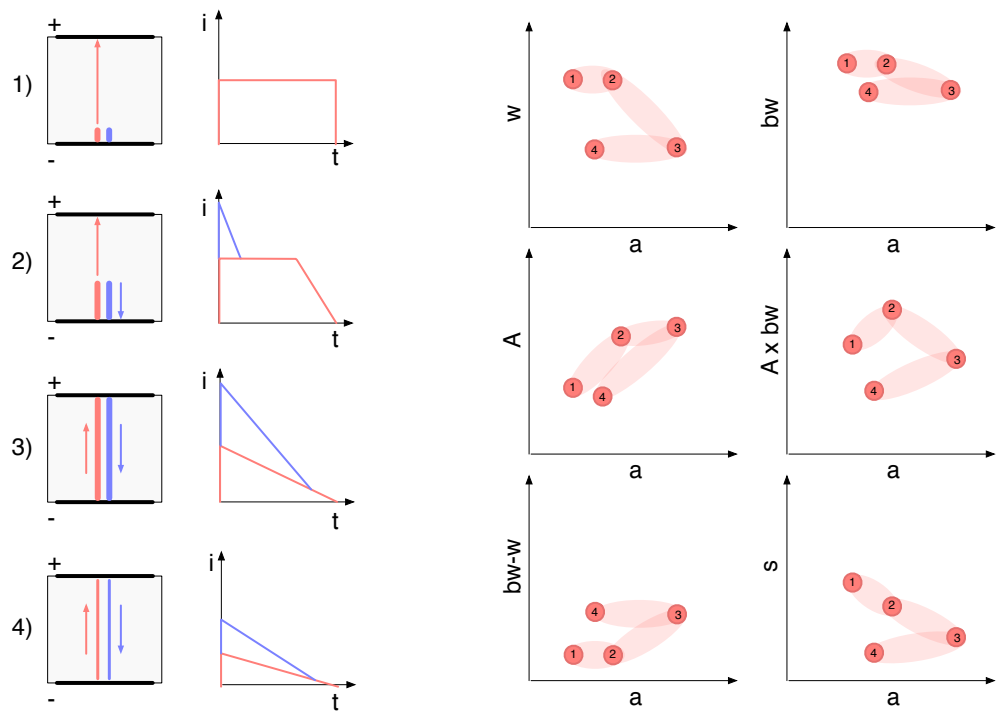


Figure 5.18: Class F.

**2107 5.9.1.3 Class F**

**2108** Protons can produce a range of pulse shapes, depending on their energy. High-energy MIPs fly  
**2109** through the sensor and produce a triangular pulse equal to that of  $\beta$ . Those with a low energy get  
**2110** stopped in the sensor, inducing a pulse with a complex shape. Class F comprises protons created  
**2111** by a neutron interaction with a carbon atom, referred to as recoil protons. For reasons of clarity  
**2112** the examples shown below stem from a neutron interaction at the negatively charged electrode. In  
**2113** addition, the direction of the recoil proton is always in the direction of the opposite electrode.

**2114** Schematic 1) shows a creation of a low-energy recoil proton. It deposits all its energy within a  
**2115** few  $\mu\text{m}$ , inducing a Class B rectangular pulse. It also resembles the Class B in the parameter space.

**2116** Schematic 2) shows a proton that travels for a third of the sensor width before being stopped.  
**2117** The trace it leaves induces a pulse with an initial peak due to the contribution of the drifting holes  
**2118** and a gentle falling edge at the end. Its width and base width are still close to the nominal value.  
**2119** The amplitude is significantly higher due to the initial peak. As a consequence, the calculated area  
**2120** is higher as well. The difference between the base width and width is still nominal. The slope value  
**2121** decreases due to a less pronounced falling edge of the pulse.

**2122** Schematic 3) shows a corner case whereby the recoil proton that is stopped at the opposite elec-  
**2123** trode. It induces a high triangular pulse. Its width is significantly lower due to the high amplitude.  
**2124** The base width, however, remains almost the same. Therefore the difference between the base width  
**2125** and width increases. The slope continues decreasing.

**2126** Schematic 4) shows a high-energy recoil proton that exits the sensor with a high velocity. Ac-  
**2127** cording to the Bethe-Bloch such a highly energetic particle deposits less charge than that with a low  
**2128** energy. The resulting current pulse therefore has a lower amplitude while preserving the width. Its  
**2129** slope is also lower due to the lower amplitude.

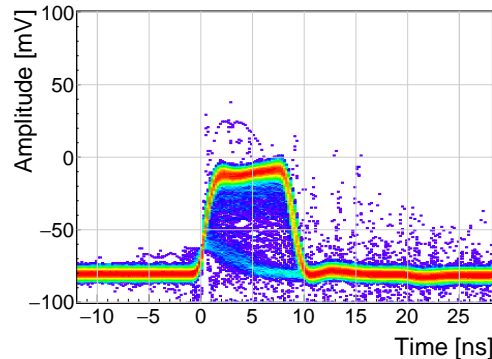
**2130 5.9.2 Data acquisition**

**2131** The operation of the pulse shape analysis has been tested using several radioactive sources. In  
**2132** particular, an  $\alpha$ , a  $\beta$  and a  $\gamma$  source have been used. Each source has been placed on top of the  
**2133** diamond detector and left for a predefined time depending on its activity. Table 2.1 shows the  
**2134** sources used, the time of exposure and their rate during data acquisition. The data for the  $\alpha$  source  
**2135** have been taken for both polarities.

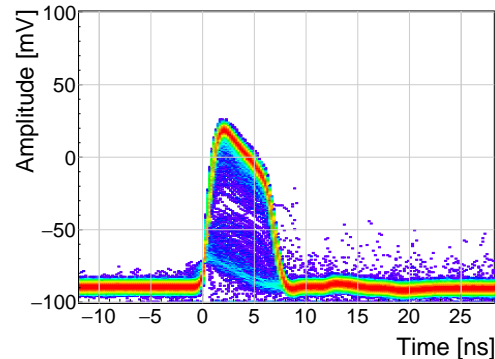
Run	Source	Radiation	Energy [MeV]	Time [h]	Triggers	Rate [ $\text{s}^{-1}$ ]	Bias [V]
1	$^{241}\text{Am}$	$\alpha$	5.5	17	10558	0.17	500
2	$^{241}\text{Am}$	$\alpha$	5.5	18	11454	0.18	-500
3	$^{90}\text{Sr}$	$\beta$	2.3	0.42	1.07e6	1'000	500
4	$^{60}\text{Co}$	$\gamma$	1.3	0.28	1.34e6	3'300	500
5	$^{239}\text{Pu Be}$	$n$	1-10	2.5	1.5e6	230	500

**2137**

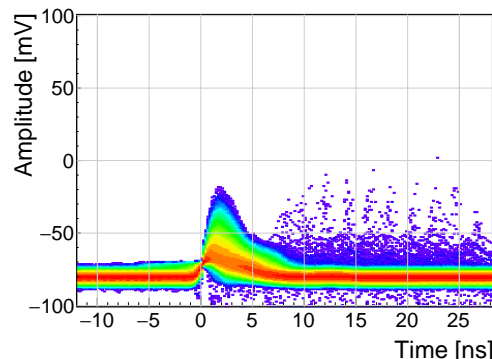
Table 5.3: Measurements carried out at Atominstutitut.



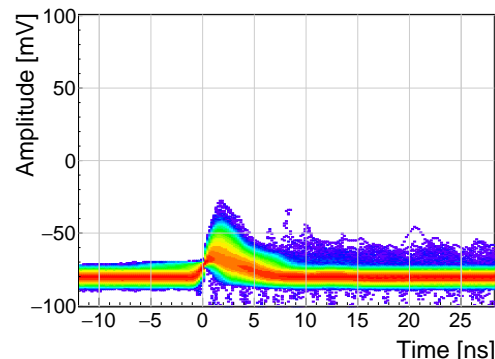
(a)  $^{241}\text{Am}$ ,  $e^-$  collection.



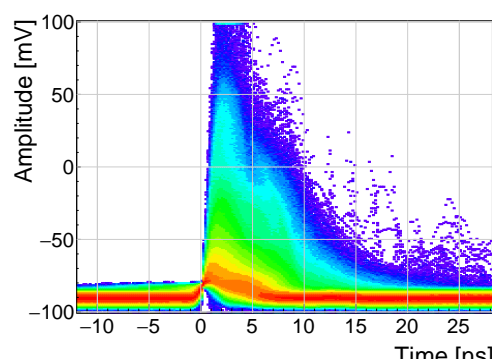
(b)  $^{241}\text{Am}$ ,  $h^+$  collection.



(c)  $^{90}\text{Sr}$ .



(d)  $^{60}\text{Co}$ .



(e)  $^{239}\text{Pu}$  Be.

Figure 5.19: Accumulated current pulses for all runs.

Figure 5.19a shows a set of current pulses induced by the  $\alpha$  particles whereby only the electrons drift through the sensor. The great majority of particles creates a defined number of charge carriers. According to the FWHM of the pulse, the electrons drift for 9 ns before reaching the opposite electrode. The pulse amplitude is stable during the drift, with a gentle positive inclination. This hint on a weak negative space-charge built up across the sensor. Some pulses have a lower amplitude while retaining the width; the smaller pulse area means that there are fewer drifting charge carriers than a nominal value. This shows that some incident  $\alpha$  already lose a part of their energy while traveling through the air before hitting the sensor. Furthermore, there is a number of low-amplitude triangular pulses which are created by incident  $\gamma$  particles. Finally, the scarce entries above the baseline after the pulse stem from interference pulses.

Figure 5.19b also shows the  $\alpha$ -induced current signals, but for the hole collection. The number of holes created is equal to the number of created electrons, therefore the collected charge is the same for both. This means that the area of the current pulse is equal to that in figure 5.19a. The pulses are only 6 ns wide, which confirms that hole mobility in diamond is  $\sim 30\%$  higher than that of electrons at room temperature. Therefore the current pulse must be higher to preserve the area. The pulses have a steep negative droop. This is due to a strong negative space-charge built up during preceding measurements with a neutron source. Furthermore, some pulses induced by a lower energy  $\alpha$  have a lower amplitude and hence a lower pulse area. Finally, the  $\gamma$ -created triangular pulses are still present.

Figure 5.19c shows the triangular pulses created by the incident  $\beta$  particles. Most have a low amplitude that is close to the trigger threshold (red coloured line). Those below the threshold are not visible by the PSA. The entries behind the pulses are either interference pulses or  $\beta$  pulses following the first pulse.

Figure 5.19d shows the triangular pulses created by the incident  $\gamma$  particles. The distribution is very similar to that created by the incident electrons in figure 5.19c. This is expected –  $\gamma$  particles interact with the sensor via compton scattering, freeing an electron which in turn ionises the sensor. Therefore the resulting current pulses of an incident  $\gamma$  are similar to those of an incident  $\beta$ .

Figure 5.19e shows that the neutron source causes the widest variety of pulse shapes - triangular and rectangular as well as those in between. This stems from the various interactions of neutron with carbon atoms, whereby  $\alpha$ ,  $\beta$ ,  $\gamma$  or protons can be produced. The prevailing pulses are still those created by  $\gamma$ . Pulse shapes caused by neutrons are described in detail in [80, 81].

### 5.9.3 Scatter plots

An online pulse shape analysis has been run on all the aforementioned data sets. The parameters of the pulses are plotted in 2D histograms - in form of scatter plots. The aim is to find a way to distinguish between the various types of radiation in order to only select the spectrum of a single type of particles from a spectrum of a mixed source. The energy spectrum is directly proportional to the measured area of the current pulses, therefore all the parameters are plotted as a function of the pulse area.

Every individual parameter can be attributed a set of qualifiers with which a certain part of the distribution can be rejected. There are two ways to apply the qualifiers. One is to set the minimum and maximum value for a specific parameter. The accepted pulses are those in between these two values. The minimum and the maximum qualifier are marked with a blue and a red line in the subsequent scatter plots. The second way is to apply a linear cut to the distribution in the scatter plot. The user can choose the slope of the line and to accept either the pulses above or below the line. The colour of the line is blue if the part above the line is accepted and red if opposite. Currently two

## 5.9. SOURCE CALIBRATION

---

2183 scatter plots have this option implemented: area vs amplitude and area vs amplitude×base width.  
2184 The latter represents the Form Factor, which is discussed in section 5.6.2.

2185 The sets of plots in figures 5.22, 5.20, 5.24 and 5.26 show the above listed parameters plotted  
2186 as a function of the pulse area for  $^{241}\text{Am}$  (electrons and holes),  $^{90}\text{Sr}$  and  $^{60}\text{Co}$  source, respectively.  
2187 Any distinguishable difference between the plots of two sources would suggest that that particular  
2188 parameter can be used to distinguish one type radiation from the other. For the most part the  
2189  $\gamma$  are considered the rejected pulses (greyscale colour palette) whereas  $\alpha$  particles or neutrons are  
2190 accepted (yellow colour palette). In special cases only a certain types of neutron interactions are  
2191 accepted, as depicted in section 5.10.

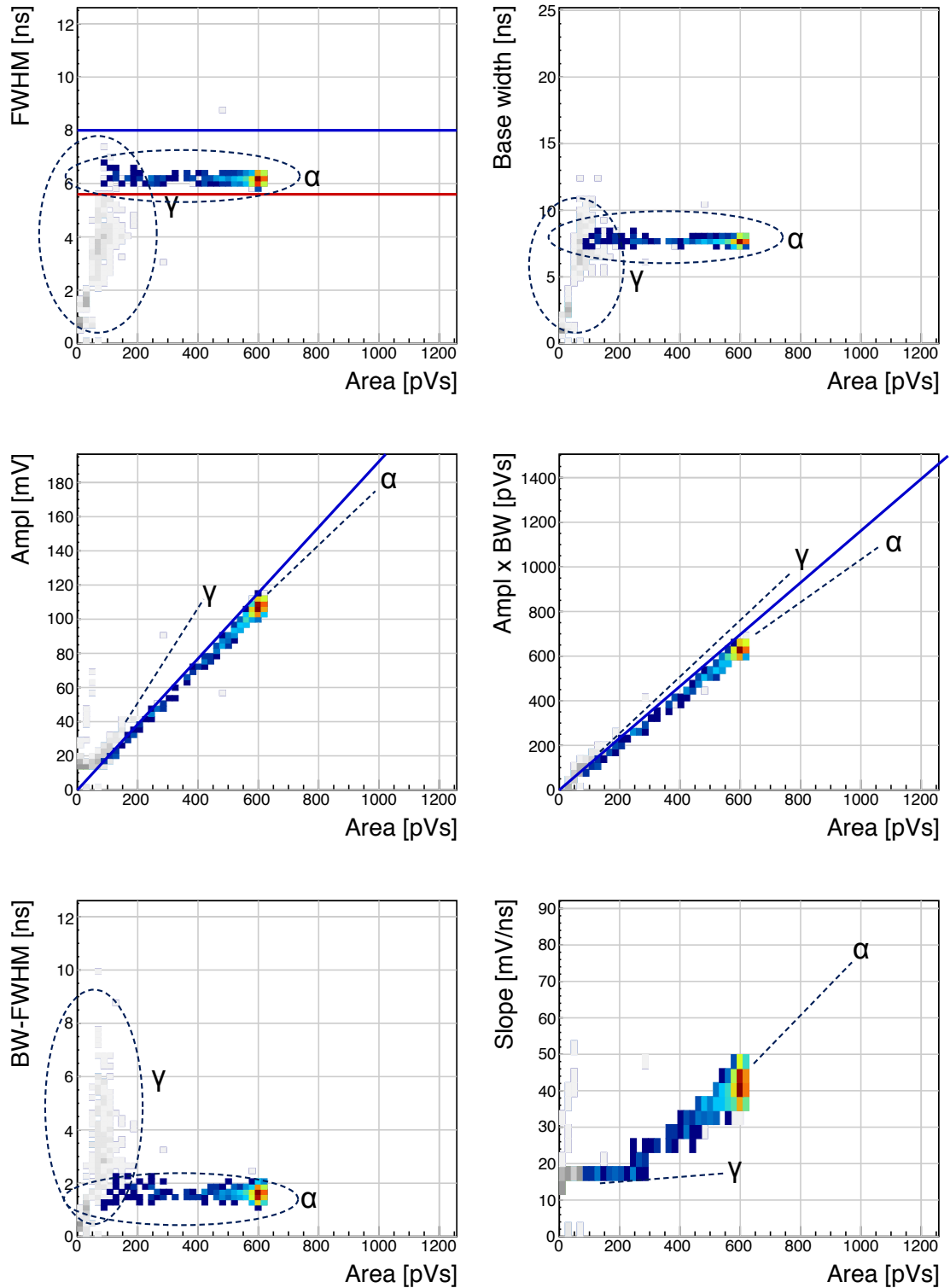


Figure 5.20:  $^{241}\text{Am}$ ,  $\text{h}^+$  collection. Qualifier: FWHM.

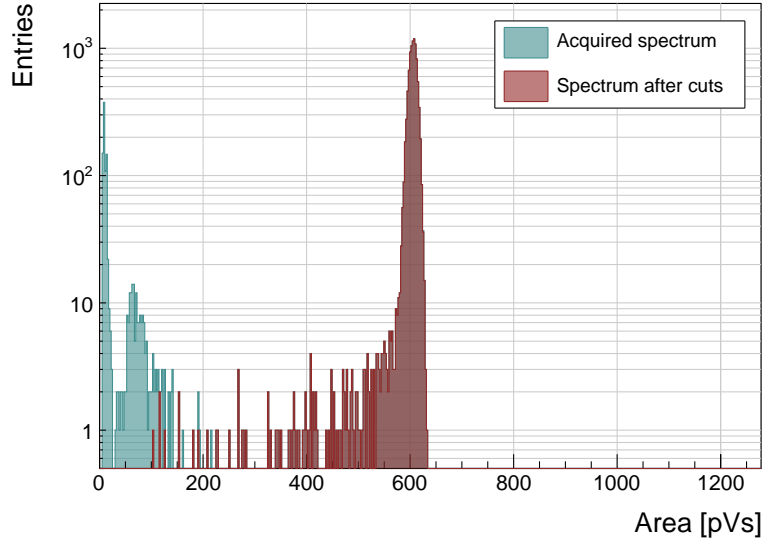


Figure 5.21:  $^{241}\text{Am}$  area histograms for hole collection. The green histogram represents all collected data whereas the red one marks the data whereby the pulse parameters are within the qualifiers. The  $\alpha$  peak at 600 pVs is clearly visible, followed by a  $\gamma$  quasi-Landau distribution with an MPV of  $\sim 70$  pVs and a noise peak at the very left of the area distribution. These two contributions have been rejected by the qualifiers.

**5.9.3.1  $^{241}\text{Am}$  source,  $\text{h}^+$  collection**

The source emits  $\alpha$  particles at  $\sim 5.5$  MeV and 60 keV  $\gamma$  photons. Due to the losses in the air and in the electrode the measured  $\alpha$  energy varies – between  $\sim 5$  MeV down to 1 MeV. Figure 5.20 shows the parameter space of the acquired data for hole collection - Class 1. Width, amplitude and calculated area qualifiers have been used to identify the  $\alpha$  pulses and reject the  $\gamma$ . Figure 5.21 shows a one-dimensional area distribution of the acquired data.

**Width:** A distinct horizontal line at 6.5 ns starting from 100 and peaking at 600 pVs shows the aforementioned spread of  $\alpha$  energies. The width of the pulse remains constant.  $\gamma$  cluster overlaps with the  $\alpha$  cluster at low energies. Width qualifier is used.

**Base width:** Wider than the FWHM, yet still constant over the entire range. High overlap with  $\gamma$ .

**Amplitude:** Linear increase with area. The coefficient for  $\alpha$  pulses is lower than that for  $\gamma$ . Amplitude qualifier is used.

**Calculated area:** Barely distinguishable difference in slope coefficients for  $\alpha$  and  $\gamma$ . Calculated area qualifier is used.

**Base width – width:** Minimal difference for  $\alpha$ , high spread for  $\gamma$  as expected. At low  $\gamma$  area the overlap is high, so the qualifier cannot be used.

**Slope:** Linear increase with the area. Significant overlap in the low area range. A line of entries with a high slope at low area pertains to short noise pulses with a high spike.

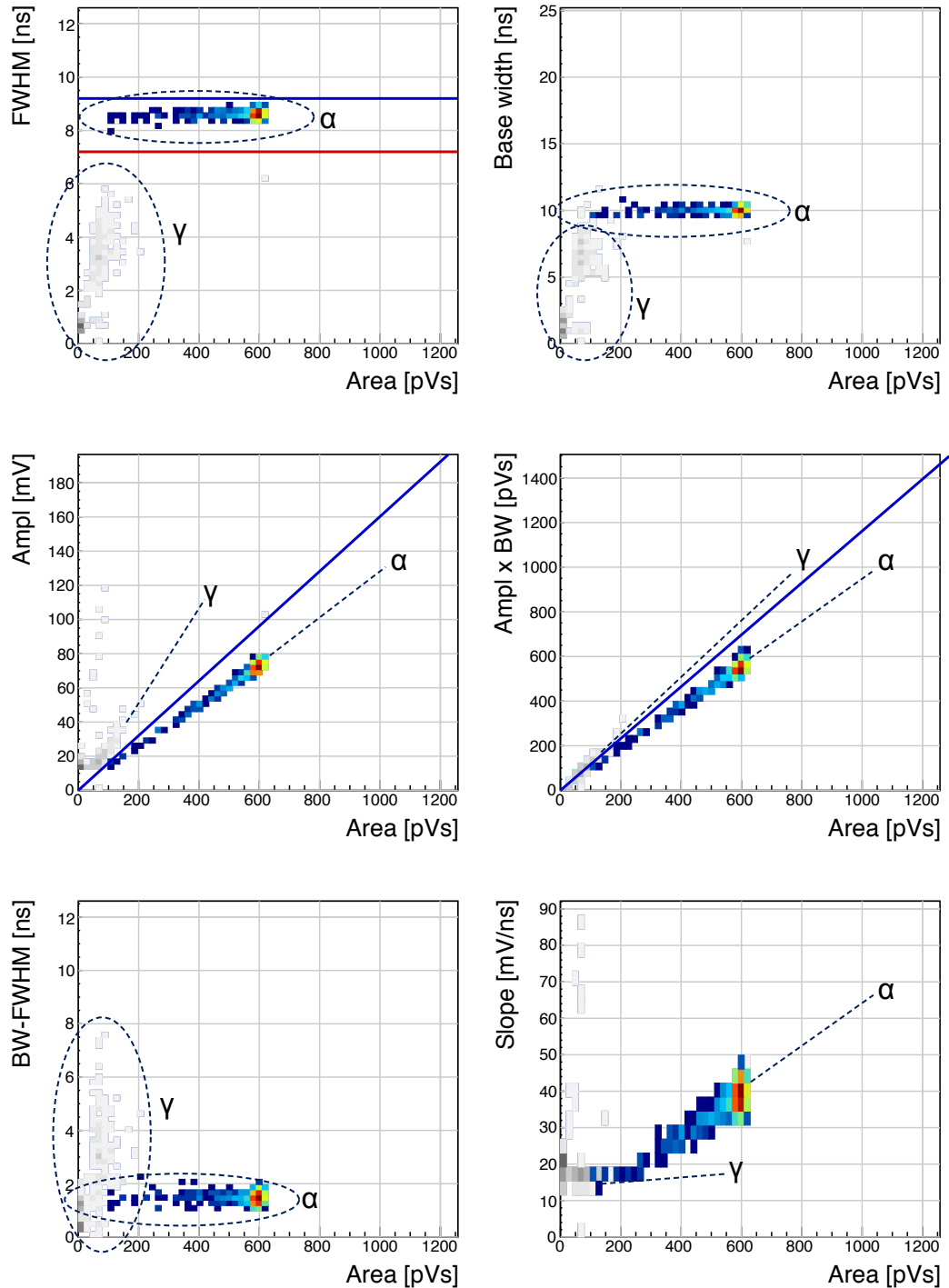


Figure 5.22:  $^{241}\text{Am}$ ,  $e^-$  collection. Qualifier: FWHM. Optional qualifiers: Amplitude, Form Factor.

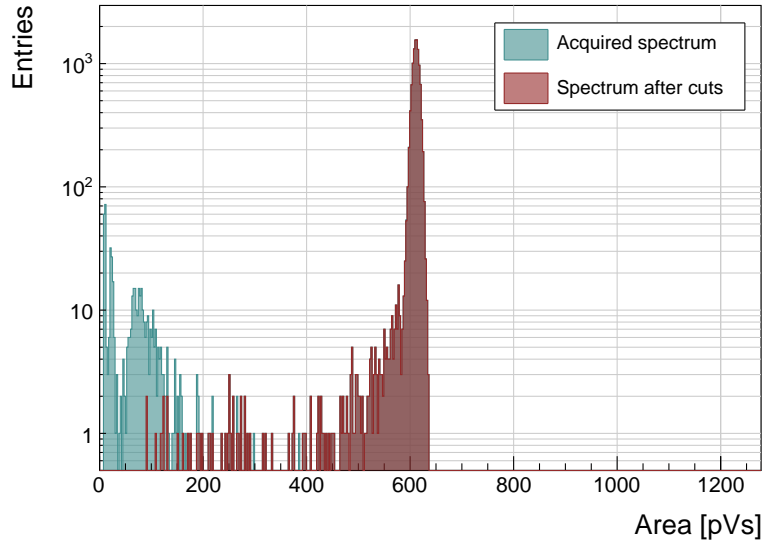


Figure 5.23:  $^{241}\text{Am}$  area histograms for electron collection. The green histogram represents all collected data whereas the red one marks the data whereby the pulse parameters are within the qualifiers. The  $\alpha$  peak at 600 pVs is clearly visible, followed by a  $\gamma$  quasi-Landau distribution with an MPV of  $\sim 70$  pVs and a noise peak at the very left of the area distribution. These two contributions have been rejected by the qualifiers.

**5.9.3.2  $^{241}\text{Am}$  source,  $e^-$  collection**

Figure 5.22 shows the parameter space of the acquired data for electron collection - Class 2. Width, amplitude and calculated area qualifiers have been used to identify the  $\alpha$  pulses and reject the  $\gamma$ . Figure 5.23 shows a one-dimensional area distribution of the acquired data.

**Width:** A distinct horizontal line at 8.5 ns starting from 100 and peaking at 600 pVs shows the spread of  $\alpha$  energies. The width of the pulse remains constant.  $\gamma$  cluster does not overlap with the  $\alpha$  cluster at low energies as none of the  $\gamma$  pulses are as wide as the  $\alpha$ . Width qualifier is used.

**Base width:** Wider than the FWHM, yet still constant over the entire range. Small overlap with  $\gamma$ .

**Amplitude:** Linear increase with area. The coefficient for  $\alpha$  pulses is significantly lower than that for  $\gamma$ , also lower than that for hole collection. Amplitude qualifier is used.

**Calculated area:** Distinguishable difference in slope coefficients for  $\alpha$  and  $\gamma$ . Calculated area qualifier is used.

**Base width – width:** Minimal difference for  $\alpha$ , high spread for  $\gamma$  as expected. At low  $\gamma$  area the overlap is low, but due to low statistics.

**Slope:** Linear increase with the area. Overlap in the low area range. A line of entries with a high slope at low area pertains to short noise pulses with a high spike.

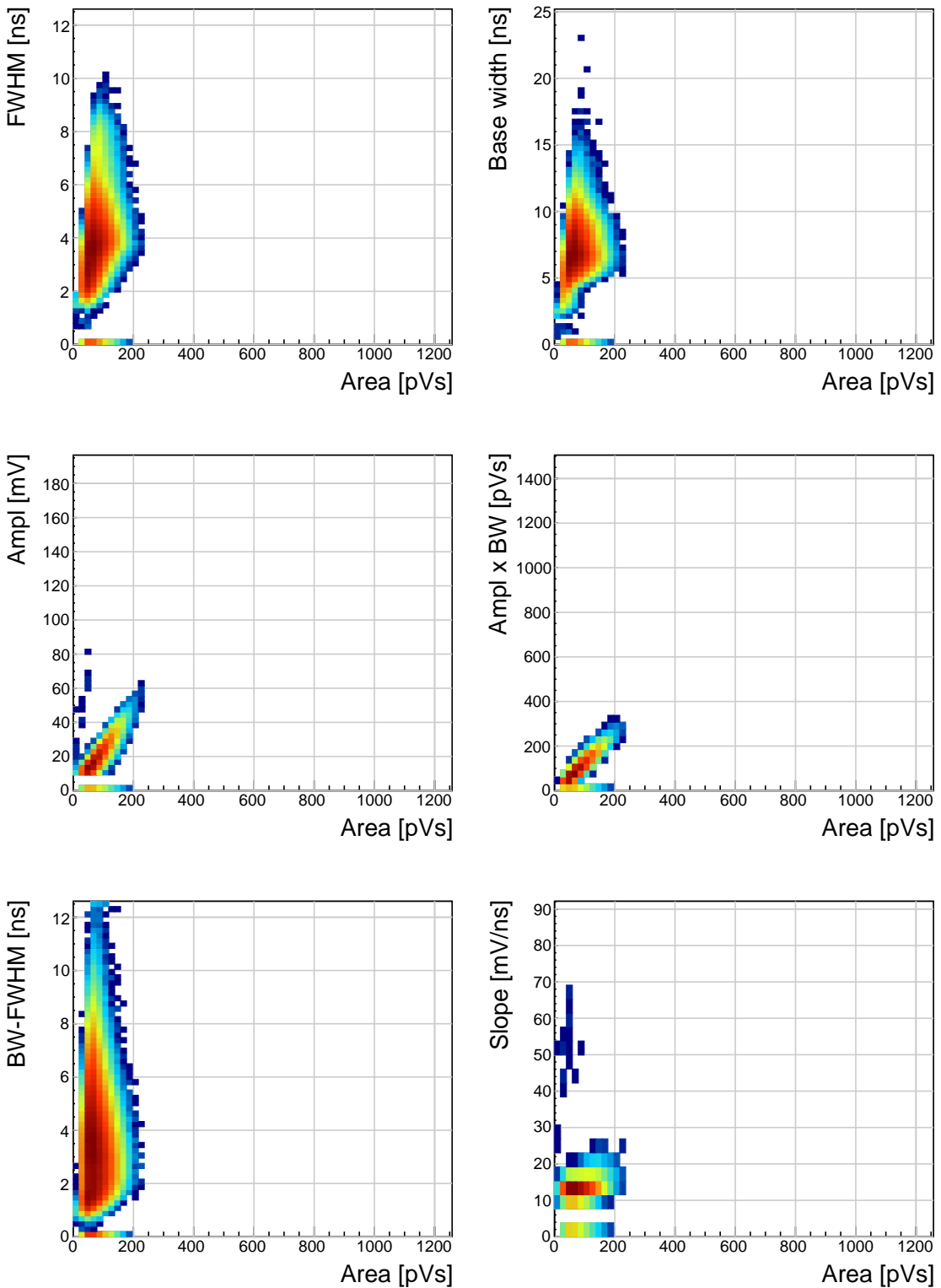


Figure 5.24:  $^{90}\text{Sr}$  scatter plots.

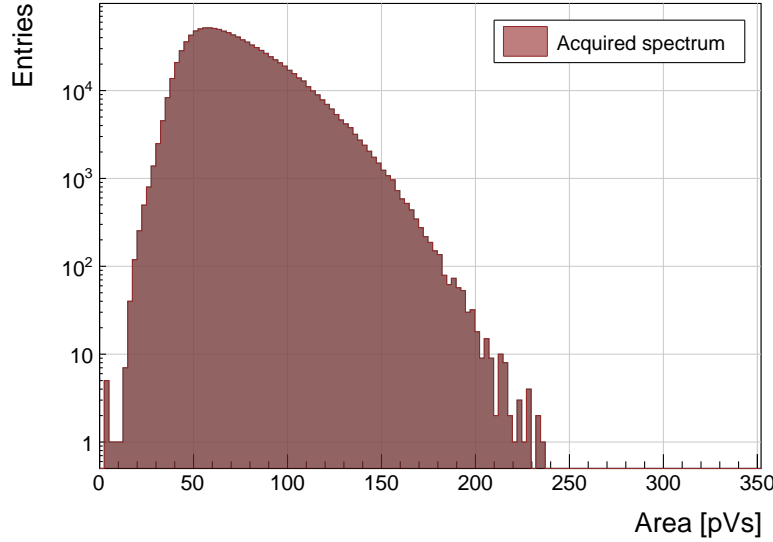


Figure 5.25: Area histogram for  $\beta$  particles. Relative to the 600 pVs  $\alpha$  peak, the expected MPV of a  $\beta$  MIP is  $\sim 30$  pVs, which is not the case in these distributions (peaking at 60 pVs). This is because the PSA device is a self-triggering system, which cuts the lower energetic particles with the trigger threshold. The resulting distribution is therefore only the top part of the real Landau distribution. This is a limitation of the device, governed by the analog noise of the current pre-amplifier.

2228 **5.9.3.3  $^{90}\text{Sr}$  source**

2229 Figure 5.24 shows the parameter space of the acquired data for  $\beta$  particles - Class 3. Figure 5.25  
2230 shows a one-dimensional area distribution of the acquired data.

2231 **Width:** The width of the  $\beta$  cluster is spread over a wide range and is not linearly dependent on  
2232 the area. This implies that the pulse shapes are not necessarily triangular but have varying shapes.

2233 **Base width:** Wider than the FWHM with a similar distribution.

2234 **Amplitude:** Linear increase with the area. A line of entries with a high slope at low area pertains  
2235 to short noise pulses with a high spike.

2236 **Calculated area:** Linear increase with area.

2237 **Base width – width:** A wide spread of entries.

2238 **Slope:** A gentle linear increase with the area. A line of entries with a high slope at low area  
2239 pertains to short noise pulses with a high spike.

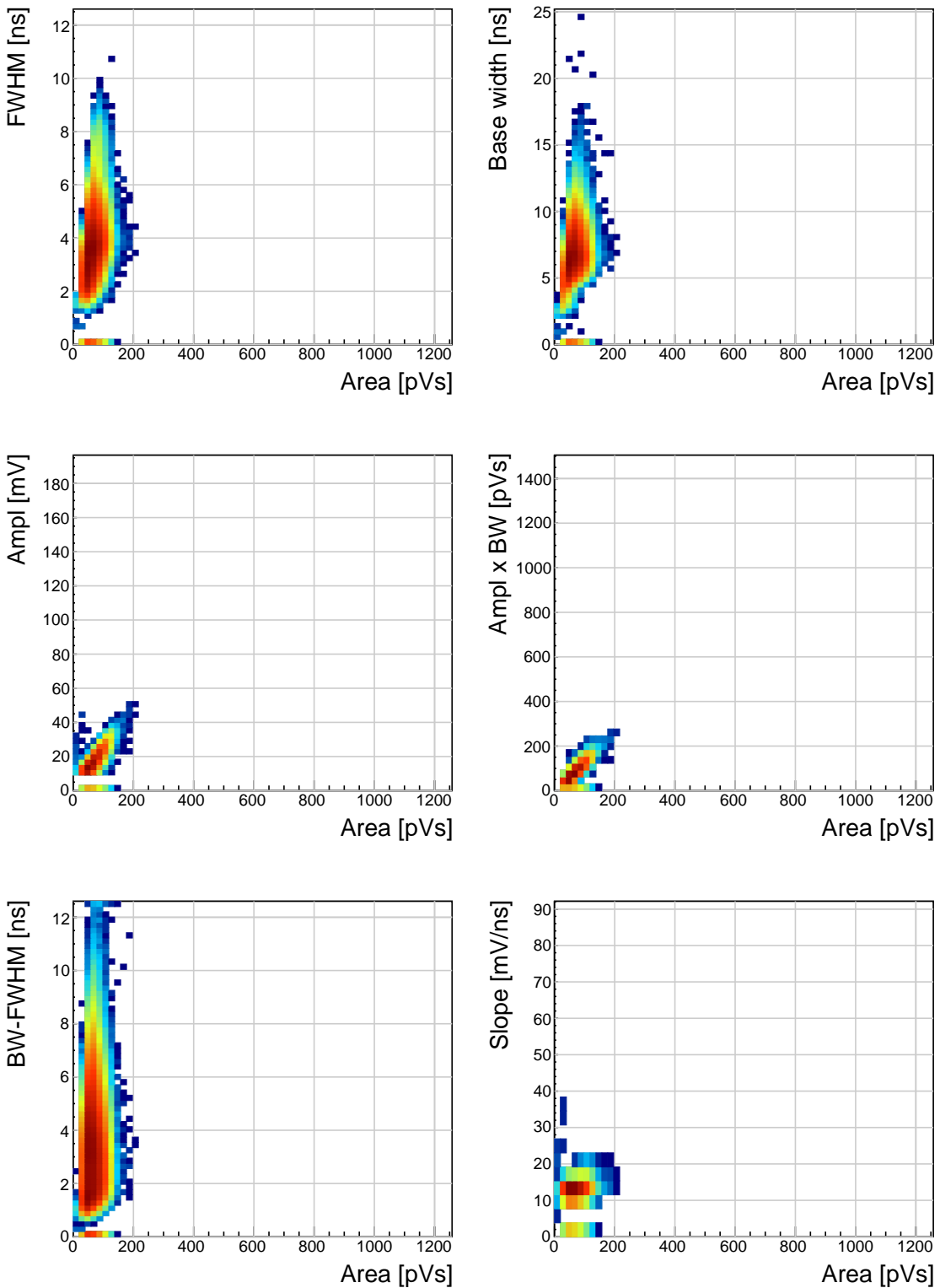


Figure 5.26:  $^{60}\text{Co}$  scatter plots.

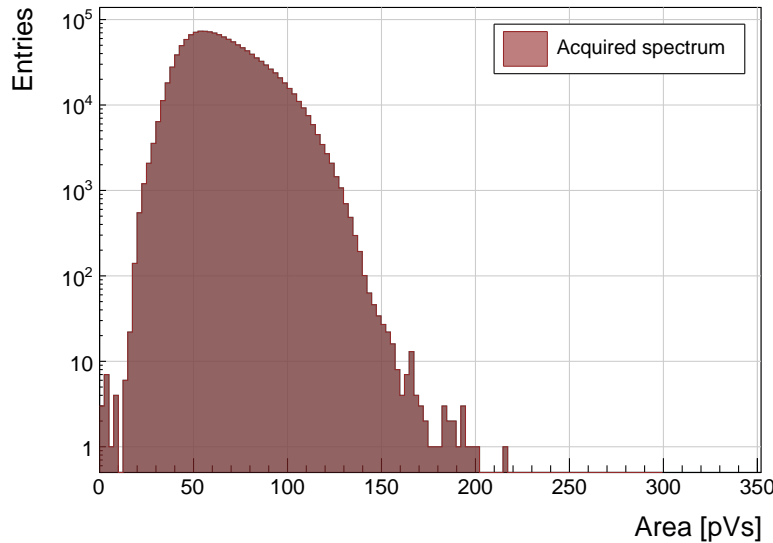


Figure 5.27: Area distribution of  $\gamma$  particles. Relative to the 600 pVs  $\alpha$  peak, the expected MPV of a  $\beta$  MIP is  $\sim 30$  pVs, which is not the case in these distributions (peaking at 60 pVs).

2240 **5.9.3.4  $^{60}\text{Co}$  source**

2241 The parameter space of the  $^{60}\text{Co}$  source overlaps entirely with that of the  $^{90}\text{Sr}$  source. This renders  
2242 it virtually impossible to distinguish between  $\gamma$  and  $\beta$  particles. Comparing the width of the  $\gamma$  and  
2243  $\beta$  and the high reach of the former, the electron collection of the alphas would need to be used to  
2244 effectively discriminate between the two types of particles.

2245 The one-dimensional histogram in figure 5.27 shows a quasi-Landau distribution with the MPV  
2246 at  $\sim 60$  pVs, which is in agreement with the background  $\gamma$  radiation emitted by the  $^{241}\text{Am}$  source,  
2247 as shown in figure 5.23 in the previous subsection. This is again not a pure Landau distribution  
2248 – the real MPV should be peaking at 30 pVs, with a minimum expected area of 20 pVs at 2/3 of  
2249 the MPV. This is not possible to measure due to the high electronics noise of the amplifier and  
2250 consequently a high trigger threshold to avoid noise triggers.

## 2251 5.10 Applications in neutron instrumentation

2252 The real-time pulse shape analysis procedure can be applied to more complex systems. This section  
2253 includes three applications where the PSA has been applied.

2254 Semiconductor-based neutron detectors provide a compact technology for neutron detection.  
2255 However, the cross section of a neutron with diamond is very low, since it only interacts with the  
2256 core of the atoms. Diamond is mainly used to detect charged particles.

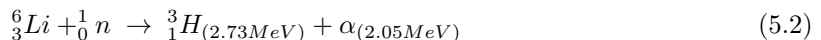
2257 Research neutron reactors radiate a mix of particles, apart from neutrons also  $\gamma$ , which are  
2258 considered a background radiation, which conceals the neutron spectrum. When measured with  
2259 diamond, the signal from neutrons is difficult to distinguish from the photon spectrum. In addition,  
2260 low energy neutrons do not cause nuclear reactions in the bulk. All in all, the neutron measurements  
2261 in a reactor using a diamond sensor present a challenge. However, by means of the PSA, the neutron  
2262 signal can be discriminated from the photon background to some extent. The following examples  
2263 show how measurements of fast ( $n^+$ ) and thermal ( $n^-$ ) neutrons have been carried out by means of  
2264 the PSA.

2265 Note the changing scale on the  $x$  axis in the figures.

### 2266 5.10.1 Thermal neutron flux monitoring

2267 Research neutron reactors like TRIGA MARK II [8] at Atominstitut [7] in Vienna are capable of  
2268 emitting neutrons at a wide range of energies. The neutron flux is proportional to the current power  
2269 of the reactor. It is therefore instrumental to monitor the neutron flux to make sure that the reactor  
2270 operation is within the specified limits. However, the byproduct of the radioactive decays in the core  
2271 is  $\gamma$  radiation, which has an energy range that overlaps with that of neutrons, making it difficult to  
2272 measure the neutron flux. This is where PSA and diamond detectors come into play. This section  
2273 describes the application of thermal neutron flux monitoring by means of the PSA.

2274 Thermal neutrons do not interact with the diamond bulk due to their low kinetic energy (of the  
2275 order of 0.012 eV). Hence a converter foil has to be added to produce second order effects. Incoming  
2276 neutrons interact with the foil, producing a set of secondary particles. These can then be detected  
2277 upon hitting the detector bulk. Common neutron interactions that are used in thermal neutron  
2278 detection are  $^{10}\text{B}(n,\alpha)^7\text{Li}$  reaction and  $^6\text{Li}(n,\alpha)^3\text{H}$  reaction ( $\alpha$  stands for  $^4_2\text{He}$ , see equation 5.2).  
2279 The focus in this section is on the latter. With a foil installed, there are several possibilities for  
2280 neutrons to interact with the detector system. Each of these interactions ionises the diamond bulk  
2281 in its own way, resulting in a specific shape of the current pulse. A neutron can: 1) interact with  
2282 the foil, producing an  $\alpha$  and a  $^3\text{H}$ , 2) interact with a carbon atom in the lattice, producing an  $\alpha$   
2283 and a  $\gamma$  or even three  $\alpha$ . The thermal neutrons do not have enough kinetic energy to interact with  
2284 the lattice, therefore the focus is on case (1). The equation for this reaction is the following:



2285 The particles in the first case are produced outside the diamond and get stopped immediately upon  
2286 hitting the sensor. The resulting pulses for both particles have a rectangular shape of the same  
2287 width, because the carriers drift with the same speed in both cases. The difference is in the number  
2288 of free carriers produced - the tritium creates more (proportional to the deposited energy), which in  
2289 turn induces a higher pulse.

2290 TRIGA MARK II neutron reactor emits large amounts of  $\gamma$  radiation in the energy range up  
2291 to 3 MeV. This already affects the measurements of  $\alpha$  particles, the energy of which peaks at 2.05  
2292 MeV in the case of  $^6\text{Li}$  converter foil. However,  $\gamma$  background radiation can be suppressed by

discriminating current pulses of  $\gamma$  from those induced by  $\alpha$  particles. This idea has already been implemented in offline analysis in [78, 79]. The results show that the background  $\gamma$  can be subtracted successfully. In order to make sure that every single incident thermal neutron has been accounted for, the algorithm has been ported to FPGA where it detects and analyses particles in real time.

**5.10.1.1 Measurements**

ROSY readout device with the implemented Pulse Shape Analysis was put to a test at Atominstitut in Vienna. Their TRIGA neutron reactor is capable of delivering thermal neutrons with the energy 0.012 eV at a rate of  $10^3$  n cm $^{-2}$  s $^{-1}$ , with a considerable  $\gamma$  background.

First, the device was calibrated using an unsealed monochromatic  $^{241}\text{Am}$  source with the emitted particle energy  $E_\alpha = 5.1$  MeV (taking into account the losses in the air). Then the diamond detector was exposed to the beam. Secondary reaction products ( $\alpha$  and  $^3\text{H}$  particles), created by neutrons hitting the converter foil, were detected by the diamond sensor, together with a significant photon background. Then the pulse identification algorithm was applied to discriminate between the reaction products and the  $\gamma$ .

The main parts of the detector are an sCVD diamond sensor sized 4.7 cm  $\times$  4.7 cm and a 1.8  $\mu\text{m}$  thick  $^6\text{LiF}$  converter foil, both embedded in an RF-tight PCB. The diamond sensor is biased with a bias voltage of 1 V/ $\mu\text{m}$  and capacitively coupled to CIVIDEC's C2 40 dB wide bandwidth current preamplifier. A 5 m long BNC cable connects the preamplifier to CIVIDEC ROSY box. The detector assembly together with the preamplifier has to be placed in front of an exit hole of the reactor.

Note: this data set has been taken with an older version of the firmware, which only measured a limited number of pulse parameters.

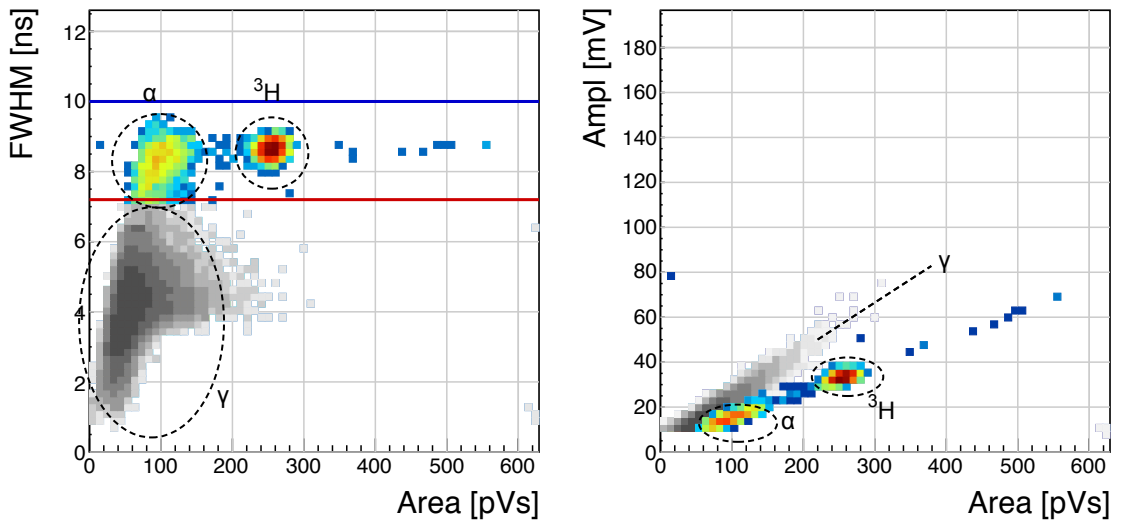


Figure 5.28: Thermal neutrons,  $\gamma$ . Qualifier: FWHM.

### 2314 5.10.1.2 Results and discussion

2315 The data shown in figure 5.28 show a high flux of  $\gamma$ , which covers a wide area range.

2316 **Width** The  ${}^3\text{He}$  peak is clearly visible in the top left plot and has almost no overlap with the  $\gamma$  2317 cluster. The  $\alpha$  cluster has a much lower energy and is in the same energy range as the  $\gamma$ . However, 2318 its width is higher and makes a separation between the  $\gamma$  and the  $\alpha$ . By setting a qualifier to the 2319 right value, the photon background is cut away, leaving only the thermal neutron decay products in 2320 the data set.

2321 **Amplitude** A clear difference between the linear coefficients is seen. However, at low area values 2322 the  $\alpha$  peak is already hidden by the  $\gamma$ , which makes the amplitude qualifier insufficient.

2323 The resulting one-dimensional area histogram before and after applied cuts is shown in figure 5.29. 2324 The blue distribution is the mixed field of background  $\gamma$ , tritium and  $\alpha$  particles. The latter are 2325 completely hidden in the  $\gamma$  energy distribution. After applied qualifiers the  $\alpha$  peak appears. There 2326 are 2422 and 1174 entries in the respective peaks, pointing to a  $\sim$ 50 % detection efficiency of  $\alpha$  2327 particles. This loss is mostly due to energy losses in the air, which yields rectangular pulses with a 2328 low amplitude. The mean values are at 260 pVs and 100 pVs, which correspond to 2.1 MeV and 2329 0.8 MeV.  $\alpha$  therefore loses 60 % of its energy whereas tritium only loses 22 %.

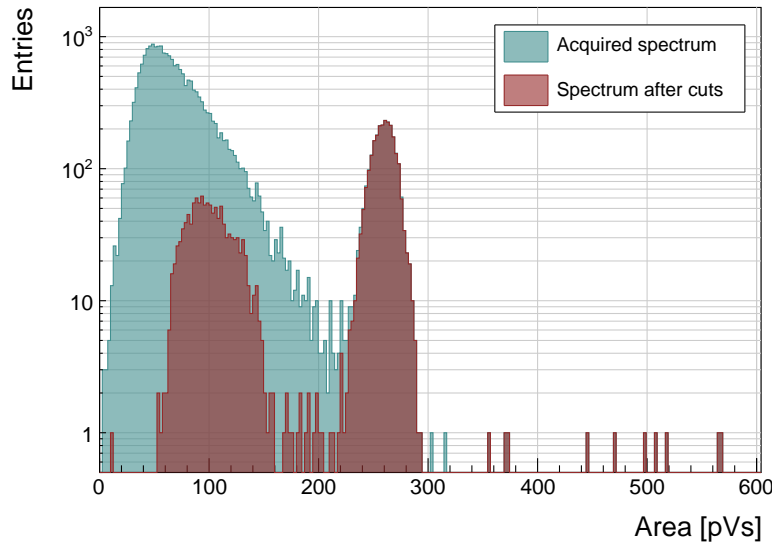


Figure 5.29: Energy spectrum after applied qualifiers reveals the tritium and the  $\alpha$  peak.

2330 To sum up, by applying the FWHM qualifier to the acquired data from the TRIGA neutron  
2331 reactor, the  $\alpha$  and tritium particles can be identified and separated from the  $\gamma$  background. The  
2332 resulting cleaned data can be used to correctly count the thermal neutrons detected by the diamond  
2333 sensor. The 50 % detection efficiency of  $\alpha$  particles can be improved by minimising the distance  
2334 between the  ${}^6\text{LiF}$  foil and sensor, thus minimising the energy loss in the air.

### 2335 5.10.2 Fusion power monitoring

2336 Many research collaborations around the world are trying to develop a functional fusion reactor,  
2337 which could provide a cleaner energy source. One of them is ITER [82], a research fusion reactor  
2338 being built in France. The idea behind it is to harvest energy from the fusion of light atoms into  
2339 a heavier one. For ITER the fuel chosen is a mixture of deuterium and tritium, which fuse into  
2340 a helium atom at extremely high temperatures (plasma), emitting a highly energetic neutron as a  
2341 byproduct. The equation is the following:



2342 The  $\alpha$  particle immediately deposits its energy within the plasma. The neutron, due to its neutral  
2343 charge, continues its way out of the system where it is stopped. The stopping power is converted into  
2344 energy, which heats the water into steam, which in turn spins the turbines, generating electricity.

2345 It is possible to monitor the activity of the reactor by measuring the flux of neutrons emitted.  
2346 Neutron diagnostics such as neutron cameras, neutron spectrometers and neutron flux monitors  
2347 therefore provide robust measurements of fusion power. A high  $\gamma$  background makes it difficult to  
2348 accurately measure the neutron flux. This is a motivation to use a diamond based detector with a  
2349 real-time PSA algorithm.

2350 The neutrons emitted are 14 MeV mono-energetic fast neutrons. The most accurate and efficient  
2351 way to detect them with a diamond detector is by means of a  $C_{12}(n,\alpha)$  reaction with a carbon atom  
2352 in the ballistic centre [83]. In this region the positive and negative charge carriers created by  $\alpha$  that  
2353 start drifting in the opposite directions need the same time to reach the opposite electrodes.

#### 2354 5.10.2.1 Measurements

2355 The  ${}^{239}\text{Pu Be}$  neutron source has been used to simulate the fusion reactor. It emits a mixed field  
2356 of neutrons and  $\gamma$  with a wide range of energies. The neutrons are rarely detected with diamond  
2357 – the interactions happen mostly in the electrodes on either side of the detector. The  $\alpha$  particles  
2358 created by the interactions are detected by the diamond. Depending on the side of the interaction,  
2359 the created pulse is either due to hole or electron collection. These two interactions make the two  
2360 distinct lines in the *width* plot at 9 ns and 6 ns, as shown in figure 5.32, top left plot.

2361 A very interesting interaction point is the ballistic centre [83, 81] of the diamond. A ballistic  
2362 centre is the position from which it takes the holes and the electrons the same amount of time to  
2363 drift to the respective electrodes. In this case the shortest possible pulse is created. Conversely, to  
2364 conserve the collected charge and thus the pulse area, the pulse amplitude must be the highest at  
2365 the ballistic centre. The entries in between are created by neutron interactions at random positions  
2366 in the diamond, which produce pulses of various shapes.

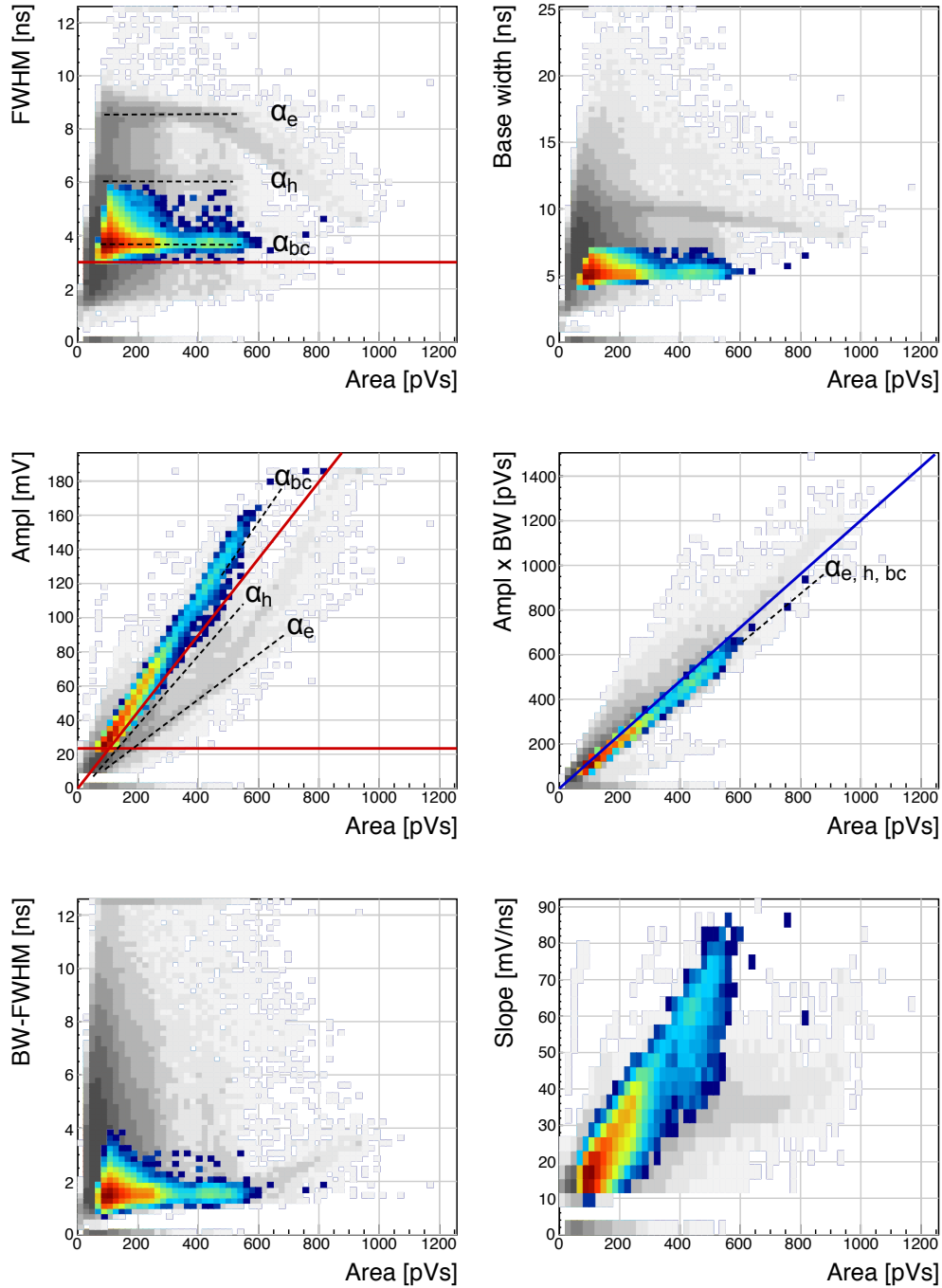


Figure 5.30:  $^{239}\text{Pu}$  Be. Qualifiers: BW-FWHM, FWHM, Form Factor

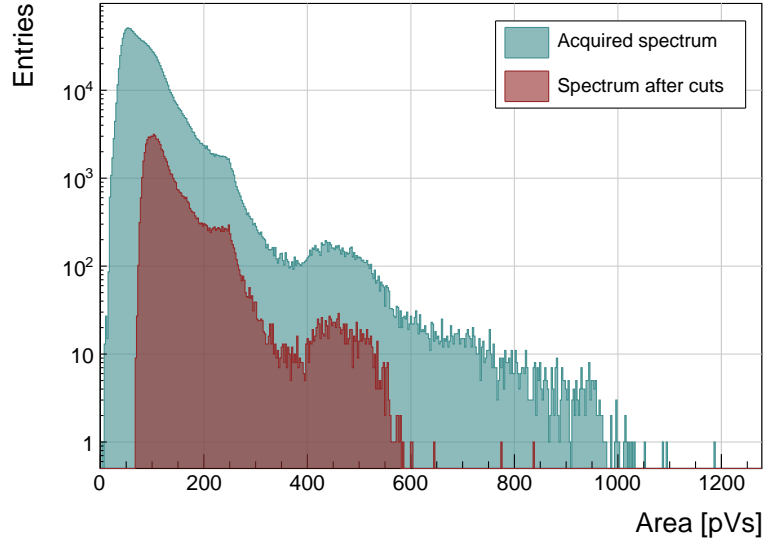


Figure 5.31:  $^{239}\text{Pu Be}$ , energy distribution of the neutrons interacting in the ballistic centre.

**5.10.2.2 Results and discussion**

Coming back to the motivation, the most efficient way of counting the 14 MeV neutrons is through the measurement of the neutrons interacting in the ballistic centre [83, 81]. To extract this type of interaction several qualifiers must be used. The first possibility is the FWHM set to 3–5 ns. However, this time the cuts on the *width* and the *calculated area* are preferred. First, a minimum constant amplitude qualifier is set to 22 mV, as shown in figure 5.32, middle left plot. Then a linear amplitude qualifier is set such that only the pulses with the highest amplitude for every area value are taken. This ensures that the high pulses from the ballistic centre are chosen. Second, a maximum linear amplitude  $\times$  base value qualifier is set such that only the pulses bearing the closest resemblance to a rectangle are chosen, as shown in figure 5.32, middle right plot. In this space the entries at the bottom of the distribution are bearing more resemblance to a rectangle whereas those at the top are more akin to triangles.

The resulting *width* plot after applied qualifiers highlights the entries with a FWHM of 4 ns, which is the width of the pulses induced by neutrons interacting in the ballistic centre. This proves that these combined qualifiers indeed pinpoint these neutron interactions. The final one-dimensional area/energy distribution of the neutrons interacting in the ballistic centre is shown in figure 5.33.

The result could be further improved by further constraining the identification, e.g to define the minimum FWHM constant qualifier and the minimum slope constant qualifier. To sum up, by applying the appropriate qualifiers to the data, the neutron interactions in the ballistic centre can be identified.

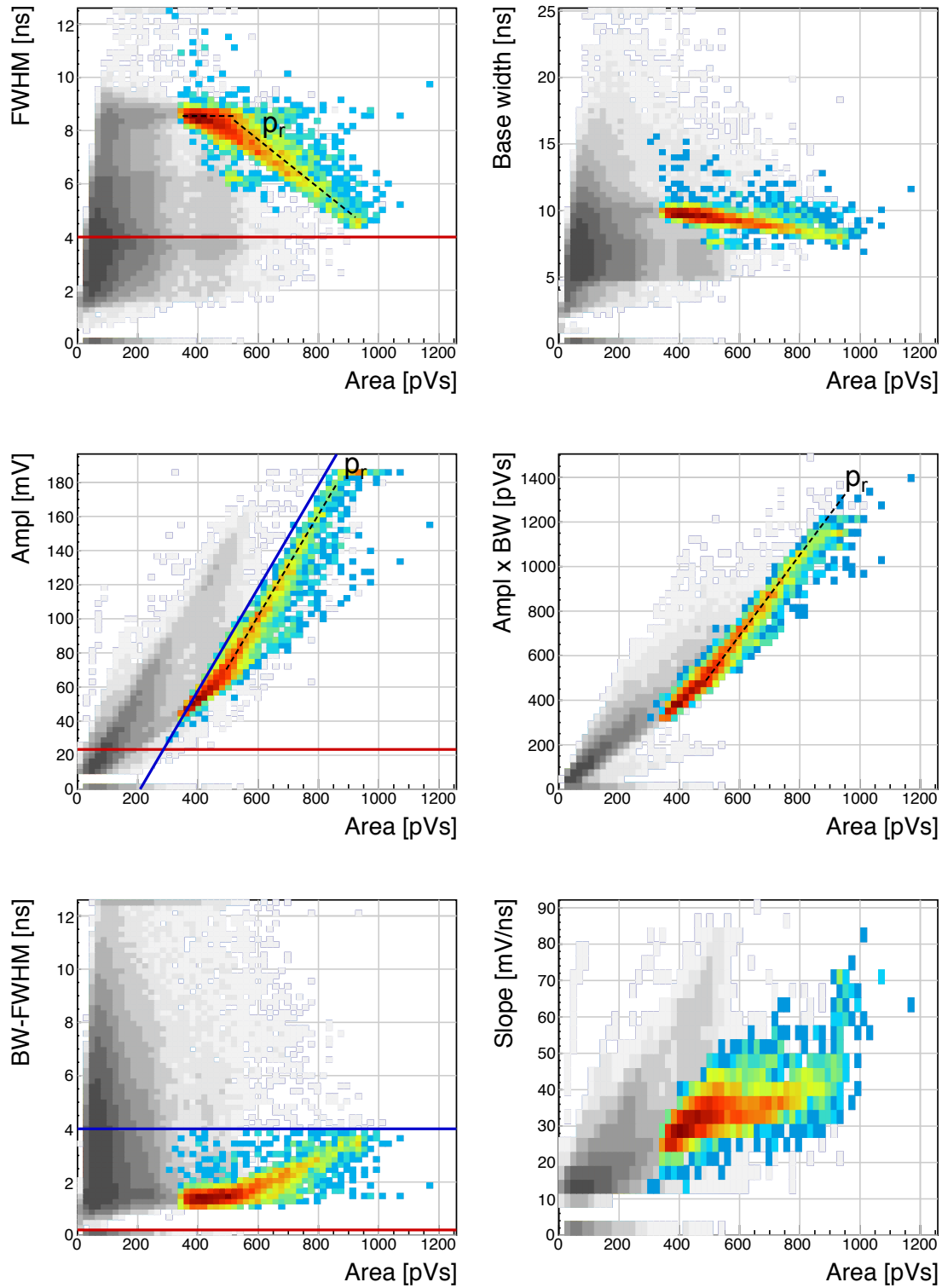


Figure 5.32:  $^{239}\text{Pu}$  Be. Qualifiers: BW-FWHM, FWHM, amplitude, linear amplitude

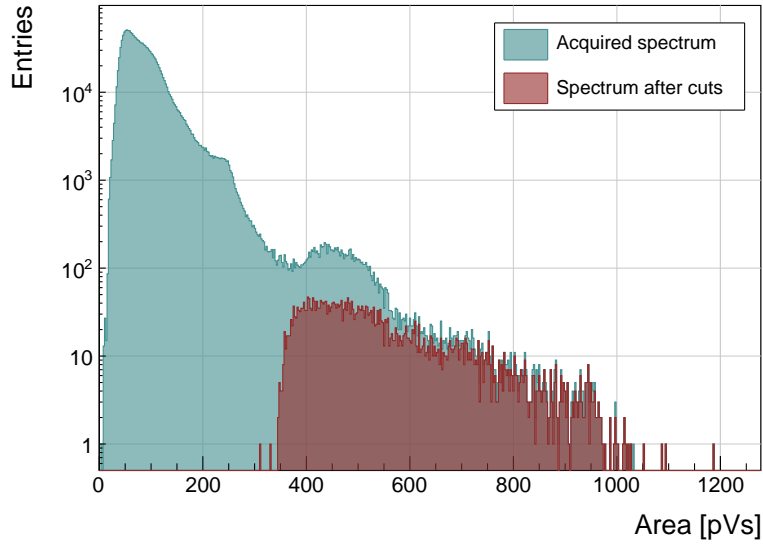


Figure 5.33:  $^{239}\text{Pu Be}$ , energy distribution of the neutrons creating a recoil proton.

### 5.10.3 Recoil proton monitoring

High energy neutrons are typically detected indirectly through elastic scattering reactions. They collide with the nucleus of atoms in the detector, transferring energy to that nucleus and creating an ion, which is detected. If the hydrogen ion – a proton – is created, it travels through the sensor while ionising it and, depending on its initial energy, stops in the sensor or exits it with some residual energy. Its specific parametric signature is discussed in section 5.9.1.3.

#### 5.10.3.1 Measurements

As in section 5.10.2, a  $^{239}\text{Pu Be}$  has been used as a source of high energy neutrons.

#### 5.10.3.2 Results and discussion

The most important qualifier for extracting the recoil protons is the amplitude. However, in this case the constant qualifiers do not help, nor does the linear qualifier starting at 0. To cut the recoil proton strand the starting point of the linear amplitude qualifier line has to start at a higher area value, 200 pVs in this case (shown in the *amplitude* plot in figure 5.32). Other qualifiers are set only to clean the outliers.

The measured parametric signature is not fully in agreement with that in figure 5.18. However, the steady fall in the *width* plot is clearly seen. The resulting one-dimensional plot after applied qualifiers is shown in figure 5.33.

To sum up, recoil protons can be extracted from a mix of created particles after neutron interactions with the diamond sensor.

**2406 5.10.4 Fast and thermal neutron monitoring**

**2407** The CROCUS reactor at EPFL [84] is a research neutron reactor. The research group working on  
**2408** the reactor is interested in measuring neutrons with energies between 1–2 MeV, which is overlapping  
**2409** with the  $\gamma$  background energy range.

**2410** The highest output power of the CROCUS reactor is 100 W. Currently there are fission chambers  
**2411** that carry out the neutron counting, which is a measure of the activity of the reactor. The new goal  
**2412** is to measure both neutrons and  $\gamma$ , but separately. The pulse shape analysis is a good solution for  
**2413** this task. For this, a 400  $\mu\text{m}$  thick diamond detector with a specially designed casing was added to  
**2414** measure the activity. The  ${}^6\text{LiF}$  foil was added for conversion of thermal neutrons. The ROSY box  
**2415** with the integrated PSA routine was used for signal analysis.

**2416 5.10.4.1 Measurements**

**2417** At the highest reactor activity the real-time system counts and analyses particles at a rate of  
**2418**  $\sim 1.5 \times 10^5 \text{ s}^{-1}$ . The results from a test run at 10 W output power are shown in figure 5.34.  
**2419** The data include a mixed field consisting of fast neutrons,  $\gamma$  and of  $\alpha$  and  ${}^3\text{H}$  particles as products  
**2420** of thermal neutron decay in the  ${}^6\text{LiF}$  foil in front of the detector. The energy deposited in the  
**2421** diamond is not as high as that from the  ${}^{239}\text{Pu}$  Be source. In addition, the analog noise during this  
**2422** measurement is higher than in the previous application. These conditions combined make particle  
**2423** identification at CROCUS a challenging task.

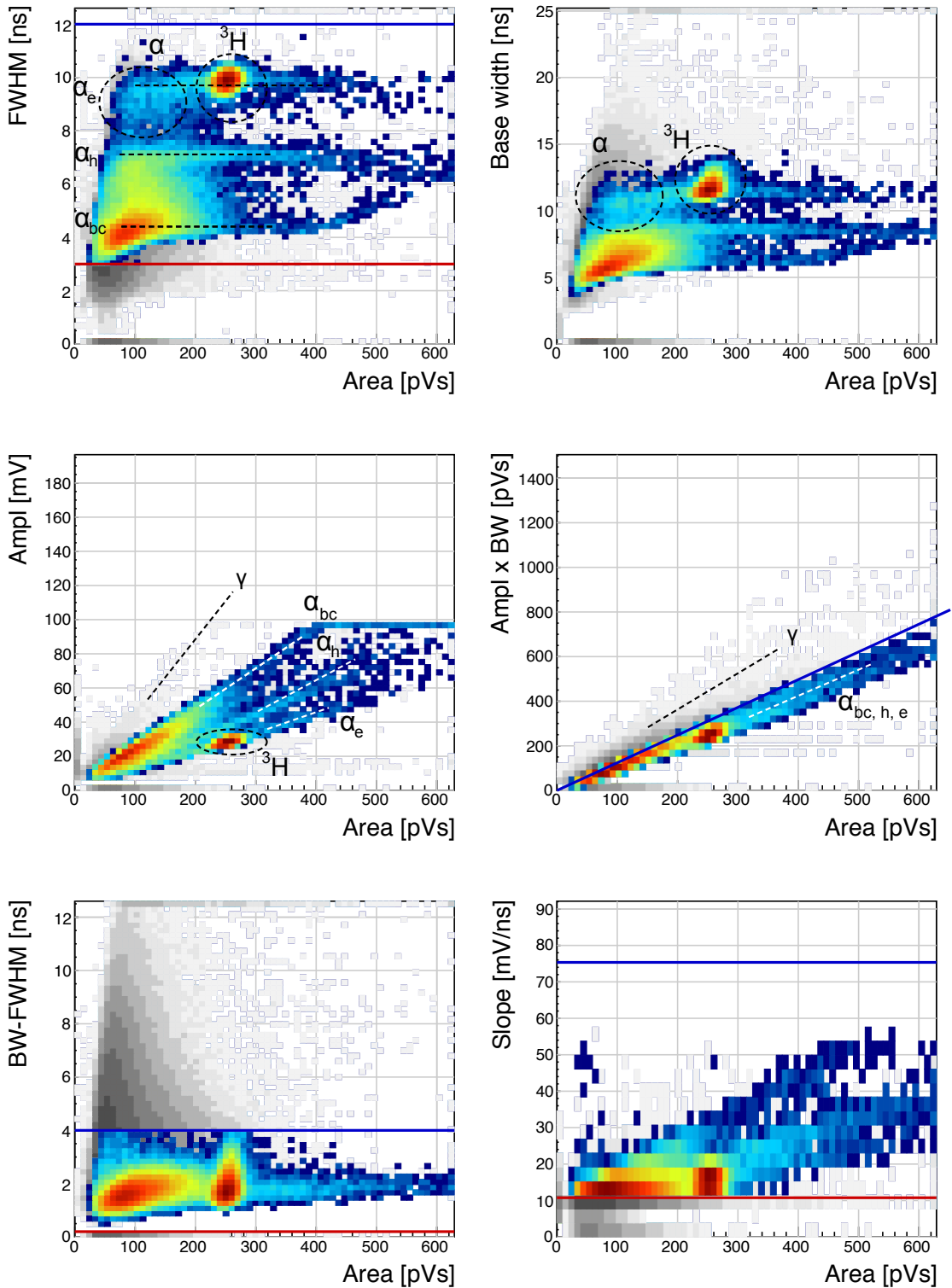


Figure 5.34: Fast neutrons, thermal neutrons,  $\gamma$ . Qualifiers: BW-FWHM, FWHM, Form factor, Slope.

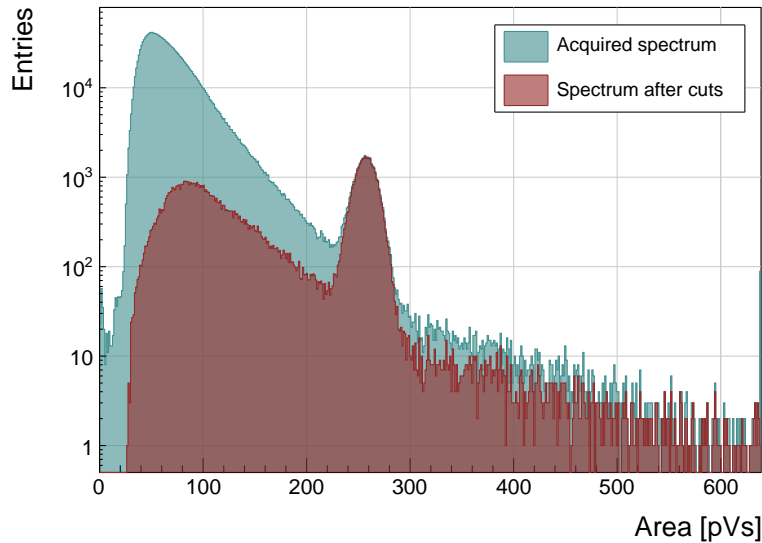


Figure 5.35: Energy spectrum in CROCUS before and after applied qualifiers.

#### 5.10.4.2 Results and discussion

The aim of this exercise is to identify both thermal and fast neutrons. For this the main qualifier used is the Form Factor - the linear line in the *calculated area*. Additional FWHM, FWHM-BW and slope constant qualifiers are used to clean the outlying entries. The resulting accepted entries in figure 5.34 have the distinctive three-line fast neutron signature in the *width* plot with two superimposed islands by the  $\alpha$  and  ${}^3\text{H}$  cluster produced by thermal neutrons in the  ${}^6\text{LiF}$  foil. The  $\gamma$  background is sufficiently suppressed. The resulting one-dimensional histogram of the area/energy distribution is shown in figure 5.35.

To sum up, by applying the Form Factor qualifier both fast and thermal neutrons can be identified, suppressing the  $\gamma$  background.

## **2434 5.11 Conclusion**

*2435 This chapter describes a system that can identify the type of radiation in real time. The system  
2436 is implemented on an FPGA in a CIVIDEC ROSY box and is used with diamond detectors. The  
2437 signal from the diamond sensor is read in and analysed in the firmware. First the shape of the pulse  
2438 is parametrised. Then the logic determines the type of particle according to the user defined cuts.  
2439 Finally the parameters are written into a histogram, which is read out by the user. The firmware  
2440 is designed to carry out the pulse shape analysis of a single pulse in  $\sim 200$  ns, yielding a maximum  
2441 pulse rate of  $6 \times 10^6$  particles per second. The rate as well as the linearity the measurement stability  
2442 with respect to noise have been verified using a pulse generator. Then several radioactive sources  
2443 were used to calibrate the device. Finally the system has been set up in two neutron reactors to test  
2444 the operation in a mixed field containing thermal neutrons, fast neutrons and  $\gamma$ . The identification  
2445 can be optimised using a combination of qualifiers to achieve the desired effect.*



2446

# Bibliography

- 2447 [1] S. F. Novaes. *Standard model: An Introduction*. In *Particles and fields. Proceedings, 10th Jorge Andre Swieca Summer School, Sao Paulo, Brazil, February 6-12, 1999*, 1999.
- 2448
- 2449 [2] Daniel Dominguez. *Standard Model. Le modele standard*. General Photo, Mar 2015.
- 2450 [3] E Rossi. *Measurements of the properties of the Higgs-like boson in the four leptons decay channel with the ATLAS detector using  $25\text{fb}^{-1}$  of proton-proton collision data*. *Nuovo Cimento C*, 037(01):217–221. 5 p, 2014.
- 2451
- 2452
- 2453 [4] European Centre for Nuclear Research, CERN. <http://home.cern>.
- 2454 [5] E Regenstreif. *The CERN proton synchrotron, 1. Ned. T. Natuurk.*, 25:117–132, 1959.
- 2455 [6] W P C Mills. *The present performance of the SPS*. *IEEE Trans. Nucl. Sci.*, 26(CERN-SPS-AOP-79-9):3176–3178. 3 p, Mar 1979.
- 2456
- 2457 [7] Atominstitut, Technical University of Vienna, Austria. <http://ati.tuwien.ac.at/startpage/EN/>.
- 2458 [8] TRIGA MARK II neutron reactor. <http://ati.tuwien.ac.at/reactor/EN/>.
- 2459 [9] General Atomics. *View of the TRIGA reactor*. 2015.
- 2460 [10] Neutron Time-of-flight experiment. <https://ntof-exp.web.cern.ch/ntof-exp/>.
- 2461 [11] Maximilien Brice. *View of the nTOF detector*. Oct 2010.
- 2462 [12] Lyndon Evans. The Large Hadron Collider. *Annu. Rev. Nucl. Part. Sci.*, 61:435–466. 32 p, 2011.
- 2463
- 2464 [13] Maximilien Brice. *LHC tunnel*. Jan 2011.
- 2465 [14] W Herr, B J Holzer, and B Muratori. *Design and Principles of Synchrotrons and Circular Colliders: Concept of Luminosity*. *Landolt-Bornstein*, 21C:6.4–1 – 6.4–7, 2013.
- 2466
- 2467 [15] I Bejar Alonso and L Rossi. *HiLumi LHC Technical Design Report: Deliverable: D1.10*. Technical Report CERN-ACC-2015-0140, CERN, Geneva, Nov 2015.
- 2468
- 2469 [16] Peter Jenni. *The experiments: ATLAS*. page 16 p, 2009.
- 2470 [17] Joao Pequenao. *Computer generated image of the whole ATLAS detector*. Mar 2008.
- 2471 [18] E. A. Ekimov, V. A. Sidorov, E. D. Bauer, N. N. Mel’nik, N. J. Curro, J. D. Thompson, and S. M. Stishov. *Superconductivity in diamond*. *Nature*, 428(6982):542–545, 04 2004.
- 2472

## BIBLIOGRAPHY

---

- 2473 [19] 1951 Park, Jong-Hee, 1955 Sudarshan, T. S., and Inc ebrary. Chemical vapor deposition.  
2474 Materials Park, Ohio : ASM International, 2001. Includes bibliographical references.
- 2475 [20] CIVIDEC Instrumentation GmbH. *sCVD diamond sensor*. <http://www.cividec.at>, 2015.
- 2476 [21] S. Sze and K. N. Kwok. Physics of Semiconductor Devices, 3rd ed. Wiley, Hoboken, NJ, 2007.
- 2477 [22] Heinz Pernegger. *The Pixel Detector of the ATLAS Experiment for LHC Run-2*. Technical  
2478 Report ATL-INDET-PROC-2015-001, CERN, Geneva, Feb 2015.
- 2479 [23] Claudia Marcelloni De Oliveira. *IBL installation into the inner detector of the ATLAS Experi-*  
2480 *ment side C*. General Photo, May 2014.
- 2481 [24] *Bremsstrahlung*. 2016.
- 2482 [25] Yoshihiko Hatano, Yosuke Katsumura, and A. Mozumder. Charged Particle and Photon Inter-  
2483 actions with Matter: Recent Advances, Applications, and Interfaces. CRC Press, 2010.
- 2484 [26] W. Blum, W. Riegler, and L. Rolandi. Particle Detection with Drift Chambers, volume 2 of 2.  
2485 Springer-Verlag, Berlin Heidelberg, 2008.
- 2486 [27] W. Shockley. *Currents to Conductors Induced by a Moving Point Charge*. *Journal of applied*  
2487 *Physics*, 9:635, 1938.
- 2488 [28] S. Ramo. *Currents Induced by Electron Motion*. *Proceedings of the IRE*, 27:584–585, 1939.
- 2489 [29] Hendrik Jansen, Norbert Wermes, and Heinz Pernegger. Chemical Vapour Deposition Diamond  
2490 - Charge Carrier Movement at Low Temperatures and Use in Time-Critical Applications. PhD  
2491 thesis, Bonn U., Sep 2013. Presented 10 Dec 2013.
- 2492 [30] Hendrik Jansen, Daniel Dobos, Thomas Eisel, Heinz Pernegger, Vladimir Eremin, and Norbert  
2493 Wermes. *Temperature dependence of charge carrier mobility in single-crystal chemical vapour*  
2494 *deposition diamond*. *Journal of Applied Physics*, 113(17), 2013.
- 2495 [31] Z. Li and H. Kraner. *Modeling and simulation of charge collection properties for neutron*  
2496 *irradiated silicon detectors*. *Nuclear Physics B - Proceedings Supplements* 32, (32):398–409,  
2497 1993.
- 2498 [32] Peter Sigmund. Particle Penetration and Radiation Effects Volume 2 - General Aspects  
2499 and Stopping of Swift Point Charges, volume 151 of *Springer Series in Solid-State Sciences*.  
2500 Springer-Verlag Berlin Heidelberg, 2006.
- 2501 [33] U. Fano. *Ionization Yield of Radiations. II. The Fluctuations of the Number of Ions*. *Physical*  
2502 *Review*, 72:26–29, July 1947.
- 2503 [34] R. C. Alig, S. Bloom, and C. W. Struck. *Scattering by ionization and phonon emission in*  
2504 *semiconductors*. 22:5565–5582, December 1980.
- 2505 [35] Claude A. Klein. *Radiation-Induced Energy Levels in Silicon*. *Journal of Applied Physics*,  
2506 30(8):1222–1231, 1959.
- 2507 [36] Moritz Guthoff and Willem De Boer. *Radiation Damage to the diamond-based Beam Condition*  
2508 *Monitor of the CMS Detector at the LHC*. PhD thesis, CERN, 2014.

## BIBLIOGRAPHY

---

- 2509 [37] Marco Marinelli, E. Milani, M. E. Morgada, G. Pucella, G. Rodriguez, A. Tucciarone,  
2510 G. Verona-Rinati, M. Angelone, and M. Pillon. *Thermal detrapping analysis of pumping-related*  
2511 *defects in diamond.* *Applied Physics Letters*, 83(18):3707–3709, 2003.
- 2512 [38] M. Huhtinen. *Simulation of non-ionising energy loss and defect formation in silicon.* *Nuclear*  
2513 *Instruments and Methods in Physics Research A*, 491:194–215, September 2002.
- 2514 [39] Moritz Guthoff, Wim de Boer, and Steffen Mller. *Simulation of beam induced lattice defects*  
2515 *of diamond detectors using {FLUKA} .* *Nuclear Instruments and Methods in Physics Research*  
2516 *Section A: Accelerators, Spectrometers, Detectors and Associated Equipment*, 735:223 – 228,  
2517 2014.
- 2518 [40] Determination of operational dose equivalent quantities for neutrons. ICRU, Washington, DC,  
2519 2001.
- 2520 [41] RD42 collaboration. <http://rd42.web.cern.ch/rd42/>.
- 2521 [42] M. Mikuž. *Diamond sensors for high energy radiation and particle detection.* TIPP, 2011.
- 2522 [43] J. L. Yarnell, J. L. Warren, and R. G. Wenzel. *Lattice Vibrations in Diamond.* *Phys. Rev. Lett.*,  
2523 13:13–15, Jul 1964.
- 2524 [44] W. Y. Liang. *Excitons.* *Physics Education*, 5:226–228, July 1970.
- 2525 [45] H. Frais-Kolbl, E. Griesmayer, H. Kagan, and H. Pernegger. A fast low-noise charged-particle  
2526 cvd diamond detector. *IEEE Transactions on Nuclear Science*, 51(6):3833–3837, Dec 2004.
- 2527 [46] J. B. Johnson. *Thermal Agitation of Electricity in Conductors.* *Phys. Rev.*, 32:97–109, Jul 1928.
- 2528 [47] H. Nyquist. *Thermal Agitation of Electric Charge in Conductors.* *Phys. Rev.*, 32:110–113, Jul  
2529 1928.
- 2530 [48] Helmuth Spieler. *Semiconductor detector systems.* Semiconductor Science and Technology.  
2531 Oxford Univ. Press, Oxford, 2005.
- 2532 [49] Xilinx Virtex 5 FPGA. <http://www.hdl.co.jp/XCM-109/top.560.jpg>.
- 2533 [50] M. Garcia-Sciveres. *ATLAS Experiment Pixel Detector Upgrades.* 2011.
- 2534 [51] Element Six. <http://www.e6.com>.
- 2535 [52] IIa Technologies Pte. Ltd. <https://www.2atechnologies.com>.
- 2536 [53] M. Červ, P. Sarin, H. Pernegger, P. Vageeswaran, and E. Griesmayer. *Diamond detector*  
2537 *for beam profile monitoring in COMET experiment at J-PARC.* *Journal of Instrumentation*,  
2538 10(06):C06016, 2015.
- 2539 [54] DRS4. <https://www.psi.ch/drs/evaluation-board>.
- 2540 [55] Paul Scherrer Institute. <https://www.psi.ch/>.
- 2541 [56] Giorgio Brianti. SPS North Experimental Area. Technical Report CERN-SPSC-T-73-8. LabII-  
2542 EA-Note-73-4, CERN, Geneva, 1973.

## BIBLIOGRAPHY

---

- 2543 [57] Michal Pomorski. Electronic properties of single crystal cvd diamond and its suitability for  
2544 particle detection in hadron physics experiments. *Wolfgang von Goethe University, Frankfurt*  
2545 *am Main, Germany*, 2008.
- 2546 [58] V. Sarin. Comprehensive Hard Materials. Elsevier Science, 2014. p. 411.
- 2547 [59] E. Griesmayer and B. Dehning. *Diamonds for Beam Instrumentation. Physics Procedia*, 37:1997  
2548 – 2004, 2012. Proceedings of the 2nd International Conference on Technology and Instrumen-  
2549 tation in Particle Physics (TIPP 2011).
- 2550 [60] V Eremin, E Verbitskaya, and Z Li. Effect of radiation induced deep level traps on si detector  
2551 performance. *Nuclear Instruments and Methods in Physics Research Section A: Accelerators,*  
2552 *Spectrometers, Detectors and Associated Equipment*, 476(3):537 – 549, 2002. Proc. of the 3rd  
2553 Int. Conf. on Radiation Effects on Semiconductor Materials, Detectors and Devices.
- 2554 [61] S. F. Kozlov, R. Stuck, M. Hage-Ali, and P. Siffert. Preparation and characteristics of natural  
2555 diamond nuclear radiation detectors. *IEEE Transactions on Nuclear Science*, 22(1):160–170,  
2556 Feb 1975.
- 2557 [62] Eugenijus Gaubas, Tomas Ceponis, Dovile Meskauskaitė, and Nikolai Kazuchits. Profiling of  
2558 current transients in capacitor type diamond sensors. *Sensors*, 15(6):13424, 2015.
- 2559 [63] Gregor Kramberger, V. Cindro, A. Gorisek, I. Mandic, M. Mikuz, and M. Zavrtanik. *Effects of*  
2560 *bias voltage during priming on operation of diamond detectors. PoS*, Vertex2012:013, 2013.
- 2561 [64] Alison G. Bates and Michael Moll. A comparison between irradiated magnetic czochralski and  
2562 float zone silicon detectors using the transient current technique. *Nuclear Instruments and*  
2563 *Methods in Physics Research Section A: Accelerators, Spectrometers, Detectors and Associated*  
2564 *Equipment*, 555(12):113 – 124, 2005.
- 2565 [65] Matevž Červ. *The ATLAS Diamond Beam Monitor*. Technical Report ATL-INDET-PROC-  
2566 2013-021, CERN, Geneva, Nov 2013.
- 2567 [66] A Gorišek, V Cindro, I Dolenc, H Frais-Klbl, E Griesmayer, H Kagan, S Korpar, G Kram-  
2568 berger, I Mandic, M Meyer, M Mikuz, H Pernegger, S Smith, W Trischuk, P Weilhammer, and  
2569 M Zavrtanik. *ATLAS diamond Beam Condition Monitor*. *Nucl. Instrum. Methods Phys. Res.,*  
2570 *A*, 572(1):67–69, 2007.
- 2571 [67] *Measurement of the Rate of Collisions from Satellite Bunches for the April-May 2010 LHC*  
2572 *Luminosity Calibration*. Technical Report ATLAS-CONF-2010-102, CERN, Geneva, Dec 2010.
- 2573 [68] *CiS Forschungsinstitut fuer Mikrosensorik GmbH*. <http://www.cismst.org/>.
- 2574 [69] J et al. Albert. *Prototype ATLAS IBL Modules using the FE-I4A Front-End Readout Chip*.  
2575 *J. Instrum.*, 7(arXiv:1209.1906):P11010. 45 p, Sep 2012. Comments: 45 pages, 30 figures,  
2576 submitted to JINST.
- 2577 [70] Fabian Huegging. *The ATLAS Pixel Insertable B-Layer (IBL)*. *Nucl. Instrum. Methods Phys.*  
2578 *Res., A*, 650(arXiv:1012.2742):45–49. 7 p, Dec 2010. Comments: 7 pages, 5 figures, 4 tables,  
2579 accepted by Nuclear Instruments and Methods A for publication.
- 2580 [71] Richard Claus. *A New ATLAS Muon CSC Readout System with System on Chip Technology*  
2581 *on ATCA Platform*. Jun 2015.

## BIBLIOGRAPHY

---

- 2582 [72] S Mueller, W deBoer, M Schneider, A Sabellek, M Schmanau, C Ruehle, T Schneider, and  
2583 R Hall-Wilton. *Study of leakage currents in pCVD diamonds as function of the magnetic field.*  
2584 *Phys. Status Solidi, A*, 206(arXiv:0905.0403):2091–2097. 6 p, May 2009. Comments: 6 pages,  
2585 16 figures, poster at Hasselt Diamond Workshop, Mar 2009.
- 2586 [73] Garrin McGoldrick, Matevž Červ, and Andrej Gorišek. *Synchronized analysis of testbeam data*  
2587 *with the Judith software*. *Nucl. Instrum. Methods Phys. Res., A*, 765:140–145, 2014.
- 2588 [74] *EUDET ACONITE telescope*. <https://telescopes.desy.de>.
- 2589 [75] E. Griesmayer et al. *Diamond detectors for LHC. Proceedings for IBIC2012. Tsukuba, Japan,*  
2590 2012.
- 2591 [76] M Capeans, G Darbo, K Einsweiller, M Elsing, T Flick, M Garcia-Sciveres, C Gemme, H Perneg-  
2592 ger, O Rohne, and R Vuillermet. ATLAS Insertable B-Layer Technical Design Report. Technical  
2593 Report CERN-LHCC-2010-013. ATLAS-TDR-19, CERN, Geneva, Sep 2010.
- 2594 [77] J Dopke. Overview of the ATLAS Insertable B-Layer (IBL) Project. Jul 2013.
- 2595 [78] P. Kavrigin, P. Finocchiaro, E. Griesmayer, E. Jericha, A. Pappalardo, and C. Weiss. *Pulse-*  
2596 *shape analysis for gamma background rejection in thermal neutron radiation using CVD dia-*  
2597 *mond detectors*. *Nuclear Instruments and Methods in Physics Research A*, (795), 2015.
- 2598 [79] E. Griesmayer, R. Bergmann, H. Böck, M. Cagnazzo, P. Kavrigin, B. Morgenbesser, and  
2599 M. Villa. *A Novel Neutron Flux Monitor Based On Diamond Detectors at the Vienna TRIGA*  
2600 *Mark II Reactor. submitted to the proceedings of ICRR 2015*, 2015.
- 2601 [80] C. Weiss, H. Frais-Kölbl, E. Griesmayer, and P. Kavrigin. *Ionization signals of diamond detec-*  
2602 *tors in fast neutron fields*. 2016.
- 2603 [81] C. Weiss. A CVD diamond detector for  $(n,\alpha)$  cross-section measurements. PhD thesis, TU  
2604 Wien, Vienna, 2014.
- 2605 [82] *ITER fusion reactor*. <https://www.iter.org/>.
- 2606 [83] P. Kavrigin, E. Griesmayer, F. Belloni, A.J.M. Plompen, P. Schillebeeckx, and C. Weiss.  
2607  $^{13}C(n,\alpha_0)^{10}Be$  cross section measurement with sCVD diamond detector. *EPJA*, 2016.
- 2608 [84] *CROCUS neutron reactor*. <http://lrs.epfl.ch/page-55655-en.html>.